



**A NON-DESTRUCTIVE EVALUATION  
APPLICATION USING SOFTWARE  
DEFINED RADIOS AND BANDWIDTH  
EXPANSION**

THESIS

Nicholas J O'Brien, Flight Lieutenant, RAAF  
AFIT-ENG-MS-20-M-049

**DEPARTMENT OF THE AIR FORCE  
AIR UNIVERSITY**

***AIR FORCE INSTITUTE OF TECHNOLOGY***

**Wright-Patterson Air Force Base, Ohio**

DISTRIBUTION STATEMENT A  
APPROVED FOR PUBLIC RELEASE; DISTRIBUTION UNLIMITED.

The views expressed in this document are those of the author and do not reflect the official policy or position of the United States Air Force, the United States Department of Defense or the United States Government. This material is declared a work of the U.S. Government and is not subject to copyright protection in the United States.

AFIT-ENG-MS-20-M-049

A NON-DESTRUCTIVE EVALUATION APPLICATION USING SOFTWARE  
DEFINED RADIOS AND BANDWIDTH EXPANSION

THESIS

Presented to the Faculty  
Department of Electrical and Computer Engineering  
Graduate School of Engineering and Management  
Air Force Institute of Technology  
Air University  
Air Education and Training Command  
in Partial Fulfillment of the Requirements for the  
Degree of Master of Science in Electrical Engineering

Nicholas J O'Brien, BENG (Electrical and Electronic)  
Flight Lieutenant, RAAF

March 26,2020

DISTRIBUTION STATEMENT A  
APPROVED FOR PUBLIC RELEASE; DISTRIBUTION UNLIMITED.

AFIT-ENG-MS-20-M-049

A NON-DESTRUCTIVE EVALUATION APPLICATION USING SOFTWARE  
DEFINED RADIOS AND BANDWIDTH EXPANSION

THESIS

Nicholas J O'Brien, BENG (Electrical and Electronic)  
Flight Lieutenant, RAAF

Committee Membership:

Dr. Peter J. Collins  
Chair

Dr. Michael A. Temple  
Member

Major J. Addison Betances, Ph.D  
Member

## Abstract

The development of low-complexity, lightweight and low-cost Non-Destructive Evaluation (NDE) equipment for microwave device testing is desirable from a maintenance efficiency and operational availability perspective. Current NDE equipment tends to be custom-designed, cumbersome and expensive. Software Defined Radio (SDR) technology, and a bandwidth expansion technique that exploits a priori transmit signal knowledge and auto-correlation provides a solution.

This research investigated the reconstruction of simultaneous SDR receiver instantaneous bandwidth (sub-band) collections using single, dual and multiple SDR receivers. The adjacent sub-bands, collectively spanning a transmit signal bandwidth were auto-correlated with a replica transmit signal to restore frequency and phase offsets. The offsets arise due to different local oscillator manufacturing tolerances, temperature effects and ageing.

A 100 MHz bandwidth uniform white noise signal was reconstructed from both dual ( $2 \times 50$  MHz) and multiple ( $4 \times 25$  MHz) SDR collections. The 100 MHz bandwidth exceeds a B205 SDR receiver instantaneous bandwidth. The auto-correlation technique minimizes SDR hardware numbers as bandwidth overlap is not required.

Hardware test Symbol Error Rate (SER) was compared with a theoretical coherently detected M-ary orthogonal signal. A 2 MHz dual SDR uniform white noise signal reconstruction exhibited a 5 dBW loss when compared with the theoretical value. The 4 MHz multiple SDR signal reconstruction exhibited a 6 dBW loss.

Finally, a linear feedback shift register was used to generate the uniform white noise signal. This provided near true-noise characteristics employing a polynomial primitive to ensure  $2^{36} - 1$  non-repeatable sequences.

## Acknowledgements

I would like to thank my beautiful wife for taking care of everything so I could devote time to my studies. Beyond the shadow of a doubt, your encouragement and support got me through the tougher days.

To my advisor Dr. P. Collins, committee members, instructors, staff and students who steered me through the obstacles on the way you have my gratitude. I enjoyed having a ‘yarn’ whenever the opportunity arose. You are all great people.

Dr. M. Temple, Capt. Y. Matsui and Capt. N. Echeverry deserve a special mention, thanks for the RF-DNA signal collection conversion code, the Ubuntu assistance, and the Frequency Locked Loop assisted Phase Locked Loop conceptual discussion.

Finally, I am especially indebted to two AFIT members; Maj. J.A. Betances, Ph.D and Mr Michael Paprocki. Maj. Betances for the countless hours you invested in ensuring I graduated. More so than most research efforts, this thesis document is attributable to your mentoring, enthusiasm and endless patience, as well as being the prime contributor to auto-correlation code development. Mr Michael Paprocki (IMSO) for being just a phone call away from the moment we touched down in the USA. It was reassuring to have such a genuine person in your position, not to mention that you tell the best stories. You are both ‘Top Blokes’.

Nicholas J O’Brien

# Table of Contents

	Page
Abstract .....	iv
Acknowledgements .....	v
List of Figures .....	viii
List of Tables .....	xiii
List of Acronyms .....	xiv
I. Introduction .....	1
1.1 Background .....	1
1.2 Problem Statement .....	2
1.3 Research Objectives .....	4
1.4 Research Implications .....	5
1.5 Summary .....	6
II. Literature Review .....	7
2.1 Non-Destructive Evaluation .....	7
2.2 Software Defined Radio .....	9
2.2.1 Ettus USRP B205-mini Software Defined Radio .....	10
2.2.2 Ettus USRP X310 Software Defined Radio .....	10
2.2.3 GNU Radio Companion Interface Software .....	12
2.3 Bandwidth Expansion Principles .....	18
2.3.1 Wide Sense Stationary Measurement Techniques .....	19
2.3.2 Wide Sense Stationary Reference Techniques .....	24
2.3.3 Non-Wide Sense Stationary Techniques .....	27
2.4 Device Classification .....	35
2.4.1 Signal Selection .....	35
2.4.2 Signal Collection .....	37
2.4.3 Fingerprint Generation .....	37
2.4.4 Device Training and Classification .....	38
2.5 Summary .....	41
III. Methodology .....	42
3.1 Bandwidth Expansion Modelling .....	43
3.1.1 The Communications System Signal Process Model .....	43
3.1.2 Signal Generation and Processing .....	47
3.1.3 Signal Process Model Validation .....	55

	Page
3.1.4 Symbol Recovery Measurement . . . . .	56
3.2 Bandwidth Expansion Techniques . . . . .	57
3.2.1 Auto-correlation - Frequency ‘Pull-In’ . . . . .	58
3.2.2 Auto-correlation - Phase Correction . . . . .	60
3.2.3 Transmit Signal Preparation . . . . .	60
3.3 Bandwidth Expansion Application . . . . .	63
3.3.1 Single Receiver Dual Channel Simulations . . . . .	64
3.3.2 Dual Receiver Simulations . . . . .	65
3.3.3 Multiple Receiver Simulations . . . . .	66
3.3.4 Single Receiver Hardware Tests . . . . .	66
3.3.5 Dual Receiver Hardware Tests . . . . .	69
3.3.6 Multiple Receiver Hardware Tests . . . . .	72
3.4 Scaling the Bandwidth Expansion Technique . . . . .	76
3.5 RFDNA Test Case . . . . .	78
3.6 Summary . . . . .	79
IV. Results and Analysis . . . . .	80
4.1 Validation Results . . . . .	80
4.2 Simulation Results . . . . .	82
4.2.1 Dual Receiver Simulations . . . . .	82
4.2.2 Multiple Receiver Simulations . . . . .	89
4.3 Hardware Test Results . . . . .	93
4.3.1 Single Receiver Hardware Test Results . . . . .	93
4.3.2 Dual Receiver Hardware Test Results . . . . .	99
4.3.3 Multiple Receiver Hardware Test Results . . . . .	106
4.4 RFDNA Test Results . . . . .	113
4.5 Summary . . . . .	113
V. Conclusion . . . . .	115
5.1 Future Work . . . . .	117
5.1.1 Bandwidth Expansion Technique Transfer . . . . .	117
5.1.2 Alternate Support Hardware Tests . . . . .	117
5.1.3 SDR Filter Attenuation . . . . .	118
5.1.4 RF-DNA Tests . . . . .	118
Appendix A: Non-Linear Least Squares Estimation . . . . .	119
Appendix B: Simulation Summary . . . . .	123
Appendix C: Hardware Test Summary . . . . .	124
Bibliography . . . . .	125



## List of Figures

Figure		Page
1	Ettus Universal Software Radio Peripheral B205-mini Software Defined Radio. ....	11
2	Ettus Universal Software Radio Peripheral B200-mini Software Defined Radio architecture. ....	11
3	Ettus Universal Software Radio Peripheral X310 SDR. ....	13
4	Bandwidth expansion using overlapping frequency sub-bands. ....	20
5	Bandwidth expansion using aligned frequency sub-bands. ....	25
6	A basic phase locked loop diagram. ....	28
7	A first order frequency locked loop assisted second order phase locked loop diagram. ....	29
8	Depiction of a Multiple Discriminant Analysis three-dimensional sub-space projection onto two planes. ....	40
9	Depiction of a Fisher plane subspace showing a three device classification. ....	41
10	Communications system transmit process model. ....	46
11	Communication system receive signal process model. ....	48
12	PSD showing the base-band bandwidth of a QPSK transmit signal. ....	52
13	Simulated QPSK transmit signal constellation. ....	52
14	Simulated QPSK received signal constellation after phase compensation. ....	53
15	PSD showing the base-band bandwidth uniform white noise transmit signal. ....	53
16	Matlab <sup>®</sup> FVtool filter depiction showing the steep filter roll-off used to minimize bandwidth overlap between adjacent receive signal sub-bands. ....	62

Figure	Page
17	Filtered 1 MHz uniform white noise signal sub-band for transmit signal construction. . . . . 62
18	Hardware circuit setup for single SDR receiver tests. . . . . 69
19	GNU radio companion interface setup for single SDR hardware tests. . . . . 70
20	Hardware circuit setup for dual SDR receiver tests. . . . . 72
21	GNU radio companion interface setup for dual SDR receiver hardware tests. . . . . 73
22	Hardware circuit setup for multiple SDR receiver test. . . . . 74
23	GNU radio companion interface setup for multiple SDR receiver hardware test. . . . . 75
24	Monte Carlo simulation for the QPSK signal system process model validation showing SER versus $E_s/N_0$ for the single receiver, dual channel case. . . . . 81
25	Monte Carlo simulation for the uniform white noise signal system process model validation showing SER versus $E_s/N_0$ for the single receiver, dual channel case. . . . . 81
26	Simulated 2 MHz uniform white noise transmit and receive signal frequency pull in correlation sequence for a dual SDR collection. . . . . 84
27	Simulated 2 MHz uniform white noise transmit signal PSD for dual SDR collection. . . . . 85
28	Simulated 2 MHz uniform white noise overlay signal PSD showing the two 1 MHz SDR collections. . . . . 85
29	Simulated 2 MHz uniform white noise recombined signal PSD for a dual SDR collection. . . . . 86
30	Simulated 2 MHz uniform white noise transmit and receive symbol correlation for a dual SDR collection showing uncorrected correlation lag. . . . . 87

Figure	Page
31	Simulated 2 MHz uniform white noise transmit and receive symbol correlation for a dual SDR collection showing corrected correlation lag. . . . . 87
32	Monte Carlo simulation for the 2 MHz uniform white noise SER versus $E_s/N_0$ for 0 to 25 dB, for single and dual SDR collections. . . . . 88
33	Simulated 4 MHz uniform white noise transmit signal PSD for multiple SDR collection. . . . . 90
34	Simulated 4 MHz uniform white noise overlay signal PSD showing the four 1 MHz SDR collections. . . . . 90
35	Simulated 4 MHz uniform white noise recombined signal PSD for a multiple SDR collection. . . . . 91
36	Simulated 4 MHz uniform white noise transmit and receive symbol correlation for a multiple SDR collection. . . . . 92
37	Monte Carlo simulation for the 4 MHz uniform white noise SER versus $E_s/N_0$ for 0 to 25 dB, for single, dual and multiple SDR collections. . . . . 92
38	Single receiver hardware test PSD showing an approximate 50 MHz (at $-3$ dB) transmit bandwidth. . . . . 94
39	Single receiver hardware test PSD showing an approximate 50 MHz (at $-3$ dB) collection bandwidth. . . . . 94
40	Single receiver hardware test plot showing a symbol recovery correlation for the approximate 50 MHz (at $-3$ dB) collection bandwidth. . . . . 95
41	Single receiver hardware test PSD showing an approximate 100 MHz (at $-3$ dB) transmit bandwidth. . . . . 96
42	Single receiver hardware test PSD showing the failed 100 MHz collection. . . . . 96
43	Single receiver hardware test plot showing a symbol recovery correlation for the failed 100 MHz collection bandwidth. . . . . 97
44	Hardware test frequency change versus signal duration for a uniform white noise single SDR collection. . . . . 98

Figure	Page
45	Hardware test 2 MHz uniform white noise transmit signal PSD for dual SDR collection. . . . . 101
46	Hardware test 2 MHz uniform white noise overlay signal PSD showing the two 1 MHz SDR collections. . . . . 101
47	Hardware test 2 MHz uniform white noise recombined signal PSD for a dual SDR collection. . . . . 102
48	Hardware test 2 MHz uniform white noise transmit and receive symbol correlation for a dual SDR collection. . . . . 102
49	Hardware test 2 MHz uniform white noise SER versus $E_s/N_0$ for 0 to 25 dB, for a dual SDR collection. . . . . 103
50	Hardware test 20 MHz uniform white noise overlay signal PSD showing the two 10 MHz SDR collections. . . . . 104
51	Hardware test 100 MHz uniform white noise overlay signal PSD showing the two 50 MHz SDR collections. . . . . 104
52	Hardware test 100 MHz uniform white noise transmit and receive symbol correlation for a dual SDR collection. . . . . 105
53	Hardware test 4 MHz uniform white noise transmit signal PSD for multiple SDR collection. . . . . 107
54	Hardware test 4 MHz uniform white noise overlay signal PSD showing the four 1 MHz SDR collections. . . . . 108
55	Hardware test 4 MHz uniform white noise recombined signal PSD for a multiple SDR collection. . . . . 108
56	Hardware test 4 MHz QPSK overlay signal for a multiple SDR collection. . . . . 109
57	Hardware test 4 MHz QPSK overlay signal showing the four 1 MHz SDR collections. . . . . 109
58	Hardware test 4 MHz uniform white noise transmit and receive symbol correlation for a multiple SDR collection. . . . . 111
59	Hardware test 4 MHz uniform white noise SER versus $E_s/N_0$ for 0 to 25 dB, for a multiple SDR collection. . . . . 111

Figure	Page
60	Hardware test 20 MHz uniform white noise overlay signal showing the four 5 MHz SDR collections. . . . . 112
61	Hardware test 100 MHz uniform white noise overlay signal showing the four 25 MHz SDR collections. . . . . 112
62	Hardware test 100 MHz uniform white noise transmit and receive symbol correlation for a multiple SDR collection. . . . . 113

## List of Tables

Table		Page
1	GRC options block. . . . .	14
2	GRC variable block. . . . .	14
3	GRC file source block. . . . .	14
4	GRC UHD: USRP sink block. . . . .	15
5	GRC UHD: USRP source block. . . . .	16
6	GRC file sink block. . . . .	17
7	GRC head block. . . . .	17
8	GRC QT GUI frequency sink block. . . . .	17
9	QPSK signal simulation parameters for communication system process model validation. . . . .	49
10	Uniform white noise signal simulation parameters for communication system process model validation. . . . .	51
11	RRC filter parameters for transmit signal preparation. . . . .	61
12	Bandwidth expansion simulations. . . . .	123
13	Bandwidth expansion hardware tests. . . . .	124

## List of Acronyms

**10G ETH** 10 Gigabit Ethernet.

**1G ETH** 1 Gigabit Ethernet.

**ADC** Analog to Digital Converter.

**AFIT** Air Force Institute of Technology.

**AWG** Analog Waveform Generator.

**AWGN** Additive White Gaussian Noise.

**BER** Bit Error Rate.

**DAC** Digital to Analog Converter.

**DFT** Discrete Fourier Transform.

**DUT** Device Under Test.

**FIR** Finite Impulse Response.

**FLD** Fisher Linear Discriminant.

**FLL** Frequency Locked Loop.

**FPGA** Field Programmable Gate Array.

**FSK** Frequency Shift Keying.

**GPS** Global Positioning System.

**GPSDO** Global Positioning System Disciplined Oscillator.

**GRC** GNU Radio Companion.

**GUI** Graphic User Interface.

**IDFT** Inverse Discrete Fourier Transform.

**ISI** Inter-Symbol Interference.

**LFSR** Linear Feed-back Shift Register.

**LPI** Low Probability of Intercept.

**Matlab<sup>®</sup>** Matrix Laboratory.

**MDA** Multiple Discriminant Analysis.

**MLE** Maximum Likelihood Estimation.

**NDE** Non-Destructive Evaluation.

**NDT** Non-Destructive Testing.

**NLS** Non-Linear Least Squares.

**NoNET** Noise Radar Network.

**OQPSK** Offset-Quadrature Phase Shift Keying.

**PLL** Phase Locked Loop.

**PMF** Probability Mass Function.

**PPS** Pulse Per Second.

**PSD** Power Spectral Density.



**QPSK** Quadrature Phase Shift Keying.

**RF** Radio Frequency.

**RF-DNA** Radio Frequency-Distinct Native Attribute.

**RFIC** RF Integrated Circuit.

**RRC** Raised Root Cosine.

**SDR** Software Defined Radio.

**SER** Symbol Error Rate.

**SMA** Sub-Minature Version A.

**SNR** Signal-to-Noise Ratio.

**SURE** Stimulated Unintended Radiated Emissions.

**USRP** Universal Software Radio Peripheral.

**VCO** Voltage Controlled Oscillator.

**WSS** Wide Sense Stationary.

# A NON-DESTRUCTIVE EVALUATION APPLICATION USING SOFTWARE DEFINED RADIOS AND BANDWIDTH EXPANSION

## I. Introduction

### 1.1 Background

Competing operational availability and system-maintenance demands are common in today's defense environment where budgetary constraints and high costs can limit the use of redundant systems. Non-Destructive Evaluation (NDE) offers a potential solution providing Device Under Test (DUT) system maintenance measurement without impairing serviceability [1]. Instrument portability, complexity and cost can limit NDE adoption with some technicians preferring intrusive practices such as Bit Error Rate Testing or Time Domain Reflectometry. Frequency spectrum regulation and Radio Frequency Interference can also constrain adoption when testing involves electrical measurements [2].

Recent research efforts combine Air Force Institute of Technology (AFIT) Noise Radar Network (NoNET), Stimulated Unintended Radiated Emissions (SURE) and Radio Frequency-Distinct Native Attribute (RF-DNA) techniques to characterize the behaviour of microwave devices [2–7]. The devices are stimulated with an active noise interrogation signal. The successful noise signal experiments demonstrated concurrent frequency spectrum use with other Radio Frequency (RF) sources [4]. The non-intrusive characteristics of the measurement system show promising results for the field of NDE [7]. However, the NoNET system is not portable.

As early as 1959, McMaster acknowledged that portability was a primary factor

in NDE (then Non-Destructive Testing (NDT)) adoption [1]. Recent AFIT research investigated the portability, complexity and cost issues surrounding the SURE process and NoNET. This research applied a non-Wide Sense Stationary (WSS) bandwidth expansion technique to reconstruct a Quadrature Phase Shift Keying (QPSK) signal. The technique restored a 1.98 MHz bandwidth using two Software Defined Radio (SDR) narrow-band (1 MHz) receiver collections [8]. The collections were conducted simultaneously. The Software Defined Radios provided a light-weight, low-complexity and low-cost alternative to the previously used NoNET. The bandwidth expansion technique provided a means for SURE collection and reconstruction of non-WSS signals.

Further investigation of active noise signal collection using SDR receivers and a reliable bandwidth expansion technique is warranted. The non-intrusive characteristics of the active noise signal, and consequently the NDE device, would be of significant benefit to maintenance fault investigation.

To exploit NDE characteristics a proposed device would need sufficient instantaneous receiver bandwidth to support microwave device, RF front-end, cable and connector characterization using SURE and RF-DNA processes. The challenge is to provide sufficient instantaneous receiver bandwidth for accurate wide-band signal reconstruction.

## **1.2 Problem Statement**

The problem is to collect, and then reconstruct, a wide-band uniform white noise signal. The transmitted signal bandwidth is assumed to span multiple SDR receiver bandwidths. The transmit signal is also assumed to be time-variant. Therefore, the recovery requires multiple SDRs to effect simultaneous collection of the wide-band signal. Each SDR collecting an allocated part (sub-band) of the signal.

The collected sub-bands must then be processed using a non-WSS bandwidth expansion technique that accounts for the time varying nature of the uniform white noise signal. The technique must resolve time-alignment, frequency drift and phase correction issues. This must occur with sufficient accuracy to align SDR sub-band signals, allowing for transmit symbols to be recovered from the restored signal.

Software Defined Radios typically have a narrow instantaneous bandwidth. Their light weight, low complexity and low cost enhances portability, flexibility and marketability. This is at the expense of Analog to Digital Converter (ADC) bit-rate performance. Low ADC bit-rates limit SDR instantaneous bandwidth [9]. Previous work identified device characterization is optimized when the DUT is stimulated with a wide-band signal; that is, wider than the frequency response of the DUT [6]. Therefore, SDR instantaneous bandwidth limitations appear to be inconsistent with the requirement for wide-band signal response collection.

This presents a challenge. SDRs commonly support Megahertz bandwidths (e.g. Ettus Universal Software Radio Peripheral (USRP) B205-mini SDR has a 56 MHz instantaneous bandwidth [10]) while many microwave devices support Gigahertz bandwidths (e.g. Mini-Circuits model ZX60-14012L+ amplifier has a 30 kHz-14 GHz instantaneous bandwidth [6]). This implies a single SDR receiver must collect and store consecutive wide-band signal portions until all sub-bands are collected for processing.

This is suitable where “a time delay in the input sequence causes [an] equivalent time delay in the systems output sequence” [11], (i.e. a time-invariant system) and where the signal statistics are time invariant [12] (i.e. WSS). However, if the wide-band system is time-variant or signals are non-WSS, then simultaneous collection of the entire bandwidth using multiple SDRs is required [8].

Assuming the signal response is non-WSS, simultaneous bandwidth collection for accurate signal reconstruction requires time, frequency and phase synchronization

between each SDR receiver, as well as synchronization between the transmitter and SDR receivers. For collection processing, synchronization becomes increasingly difficult when multiple SDR receivers are used. Frequency differences between each SDR receiver must be corrected before SDR receiver phase values can be estimated. Frequency drift inherent to each SDR must also be corrected to align adjacent sub-bands for accurate wide-band signal reconstruction.

### 1.3 Research Objectives

Everett achieved sub-band alignment using a novel cross-correlation technique which provided a successful bandwidth expansion proof-of-concept. The research effort did not reconstruct a wide-band signal response exceeding an individual SDR bandwidth, or reconstruct a wide-band signal response spanning more than two SDRs [8].

This research effort aims to demonstrate a wide-band signal response reconstruction exceeding an individual SDR bandwidth. The research effort will also show a signal reconstruction spanning multiple SDR narrow-band receiver bandwidths. The wide-band signal response collection capability is required for a mature NDE device assumed to have transmission bandwidth similar to the NoNET system. The NoNET noise diode transmits a 100 MHz–1.5 GHz Additive White Gaussian Noise (AWGN) signal, with band-pass recovery spanning 395 – 720 MHz [13].

Everett’s QPSK signal reconstruction technique is also trialled during this research. A frequency correction technique based on a non-data aided feed forward carrier frequency offset estimation model is substituted for the spectral cross-correlation technique to resolve QPSK signal frequency offset. The spectral cross-correlation technique and carrier frequency offset estimation are discussed in further detail in Section 2.3.3.

This research substitutes a wide-band uniform white noise signal for the QPSK signal. Wide-band uniform white noise experiments are necessary because the mature NDE device is assumed to require a wide-band noise transmission capability. A noise signal being more akin to processing NoNET transmission-type signals instead of a typical M-ary shift keying based communications signal. The QPSK signal is retained to validate the process models, and to provide a comparative measure of bandwidth expansion performance.

Finally, Everett’s cross-correlation bandwidth expansion techniques are replaced by an auto-correlation technique using a priori knowledge of the transmit signal. This ‘template’ technique is commonly used in radar matched filters [14]. The matched filter is used to detect a delayed version of the transmitted signal embedded in an unknown signal. This research effort aims to exploit ‘templating’ to synchronize adjacent sub-band frequency and phase values, in addition to detecting the delayed transmit signal [14]. This research does not replicate a specific transmission capability but focuses on reconstructing a signal using SDR receiver instantaneous bandwidth expansion.

#### **1.4 Research Implications**

NDE is non-intrusive, reducing DUT degradation and out-of-service times [1]. If the proposed low-power and wide-bandwidth NDE solution is realizable, even considering the use of multiple SDR receivers, the research would result in a low-cost, light-weight, portable alternative to existing NDE measurement instruments. As mentioned, existing NDE instruments tend to be high-cost and cumbersome devices.

Fault condition identification without system removal from service, disassembly, intrusive inspection, reassembly and service release requirements could significantly reduce maintenance investigation times. This would increase system availability. A

recent example is a wireless RF laboratory test for connector continuity. The test demonstrated the ability to distinguish loose and damaged Sub-Minature Version A (SMA) and Type N connectors without having to remove the DUT from service [7]. The mature NDE application would benefit the Department of Defense, Australian Defence Force and wider industry.

## 1.5 Summary

Chapter I described the need for an NDE device, outlined the research problem, detailed the research objectives and identified the research implications. This research effort is documented as follows: Chapter II provides the necessary theoretical background required to prepare the reader for understanding the research being undertaken, including a review of bandwidth expansion research; Chapter III describes the simulation and test methodologies implemented to trial bandwidth expansion techniques; Chapter IV details simulation and test results, and provides analysis; while Chapter V concludes with the research findings and identifies future work.

## II. Literature Review

The following sections provide the necessary theoretical background and a summary of current bandwidth expansion research to prepare the reader for this research effort. Section 2.1 defines Non-Destructive Evaluation (NDE), discusses NDE benefits and identifies NDE applications; Section 2.2 describes Software Defined Radio (SDR) technology, details Ettus Universal Software Radio Peripheral (USRP) B205-mini SDR and the Ettus USRP X310 SDR features and architecture. This section also describes the GNU Radio Companion (GRC) software that provides the interface between the host-PC and the SDRs. The description includes summary tables of all processing blocks used for this research effort, and their affected parameters. Section 2.3 describes bandwidth expansion principles using Wide Sense Stationary (WSS) and non-WSS research examples. The non-data-aided feed forward carrier frequency offset estimation model and phase-offset cross-correlation techniques are discussed here; finally Section 2.4 describes signal collection and the Radio Frequency-Distinct Native Attribute (RF-DNA) processes used for device classification.

### 2.1 Non-Destructive Evaluation

McMaster provides a NDE (then Non-Destructive Testing (NDT)) definition. “The science of nondestructive [evaluation] embraces all methods for the detection or measurement of the significant properties or performance capabilities of materials, parts, assemblies, equipment or structures, by tests which do not impair their serviceability,” [1].

NDE is of significant benefit for maintenance servicing. In many cases NDE limits, or removes, the need for traditional maintenance practices where system service removal, disassembly, inspection, maintenance and repair, reassembly and service



release are required. With renewed emphasis on asset management, Device Under Test (DUT) inspection using non-intrusive processes allows for more frequent monitoring while reducing maintenance down-times. Non-intrusive processes can also limit service damage. A frequent monitoring regime supports transition from preventative maintenance practices, using time-based assembly replacement, to predictive practices, whereby assembly replacement occurs on detection or measurement of a specific event [15].

The scope of NDE application is broad, and includes the measurement of geometric properties (e.g. thickness), mechanical properties (e.g. hardness), thermal properties (e.g. heat resistance) and electrical and magnetic properties. Historical electrical and magnetic property measurement include eddy current tests to check for structural discontinuities, Megger tests to check the condition of electrical wiring insulation and conductivity tests to check for dielectric thickness [1]. More recent electrical and magnetic based NDE applications include antenna acceptance tests [2], amplifier acceptance tests [6] and connector continuity tests [7].

For this research effort, DUT materials, parts, assemblies, equipment or structures are selected microwave devices. The detection or measurement method involves DUT stimulation using the Stimulated Unintended Radiated Emissions (SURE) process, so as not to impair serviceability. The significant electrical property measurements are classified using RF-DNA. RF-DNA discriminates signal features. For example, the feature could discriminate between products to serial number, or the feature could discriminate between a serviceable and unserviceable device (e.g. A functioning antenna microwave amplifier or a faulty Sub-Minature Version A (SMA) connector) [2–4, 6, 7]. Further RF-DNA discussion is provided in Section 2.4.

In summary, NDE has the potential to reduce traditional maintenance practice duration, limit servicing damage and delay assembly replacement requirements which

contributes to increased operational availability. As discussed, current NDE equipment can suffer from portability limitations. For electrical and magnetic applications, NDE can be limited by frequency spectrum use restrictions. This research effort targets these two areas with the use of light-weight SDRs and a uniform white noise signal.

## 2.2 Software Defined Radio

An SDR refers to a radio where the majority of the Radio Frequency (RF) front-end functionality, previously performed by hardware, now occurs in software [9]. Ideally, this SDR front-end software would be clocked by Gigahertz sample rate Analog to Digital Converters (ADCs) for reception and Digital to Analog Converters (DACs) for transmission. This allows all signal processing requirements to be performed digitally. However, Gigahertz rate ADCs and DACs are not yet commonly available at a reasonable cost. This requires some functionality to still be provided by an RF Integrated Circuit (RFIC) [9]. Consequently, SDR architecture typically has an RF component and a Digital Signal Processing component.

SDR local oscillator ‘drift’ can be problematic [9]. Frequency synchronization between the transmitter and receiver, or potentially between adjacent receivers, relies on a common frequency reference. The frequency reference is provided by a local oscillator. Local oscillators are subject to different manufacturing tolerances, temperature effects and ageing [9]. Therefore, using multiple SDRs will exacerbate the synchronization problem as each receiver local oscillator and the transmitter local oscillator will ‘drift’ at varying rates.

The Ettus USRP B205-mini SDR and Ettus X310 SDR are used for this research effort. Their respective features and architecture are detailed below.

### **2.2.1 Ettus USRP B205-mini Software Defined Radio**

The Ettus USRP B205-mini SDR features a USB 3.0 controller, Spartan Field Programmable Gate Array (FPGA) and an AD9364 RFIC transceiver [10]. The B205 SDR is shown in Figure 1 and a B205 SDR architecture block diagram is depicted in Figure 2.

The AD9364 receiver component operates in the 70 MHz to 6.0 GHz range, with a maximum instantaneous bandwidth of 56 MHz. Two ADCs are configured to provide In-Phase and Quadrature signals. Each ADC provides a 12-bit resolution and a maximum sampling rate of 61.44 MS/s for digitization [16]. A B205 SDR weighs 24.0 g. When compared with laboratory quality digital oscilloscopes, vector signal analyzers or large signal network analyzers that are typically used for wide-band signal measurement, the B205 SDR is significantly lighter. However, SDRs contain a low-cost receiver module which makes the receiver component susceptible to the aforementioned ‘drift’.

This research effort will attempt to reproduce a signal response with a single B205 SDR using two receive channels. This will be followed by an iterative development process spanning dual and multiple B205 SDRs using a bandwidth expansion technique.

### **2.2.2 Ettus USRP X310 Software Defined Radio**

The Ettus USRP X310 SDR operates in the DC to 6.0 GHz range and has two wide-band daughter boards with a maximum instantaneous bandwidth of up to 120 MHz per channel. The X310 features multiple high speed interfaces including dual 1 Gigabit Ethernet (1G ETH) and 10 Gigabit Ethernet (10G ETH) slots, Kintex 7-410T FPGA and an optional Global Positioning System Disciplined Oscillator (GPSDO) supplying a stable 10 MHz clock reference and a 1 Pulse Per Second (PPS)



Figure 1. Ettus Universal Software Radio Peripheral B205-mini Software Defined Radio [10].

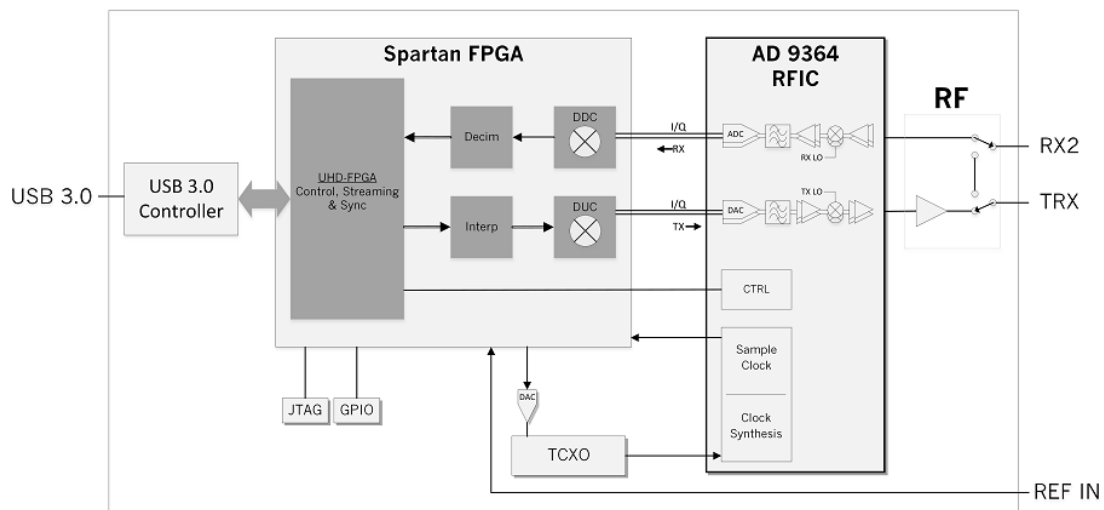


Figure 2. Ettus Universal Software Radio Peripheral B200-mini Software Defined Radio architecture. The architecture is the same as the Ettus B205-mini SDR [10].

timing signal [17]. The X310 SDR is shown in Figure 3. This research effort uses the Ettus X310 to transmit signals for recovery by B205 SDRs.

### 2.2.3 GNU Radio Companion Interface Software

The X310 and B205 SDRs are interfaced with the host-PC using the GRC interface software. GRC is an open source flow-graph software development used to “design, simulate and deploy real-world radio systems” [18]. The open source environment is supported on Wiki, hence the slightly unconventional deferral to Wiki-based references for this section.

The GRC interface software facilitates radio system tests using a flow-graph. The flow-graphs for hardware tests can be seen in Figures 19, 21 and 23. The flow-graphs are comprised of processing blocks with adjustable parameters, connected using ‘complex int 16’ wire format. ‘Complex int 16’ references a data type. In this case, the data type contains both real and imaginary parts, and uses 16-bit signed integers [19]. Flow-graph activation is controlled from a GRC Graphic User Interface (GUI) or through Linux root commands.

Block identification and descriptions are sourced from the Wiki-based GRC processing blocks webpage [18]. The following tables detail the processing block parameters and the intended hardware test values. Table 1 identifies the options block. This block is used to set global parameters. Table 2 describes the variable block. This block maps a value to a unique variable. Table 3 describes the file source block. This block reads raw data values in binary format from the specified file on the host-PC. This binary file is passed to the UHD:USRP sink block. Table 4 describes the UHD:USRP sink block which is used to stream samples to a USRP device. In this case, the USRP device is the X310 SDR. Table 5 describes the UHD:USRP source block. This block is used to stream samples from a USRP device. In this case, the USRP



Figure 3. Ettus Universal Software Radio Peripheral X310 SDR [17].

device is the B205 SDR. The UHD: USRP source block passes samples to the file sink block. Table 6 describes the file sink block which writes a stream to a binary file. Finally, within each UHD: USRP source/file sink block chain is placed a head block and a QT GUI frequency sink block. Table 7 describes the head block. This block copies the specified number of items to the output and then stops. Table 8 describes the QT GUI frequency sink block. This block provides a graphical sink to display multiple signals in a frequency format [18]. Table test values are described when the value remains unchanged for all hardware tests. Where a test value is specific to a hardware test (e.g. Samp rates), the value is addressed in Chapter III.

Table 1. GRC options block [18].

<b>Property</b>	<b>Description</b>	<b>Test Value</b>
ID	ID of the flow-graph	Refer to flow-graph Figures 19, 21 and 23
Title	Title of the flow-graph	Refer to flow-graph Figures 19, 21 and 23
Description	Description of the flow-graph	Refer to flow-graph Figures 19, 21 and 23
Generate options	Specifies GUI use	QT GUI (use GUI with QT Tool format)
Realtime scheduling	Identifies whether the operating system is prioritizing this process or not (root application)	On (prioritize if actioned using root commands)

Table 2. GRC variable block [18].

<b>Property</b>	<b>Description</b>	<b>Test Value</b>
ID	ID of the variable name	Refer to flow-graph Figures 19, 21 and 23
Value	Value of the variable that can be changed in real-time	Refer to flow-graph Figures 19, 21 and 23

Table 3. GRC file source block [18].

<b>Property</b>	<b>Description</b>	<b>Test Value</b>
File	File name of the binary file	txFile#
Repeat	Whether or not to repeat the signal once the end of the file is reached	Yes (repeat the signal)

Table 4. GRC UHD: USRP sink block [18].

<b>Property</b>	<b>Description</b>	<b>Test Value</b>
Wire format	Controls the data type of the input stream over the network	complex int 16
Device address	An address string used to locate UHD devices on the network	serial#
Sync	Synchronizes the USRP with the host PC clock or a 1 PPS signal	unknown 1 PPS (reference the GPSDO 1 PPS signal)
Mb0: Clock source	Identifies where the motherboard should synchronize its clock references	Onboard GPSDO
Mb0: Time source	Identifies where the motherboard should synchronize its time references	Onboard GPSDO
Mb0: Subdev spec	Motherboard sub-device specification	B:0 (Device occupies position B:0)
Samp rate (sps)	The number of samples per second which is equal to the bandwidth we wish to observe	Refer to flow-graph Figures 19, 21 and 23
Ch0: Center freq (Hz)	The center frequency is the overall frequency of the RF chain	2.4 GHz
Ch0: Gain value	The value used for gain, between 0 and the maximum gain of the USRP (typically between 70-90)	40
Ch0: Antenna	Identifies the antenna in use	TX/RX



Table 5. GRC UHD: USRP source block [18].

<b>Property</b>	<b>Description</b>	<b>Test Value</b>
Wire format	Controls the data type of the output stream over the network	complex int 16
Device address	An address string used to locate UHD devices on the network	serial#
Sync	Synchronizes the USRP with the host PC clock or a 1 PPS signal	unknown 1 PPS (reference the GPSDO 1 PPS signal)
Mb0: Clock source	Identifies where the motherboard should synchronize its clock references	external (GPSDO 1 PPS signal)
Samp rate (sps)	The number of samples per second which is equal to the bandwidth we wish to observe	Refer to flow-graph Figures 19, 21 and 23
Ch0: Center freq (Hz)	The center frequency is the overall frequency of the RF chain	2.4 GHz +/- offset variable
Ch0: Gain value	The value used for gain between 0 and the maximum gain of the USRP (typically between 70-90)	50
Ch0: Antenna	Identifies the antenna in use	RX2

Table 6. GRC file sink block [18].

<b>Property</b>	<b>Description</b>	<b>Test Value</b>
File	Specifies the file name to open and write output to	rxFile#
Unbuffered	Specifies whether the output is buffered in memory	On (unbuffered)
Append file	Specifies whether the file should be appended to or a new file should be created each time	Overwrite (new file)

Table 7. GRC head block [18].

<b>Property</b>	<b>Description</b>	<b>Test Value</b>
Num items	Number of samples to copy	100 MS or 1 GS

Table 8. GRC QT GUI frequency sink block [18].

<b>Property</b>	<b>Description</b>	<b>Test Value</b>
FFT size	Size of the FFT to compute and display	2048 KS
Center frequency (Hz)	Center frequency for x-axis	Refer to flow-graph 19
Bandwidth (Hz)	Bandwidth for x-axis	Refer to flow-graph Figure 19

## 2.3 Bandwidth Expansion Principles

This research effort aims to demonstrate NDE wide-band signal response collection simultaneously spanning multiple SDR narrow-band receiver bandwidths. For the intended NDE application a single SDR narrowband receiver bandwidth (sub-band) would be insufficient to collect a wide-band signal suitable for accurate signal response reconstruction.

Ideally, a transmitted wide-band signal should be perfectly reconstructed at the receiver. However, the transmitter, propagation environment and receiver imparts noise, phase and frequency effects [9]. Ignoring noise for now, the received signal will have a frequency and phase offset. Frequency offset can cause error with subsequent phase offset correction limiting the accuracy of sub-band realignment. This is a concern given frequency offset is likely to be more common with low-cost receivers (e.g. SDR receivers) due to ‘drift’. Drift is associated with lower-tolerance components [9].

WSS bandwidth expansion techniques use a single narrowband receiver to collect a sub-band. The sub-band is stored and the same narrowband receiver is used to collect the next sub-band. This is repeated until all sub-bands are collected for signal processing, including frequency and phase correction. This is a suitable approach for time invariant signals that reduces hardware requirements. While our application involves non-WSS signals, it is useful to review WSS bandwidth expansion techniques because:

- WSS techniques provide insight into bandwidth expansion principles.
- WSS techniques highlight bandwidth expansion limitations likely to be encountered during this research effort.

WSS bandwidth expansion measurement techniques are discussed in Section 2.3.1

and WSS bandwidth expansion reference techniques are discussed in Section 2.3.2.

Non-WSS, time-variant signals require simultaneous collection potentially spanning multiple SDR receivers. Section 2.3.3 addresses non-WSS bandwidth expansion techniques.

### 2.3.1 Wide Sense Stationary Measurement Techniques

A WSS bandwidth expansion technique can achieve consecutive sub-band time alignment by overlapping part of a sub-band bandwidth with part of the adjacent sub-band bandwidth. Time alignment is achieved using a frequency tone common to both sub-bands in the overlapping frequency spectrum [20]. Where bandwidth overlap is used and the frequency tone forms part of the measured signal (internal reference) the technique is termed a measurement, or a ‘stitched’, technique [20].

Figure 4, adapted from Wisell [21], depicts the sub-band overlap. The depiction shows adjacent sub-bands overlapping half of each narrowband receiver bandwidth. For a measurement technique, the phase difference, between a frequency tone (not shown) common to both sub-bands (i.e. common to the frequency bandwidth  $\Delta f$ ), would provide the basis for sub-band time-alignment.

#### 2.3.1.1 Cross Correlation Maximization

Wisell, et al. progressively build the wide-band response bandwidth with a single receiver, using cross-correlation maximization. The cross-correlation maximization method requires that two assumptions hold:

- The signal is time invariant for the entire measurement duration;
- The signal is repetitive.

Each sub-band,  $1, 2, \dots, M$ , is collected and stored, before the next sub-band is collected for storage.  $N$  signal measurements are made for each sub-band. The

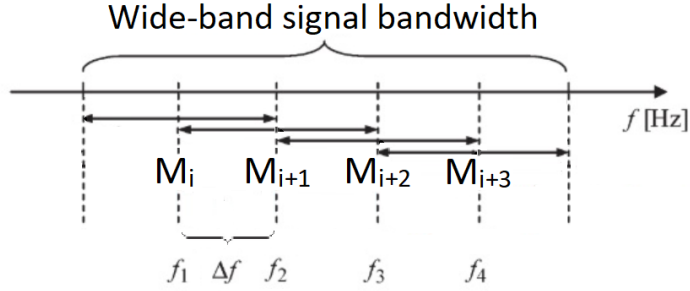


Figure 4. Bandwidth expansion using overlapping frequency bandwidths. Narrow-band receiver bandwidths (sub-bands) indicated by  $M_i$ ,  $M_{i+1}$ ,  $M_{i+2}$  and  $M_{i+3}$  with center frequencies  $f_1$ ,  $f_2$ ,  $f_3$  and  $f_4$ , are overlapped using an internal reference. Sub-band spacing is denoted by  $\Delta f$  and is represented as half the usable bandwidth [21].

signal measurements provide samples for an averaging process using least squares estimation [21]. The averaging process is inconsequential to this research effort, but is noted here to facilitate explanation of the equation variables. Each received sub-band signal is down-converted and sampled.

A coarse time-domain cross-correlation is applied to effect time-alignment (sample-based) of each sub-band. The time domain cross-correlation is,

$$\left| \sum_{n=n_{0,i}}^{n_{0,i}+L-1} m_0(n) m_i^*(n - n_{0,i}) \right|, \quad (1)$$

where the discrete time domain signals,  $m_0[n]$ ,  $m_1[n]$ ,  $\dots$ ,  $m_{M-1}[n]$ , each contain  $L$  samples,  $m_0$  is the initial collection,  $n_{(0,i)}$  is the delay, based on the  $N$  time-aligned signal measurements with regard to  $n_0$ , and  $i = 1, 2, \dots, M - 1$  [21].

The signal is then reconstructed in the frequency domain using the overlapping parts of each sub-band. Each sub-band must first undergo a Discrete Fourier Transform (DFT). For the upcoming discussion,  $M_i^+$  is the frequency domain representation of the upper-half of the sub-band  $M_i$  and  $M_{i+1}^-$  is the lower-half of the sub-band  $M_{i+1}$ .

The sub-bands, along with their center frequencies are identified in Figure 4 [21].

$M_i^+$  and  $M_{i+1}^-$  are cross-correlated in the frequency domain. The spectral cross-correlation is,

$$\sum_{k=0}^{P-1} M_i^+(k) [M_{i+1}^-(k) e^{(-j2\pi k n_{(0,i+1)})}]^*, \quad (2)$$

where  $P$  is the number of overlapping frequency bins,  $k$  is the frequency bin index and  $n_{(0,i+1)}$  is the delay, based on the  $N$  time-aligned signal measurements with regard to  $n_0$ , and  $i = 1, 2, \dots, M - 1$  [21].

The maximum of (2) provides for the spectral alignment of  $M_{i+1}^+(k)$  (i.e. the upper-half of the sub-band  $M_{i+1}(k)$ ).  $M_{i+1}^+(k)$  is then concatenated with  $M_i(k)$  (i.e.  $M_{i+1}^-(k)$  is removed). The process is repeated for overlap  $M_2^+(k)$  and  $M_3^-(k)$ , through to  $M_{P-1}^+(k)$  and  $M_P^-(k)$  reconstructing the frequency spectrum of the time-aligned sub-bands [21].  $S_{mea}(k)$  describes the frequency spectrum,

$$S_{mea}(k) = [M_1(k)M_2^+(k)e^{(j2\pi k n_{0,2})}, \dots, M_P^+(k)e^{(j2\pi k n_{0,P})}], \quad (3)$$

While the amount of overlap indicated here ( $\Delta f$ ) is half a sub-band bandwidth, the amount of overlap is not set. However, the overlap must include frequency tones coincident to both sub-bands [21]. Once all adjacent sub-bands are aligned (3) undergoes an Inverse Discrete Fourier Transform (IDFT) to restore the time domain signal.

The cross-correlation maximization technique uses a single receiver to make consecutive sub-band collections. This would be unsuitable for this research effort as

the uniform white noise signal is time-varying. The need to collect signal sub-bands over a period of time would not allow for accurate transmit signal reconstruction. To overcome this issue, this research effort will use multiple SDRs. The SDR collection times will be synchronized. Each SDR receives a different sub-band, with the sum of sub-bands spanning the transmitted signal bandwidth.

A recent research effort successfully adapted the cross-correlation maximization technique using two simultaneous SDR receiver collections [8]. Section 2.3.3 provides further details regarding [8], including the need for simultaneous collection as the time-invariant and repetitive signal assumptions did not hold.

### 2.3.1.2 Phase De-trending

The process of phase alignment is critical to bandwidth expansion signal reconstruction. Remley, et al. apply a phase alignment technique known as ‘phase de-trending’ to multisine signal frequency tones [22]. Phase detrending is a two-step process that restores a reference time ( $t_{ref}$ ) by identifying the phase difference between two adjacent frequency tones at a specified measurement time ( $t_m$ ). The first step provides a coarse time-shift estimate ( $t_{ref} - t_m$ ). The coarse time-shift estimate is,

$$(t_{ref} - t_m)_{est} = \frac{[\theta_{i+1}(t_m) - \theta_{i+1,exp}] - [\theta_i(t_m) - \theta_{i,exp}]}{2\pi(f_i - f_{i+1})}, \quad (4)$$

where  $\theta_i(t_m)$  is the measured phase of the  $i$ th frequency tone,  $\theta_{i,exp}$  is the expected phase of the  $i$ th frequency tone and subscripts  $i$  and  $i + 1$  again refer to adjacent sub-bands [22]. The numerator identifies a phase difference between two frequency tones. The phase difference falls between 0 and  $2\pi$ .

Remley acknowledges the measured phase seldom reflects the expected phase due to “signal generation, measurement and distortion errors” [22]. Therefore, the second

step refines the coarse estimate using an error minimization function to ‘detrend’ the phase. The global error minimization function is,

$$E(t) = \sum_{i=1}^N |\theta_i(t) - \theta_{i,exp}|^2, \quad (5)$$

where  $N$  is the number of frequency tones [22]. The global minimum of (5) provides the best estimate of  $t_{ref}$ . Here the linear phase shift in the frequency domain is considered as a delay in the time domain. In this manner, the delay can time-align or restore  $t_m$  to  $t_{ref}$  [22]. Once  $t_{ref}$  is restored,  $\theta_i(t_{ref})$  for each frequency tone  $f_i$  is,

$$\theta_i(t_{ref}) = \theta_i(t_m) + 2\pi f_i(t_{ref} - t_m), \quad (6)$$

Remley, et al. state that phase alignment can be extended to other frequency components [22], but it is not supported by provided examples, nor inferred that this applies to all sub-band frequency components.

Remley’s (4) [22] coarse estimate relies on precise frequency  $f_i$  and  $f_{i+1}$  for the time-shift. Wisell’s (2) [21],  $M_i$  and  $M_{i+1}$  sub-bands centered on frequency  $f_i$  and  $f_{i+1}$  respectively, also rely on precise  $f_i$  and  $f_{i+1}$  to locate the cross-correlation maximum for the time-shift.

In summary, Remley’s phase detrending technique uses a consecutive collection process and requires the signal to be repetitive. This is inconsistent with the requirements for the uniform white noise signal that is intended for this research effort. Importantly, Remley, et al. identify a critical issue that will affect our research effort. The issue is that an imprecise frequency correction will increase error, reducing



phase estimate accuracy. This is significant. Bandwidth expansion does not tolerate frequency drift which is particularly acute with SDRs [9]. Frequency sensitivity to local oscillator drift will need to be addressed in both single, dual and multiple SDR cases.

### 2.3.2 Wide Sense Stationary Reference Techniques

A WSS bandwidth expansion technique achieving consecutive sub-band alignment using a ‘pilot signal’ to time-align frequency tones is termed a reference technique [20]. Figure 5, adapted from [21], depicts the adjacent sub-band alignment. The pilot signal and the individual frequency tones required for alignment are not shown.

#### 2.3.2.1 Pilot Signals

Zenteno, et al. add a known a priori ‘pilot’ signal, for use as a time reference to reconstruct a wide-band signal. The wide-band signal bandwidth extends beyond the measured signal bandwidth of a single receiver. The pilot signal is added to the signal of interest and must span each measured signal bandwidth [20]. The number of receivers required to span the wide-band signal bandwidth is given by  $M$ .

The measured signal model is,

$$r_i = x_i + p_i, \tag{7}$$

where  $x_i$  is the signal of interest and  $p_i$  is the pilot signal and subscript  $i$  indexes the  $i$ th measured sub-band used to reconstruct the wide-band signal [20]. Both  $x_i$  and  $p_i$  are complex vectors of length  $N$ .

The frequency domain representation of the measured signal is,

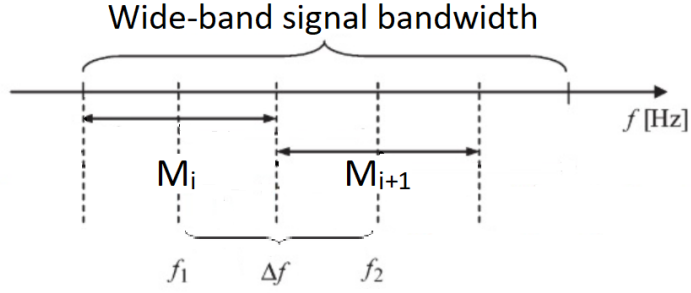


Figure 5. Bandwidth expansion using aligned frequency bandwidths. Narrow-band receiver bandwidths (sub-bands) are indicated by  $M_i$  and  $M_{i+1}$  with center frequencies  $f_1$  and  $f_2$ , aligned adjacent to the next sub-band using a pilot tone. Sub-band spacing is denoted by  $\Delta f$ . There is no overlap between sub-bands, however alignment ensures the wide-band signal bandwidth is contiguous [21].

$$R_i = X_i + P_i, \quad (8)$$

where  $X_i$  is the frequency domain representation of the signal of interest and  $P_i$  is the frequency domain representation of the pilot signal [20]. Both  $X_i$  and  $P_i$  are complex vectors of length  $N$ .

Zenteno's aim is to rebuild the wide-band signal bandwidth ( $Y$ ) representing the signal of interest ( $X$ ) with the effects of the pilot signal ( $P$ ) removed [20]. However, each sub-band  $X_i$  has been subjected to unknown time ( $\Delta_i$ ) and phase delay ( $\psi_i$ ) effects. The wide-band signal is,

$$Y = QX, \quad (9)$$

where  $Q$  is a diagonal matrix of dimension  $M$  [20].  $Q_i$  describes the unknown time

$(\Delta_i)$  and phase delay  $(\psi_i)$  effects on  $X_i$  [20].  $Q_i$  is,

$$Q_i = Q_i(\Delta_i, \psi_i) = e^{(-j\frac{2\pi k}{N}\Delta_i + \psi_i)} I_N \quad (10)$$

where  $k \in [\frac{-N}{2}, \dots, \frac{N}{2} - 1]$ ,  $N$  is the length of the measured signal complex vector and  $I$  is an identity matrix of dimension  $N$  [20]. Estimating  $(\Delta_i, \psi_i)$  for the  $M$  receivers relies on a least squares approximation using the known pilot signal time delay and phase delay as reference values. This allows the wide-band signal frequency domain representation to be rebuilt. The approximation does not contribute to this research effort and is not discussed here. A non-linear least squares technique is discussed in Section 2.3.3. Once all adjacent sub-bands are aligned, the wide-band signal frequency representation undergoes an IDFT to restore the time domain signal.

The pilot signal technique reduces receiver hardware requirements due to the adjacent sub-band alignment [20]. This would be beneficial to this research effort. The auto-correlation technique employed by this research exploits the use of adjacent sub-band alignment vice overlapping sub-bands.

The pilot signal must span the wide-band signal bandwidth [20]. This places an additional requirement on the signal generator. This research aims to reduce the complexity of a developed NDE device. Exploiting the technique would involve a trade-off between increasing transmitter complexity versus a reduction in the number of SDR receivers.

The measured signal must also be repetitive [20]. This negates use of the intended uniform white noise signal. For this reason the pilot signal technique is not used.

### 2.3.2.2 Wide Sense Stationary Signal Summary

The WSS bandwidth expansion techniques discussed in [20–22] are unsuitable for time-variant signals. Aforementioned techniques require the signal to be repetitive.

The uniform white noise signal is not repetitive. A single receiver is also unlikely to collect all sub-bands before the signal changes. The uniform white noise signal is time-varying, rendering stored sub-bands unusable.

The WSS review has identified the need for precise frequency correction, to ensure accurate phase estimates. The next section reviews non-WSS bandwidth expansion techniques which are more closely aligned to our problem.

### **2.3.3 Non-Wide Sense Stationary Techniques**

Time variance imposes two signal collection and processing requirements. First, the entire signal must be collected simultaneously and second, if the entire signal is collected as a series of sub-bands, sub-band frequency and phase must subsequently be synchronized. The first requirement is achieved simply by determining the receiver instantaneous bandwidth and calculating the number of SDRs required to span the wide-band signal bandwidth. The second requirement is more problematic, with consideration of time, frequency and phase synchronization needed.

Section 2.3.3 reviews non-WSS techniques used for frequency and phase synchronization, including Phase Locked Loops, non-data aided feed-forward estimation and phase correction using cross-correlation for simultaneously collected signals.

#### **2.3.3.1 Phase Locked Loops**

Analog Phase Locked Loops (PLLs) reconstruct a transmit carrier signal replica using the input carrier signal as a reference. The PLL Voltage Controlled Oscillator (VCO) output is periodically adjusted to keep phase error between the input carrier signal and the replica carrier signal at zero [23]. To synchronize the transmit and receive signals the PLL must acquire and track the input carrier signal frequency and phase. Figure 6 shows a basic PLL diagram.

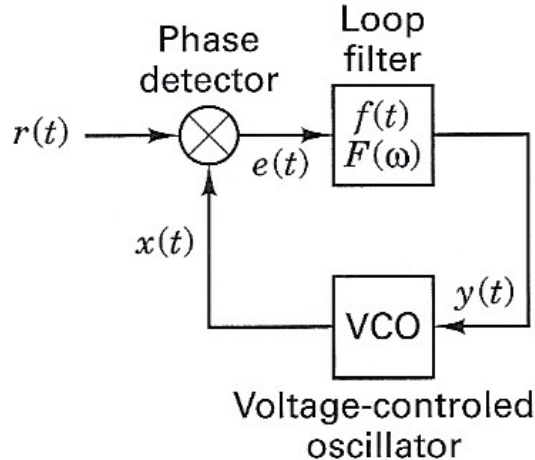


Figure 6. A Basic Phase Locked Loop Diagram [24].

In a steady-state, the phase detector determines phase difference ( $e(t)$ ) between the received input carrier signal ( $r(t)$ ) and the VCO output replica carrier signal ( $x(t)$ ). The loop filter ( $f(t)$ ), described by its Fourier response ( $\mathcal{F}(\omega)$ ), removes higher frequencies from ( $e(t)$ ) before the linear filtered voltage is input to the VCO. The VCO converts the linear filtered input voltage ( $y(t)$ ) to the output replica carrier signal ( $x(t)$ ) accounting for any phase error. ( $x(t)$ ) is input to the phase detector for the next tracking loop evolution [24].

The digital PLL has component, implementation and performance differences but serves the same purpose. Typically, a numerical controlled oscillator replaces the VCO, the phase detector is replaced with a discriminator, and the digital equivalent of an analog loop filter is applied.

Historically, communication systems used a feed-back mechanism for frequency and phase synchronization. Early analog PLL complexity made the PLL “economically unfeasible” for most applications [19]. However, a recent research effort demonstrated the use of a digital PLL applied to the bandwidth expansion problem [25]. The research effort reconstructed two overlapping frequency bandwidth receiver inputs. Neither receiver input spanned the full transmit signal bandwidth. The input

phases were synchronized, after pulse shaping, using a digital PLL. The digital PLL incorporated a phase detector, loop filter and digital data synthesizer.

The GRC conference presentation [25] details for the research effort are not extensive. However, experimental results with a Bit Error Rate (BER) better than  $10^{-5}$  at an Energy per Bit to Noise Power Spectral Density ( $E_b/N_0$ )= 10 are indicated [25]. BER infers a communications signal, although this is not explicitly stated in [25]. This research uses Symbol Error Rate (SER) versus Energy per Symbol to Noise Power Spectral Density ( $E_s/N_0$ ) metrics. Further symbol recovery measurement details are found in Section 3.1.4.

PLLs provide accurate phase measurement but are susceptible to dynamic stress. Dynamic stress presents as large variations in the input signal frequency. The Frequency Locked Loop (FLL), while providing less accurate phase measurement, is more tolerant to dynamic stress [23]. Kaplan describes a Global Positioning System (GPS) digital carrier tracking loop implementation that uses a FLL assisted PLL or ‘pull-in’ technique [23]. FLL assisted PLL tolerates dynamic stress and retains phase measurement accuracy. Figure 7 shows a basic FLL assisted PLL loop filter [23].

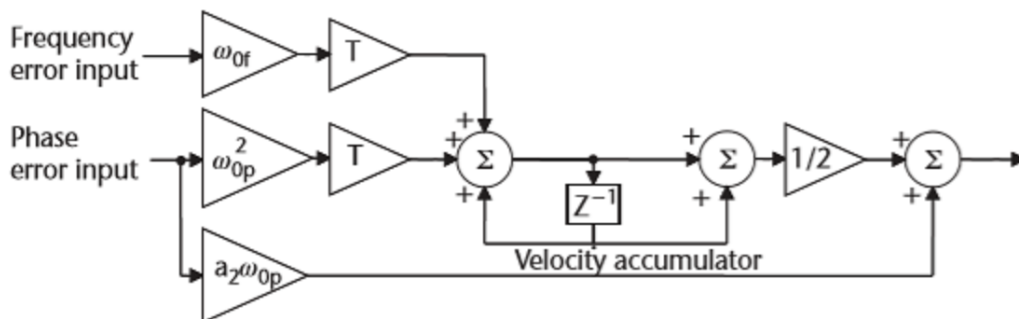


Figure 7. A first order frequency locked loop assisted second order phase locked loop diagram [23].

FLL assisted PLL occurs in the digital loop filter. The initial phase inputs are zeroed and a wide-band discriminator frequency error output is applied to establish

phase lock. Kaplan provides examples of three common FLL discriminator algorithms [23]. The algorithms vary, but generally apply a cross or dot product of the input in-phase and quadrature samples, over the time difference between the input samples. The output is a frequency error. An example FLL discriminator algorithm from Kaplan is,

$$\frac{I_1 \times Q_2 - I_2 \times Q_1}{t_2 - t_1}, \quad (11)$$

where  $I$  is an in-phase sample,  $Q$  is a quadrature sample,  $t$  is the time when the samples were taken and subscripts 1 and 2 indicate time 1 and 2 respectively [23].

The FLL tracking loop bandwidth is iteratively reduced to ‘pull-in’ the frequency error. Once phase lock is achieved the FLL transitions to a PLL. The PLL also iteratively reduces its tracking loop bandwidth until a steady state is achieved. If phase lock is lost the process resets and repeats [23].

The ‘closed-loop’ FLL assisted PLL technique resolves the precise frequency correction and accurate phase estimate requirement. One of the stated aims of this research effort is to provide a light-weight, low-complexity and low-cost solution to the bandwidth expansion problem. The author is not convinced that the Air Force Institute of Technology (AFIT) provided PLL software code met the low-complexity criteria. Consequently, a simplification of the technique is used for this research that limits the ‘pull-in’ process to three iterations.

### 2.3.3.2 Non-Data-Aided Feed-Forward Frequency Estimation

Besson [26] and Wang’s [27] respective papers describe non-data-aided feed-forward carrier frequency offset estimation methods. Their respective works are not specific to bandwidth expansion, however, the arguments could be adopted for sub-band frequency alignment. A non-data aided method does not rely on a priori knowledge of the detected symbols for carrier or clock recovery [28]. Besson and Wang’s meth-

ods, instead, exploit data embedded within the transmission signal, non-linear least squares estimation and squaring loop principles to provide a frequency offset estimate.

A squaring loop establishes an index for carrier recovery. A received carrier with signal level symmetric about zero does not provide useful information regarding the transmitted carrier. Squaring the received signal generates power in a frequency component at twice the carrier frequency. This frequency component can then be filtered to provide an index for carrier recovery [29].

The model used by Besson [26] is,

$$y(t) = \alpha x(t)e^{j\omega_0 t} + e(t) \quad t = 0, 1, 2, \dots, \quad (12)$$

where “ $\alpha$  is a complex-valued amplitude,  $x(t)$  is a real-valued time-varying envelope,  $\omega_0$  is the frequency and  $e(t)$  is a disturbance” [26].

Besson finds a frequency estimate by manipulating a squared-loop application of (12) to meet a non-linear least squares criterion. The least squares criterion is,

$$\sum_{t=0}^{N-1} |y(t) - \alpha x(t)e^{j\omega_0 t}|^2, \quad (13)$$

where  $N$  is the number of samples [26]. The squaring loop is repeated  $N$  times to identify the  $\omega_0$  that minimizes (13) [26].

The frequency offset estimation method derived in [26] applies the frequency estimate to a Binary Phase Shift Keying second order modulation. Wang applies a variation of the estimation method to a Quadrature Phase Shift Keying (QPSK) signal. QPSK modulation order requires fourth order values but the principles are transferable [27].

Two key equations resulting from [27] are adopted for bandwidth expansion. The first equation finds the global maximum, instead of the global minimum in [26], of a



least squares equation to provide a frequency estimate. The frequency offset estimate derivation is provided in Appendix 5.1.4. The global maximum of the frequency estimate is,

$$f_{est} = \frac{1}{4} \left( \frac{1}{N} \sum_{n=0}^{N-1} |y^m(n) e^{-j2\pi f(n)}|^2 \right), \quad (14)$$

where  $m$  is the modulation order,  $n$  is the sample index,  $N$  is the number of samples,  $y$  is the received signal and  $f$  is the expected carrier frequency [27]. The second equation applies the frequency estimate (14) to compensate for the frequency offset. The frequency compensation equation is,

$$f_{comp} = y e^{-j2\pi f_{est}(n)}, \quad (15)$$

In practice, a QPSK received signal is raised to the fourth power, then undergoes a DFT with a high oversampling rate (e.g.  $2^{23}$  S/s) [27]. The global maximum is identified in the resultant frequency response. The position index at  $\frac{1}{4}$  the global maximum position index is  $f_{est}$ . Substituting  $f_{est}$  of (14) into  $f_{comp}$  of (15) restores the carrier frequency.

It was identified after the initial QPSK simulation, described in Section 3.1, that the frequency offset estimation technique was not appropriate for the uniform white noise signal. The technique exploits signal cyclo-stationary (CS) statistics. CS statistics are readily found in M-ary shift keying signals [26, 27] but are absent in noise.

### 2.3.3.3 Phase Correction of Simultaneous Collections

Accurate phase recovery requires a precise frequency overlap between adjacent sub-bands. An ideal frequency overlap minimizes phase error attributable to frequency mismatch. The phase correction technique described here was identified in a recent AFIT research effort [8].

The frequency estimator (14) described in Section 2.3.3.2 can be used to provide the position index for a QPSK frequency estimate. Alternately, as proposed in [8] cross-correlating the frequency spectra of adjacent overlapping sub-bands will provide a coarse position index. The position index identifies the frequency offset. Review of the spectral cross-correlation technique shows similarities to the approach described in Section 2.3.1.1, however (2) requires over-sampling to effect a least squares solution. The spectral cross-correlation technique, used in [8], does not seek a non-linear least squares solution.

The cross-correlation equation presented in [30] with time domain variables can be substituted for frequency domain variables. This is due to the Fourier Time / Frequency duality principle. The frequency domain cross-correlation is,

$$C_{XY}[l] = \sum_{-\infty}^{\infty} \{X[k] Y^*[k+l]\} \quad -\infty < l < \infty, \quad (16)$$

where  $X[k]$  are DFT coefficients of the first received sub-band,  $Y^*[k+l]$  is the complex conjugate of the DFT coefficients of the second received sub-band with frequency shift  $[l]$  and  $*$  is the complex conjugate [30].  $C_{XY}$  at lag  $[l]$  presents as a frequency shift. The lag is applied to frequency align the sub-bands.

For phase correction, adjacent frequency domain spectra are overlapped using the frequency cross-correlation technique described. The sub-band overlapping portions are band-pass filtered before an IDFT restores the overlapping portions to the time

domain. The overlapping portions are then cross-correlated. The time domain cross-correlation is,

$$C_{xy}[m] = \sum_{-\infty}^{\infty} \{x[n] y^*[n+m]\}, \quad -\infty < m < \infty, \quad (17)$$

where  $x[n]$  is the first restored overlapping sub-band,  $y^*[n+m]$  is the complex conjugate of the second restored overlapping sub-band at delay  $[m]$  and  $*$  is the complex conjugate [30].  $C_{xy}$  at lag  $[m]$  presents as a delay. The delay is applied to time-align the sub-bands, not just the overlapping portions.

The research effort culminated in the reconstruction of a 2 MHz QPSK transmit signal using two SDRs [8]. Each SDR was band-limited, able to recover a 1 MHz sub-band. The SDR selected center frequencies provided a sub-band overlap of 20 kHz resulting in a recombined signal spanning 1.98 MHz. The processed signal exhibited accurate QPSK symbol recovery. The research did not extend the process to multiple sub-bands, nor did it investigate the uniform white noise signals explored in this research.

#### 2.3.3.4 Non-Wide Sense Stationary Signal Summary

The non-WSS bandwidth expansion techniques use simultaneous signal collection approaches. Further, the PLL and the simultaneous phase correction techniques do not require a repetitive signal. However, each technique only provides a partial solution to the current problem. The PLL technique requires complex code, the frequency estimate technique is limited to M-ary signals and the phase correction technique has not been proven across multiple sub-bands.

Consequently, this research effort attempted to develop the phase correction technique, in [8], to multiple sub-bands. As stated, the approach was abandoned in

favor of an auto-correlation technique. While it would be customary to include auto-correlation background discussion here, the reader is directed to Section 3.2.1 and Section 3.2.2 for further detail on the auto-correlation technique used in this research effort.

## 2.4 Device Classification

Device characterization afforded by RF-DNA has its origins in authorized device identification and rogue detection [31–33]. More recently, research efforts have shown RF-DNA is suitable for fault condition characterization during device assembly, acceptance testing and in-service scenarios [2–7]. Generally, RF-DNA processing requires signal collection, statistical fingerprint generation, device training and classification.

### 2.4.1 Signal Selection

As discussed, concurrent frequency spectrum use requires a non-intrusive interrogation signal. A uniform white noise signal meets this requirement due its low average power. Average power  $P_a$ , being a key determinant in signal detection [34], is calculated as,

$$P_a = P_t \frac{\tau}{T}, \quad (18)$$

where  $P_t$  is peak power,  $\tau$  is signal duration and  $T$  is the pulse repetition interval [35]. As can be seen, for fixed  $\tau$  and  $T$  values  $P_a$  is determined solely by  $P_t$  [35]. Low Probability of Intercept (LPI) systems using a low-continuous  $P_t$  spread over the duty cycle can achieve detection performance equivalent to conventional systems that use high  $P_t$  and short  $\tau$ . LPI systems mitigate low-continuous  $P_t$  by increasing  $\tau$  until a unity duty cycle is achieved [34]. The duty cycle is,

$$d_c = \frac{\tau}{T}. \quad (19)$$

Consequently uniform white noise signal low peak-to-average power ratio and wide bandwidth results in a signal that is difficult to detect and classify without a priori knowledge. Further, a uniform white noise signal provides a uniformly distributed power throughout the sampled spectrum (i.e. a ‘flat’ power spectral density) which assists with DUT resonant response optimization [2]. These characteristics make the uniform white noise signal a valid NDE stimulation signal candidate.

A uniform white noise signal is derived using repeated random variable sampling from a uniform Probability Mass Function (PMF) defined as,

$$p_u(r) = U(r; r_1, r_2) = \begin{cases} \frac{1}{r_2 - r_1}, & r_1 \leq r \leq r_2 \\ 0, & \text{otherwise,} \end{cases} \quad (20)$$

and is characterized by its mean ( $\bar{r}$ ) and variance ( $\sigma_r^2$ ) [12]. The mean ( $\bar{r}$ ) for a uniform noise PMF is,

$$\bar{r} = \frac{1}{2}(r_2 + r_1), \quad (21)$$

and the variance ( $\sigma_r^2$ ) for the uniform PMF is,

$$\sigma_r^2 = \frac{(r_2 - r_1)^2}{12}. \quad (22)$$

The development of the simulation and hardware test uniform white noise signal is

discussed further in Section 3.1.2.2.

### 2.4.2 Signal Collection

Signal collection requires a single SDR receiver or multiple SDR receivers dependent on bandwidth recovery requirements. Bandwidth being the primary consideration for improving signal reconstruction as identified in [6]. Lukac’s findings are consistent with Hartley’s Law, where the information ( $I$ ) gained is,

$$I \propto \beta \times \tau, \tag{23}$$

where  $\beta$  is the signal bandwidth and  $\tau$  is the signal duration [19]. Assuming  $\tau$  is fixed, the information gained depends solely on the available bandwidth. Further information on SDRs was provided in Section 2.2.

### 2.4.3 Fingerprint Generation

Fingerprint generation is reliant on features sourced from the collected signal [2–4, 6, 7, 32]. Features are many and varied. Reviewed articles use instantaneous amplitude ( $a(t)$ ), instantaneous frequency ( $f(t)$ ) and instantaneous phase ( $\phi(t)$ ) [2–4, 6, 7, 32], Power Spectral Density [5], discrete Gabor transforms [5, 33], complex wavelet transforms [31] and slope-based Frequency Shift Keying (FSK) features [36].

Statistical variance ( $\sigma^2$ ), skewness ( $\gamma$ ) and kurtosis ( $\kappa$ ) are calculated for signal feature sub-regions of interest. This reduces feature dimensionality, data storage and processing duration [31]. Standard statistical equations for variance, skewness and kurtosis of sequence  $\{x\}$  are given by,

$$\sigma_x^2 = \frac{1}{N_x} \sum_{k=1}^{N_x} [x(k) - \bar{x}]^2, \tag{24}$$

$$\gamma_x = \frac{1}{\sigma^3 N_x} \sum_{k=1}^{N_x} [x(k) - \bar{x}]^3, \quad (25)$$

$$\kappa_x = \frac{1}{\sigma^4 N_x} \sum_{k=1}^{N_x} [x(k) - \bar{x}]^4, \quad (26)$$

where  $\bar{x}$  denotes the sequence mean value. The resultant statistics (24), (25) and (26) are concatenated to form sub-region DNA markers,

$$F_{R_i} = [\sigma_{x_i}^2 \ \gamma_{x_i} \ \kappa_{x_i}], \quad (27)$$

where  $F_{R_i}$  is the regional feature vector and subscript  $i$  indicates the  $i$ th sub-region [32]. These markers are concatenated to form RF-DNA characteristic fingerprints,

$$F^C = [F_{R_1} : F_{R_2} : \dots : F_{R_{(N_R+1)}}], \quad (28)$$

where  $:$  denotes vector concatenation,  $F^C$  is the composite fingerprint vector and  $N_R$  is the number of sub-regions [32].

#### 2.4.4 Device Training and Classification

RF-DNA composite fingerprint vectors are arbitrarily separated into two subsets; a device training subset and a test (classification) subset. Multiple Discriminant Analysis (MDA), a variation on the Fisher Linear Discriminant (FLD) analysis approach, is commonly applied in RF-DNA device training [2–4, 6, 31, 32, 36, 37]. The purpose of discriminatory analysis being to separate samples into classes based on a

feature or features.

The FLD algorithm projects  $d$  dimensions onto a line. The aim is to find the projection line orientation ( $W$ ) that maximizes the ratio of sample “between-class scatter” while minimizing “within-class scatter” [38]. For multi-dimensional scenarios the projection line can become cluttered, with sample class separation becoming confused [38]. MDA projects  $d$  dimensions onto  $c - 1$  planes (assumes  $c < d$ ), with orientation represented by norm vectors  $W_n$  where  $n \in \{1, 2, \dots, c - 1\}$  planes.  $W_n$  for  $c - 1$  planes is assessed for maximum Euclidean distance between classes and minimum single class scatter in the projection space. The optimal plane is denoted  $W_{best}$  [31]. The remaining requirement is to determine class decision boundaries.

For RF-DNA classification, Maximum Likelihood Estimation (MLE) is one technique used to determine best estimate values for the class decision boundaries. The decision boundary values are estimated, assuming a normal distribution, to maximize the probability of obtaining the samples in the device training subset [38].  $W_{best}$  is partitioned by the decision boundaries. The test subset is then projected onto  $W_{best}$  with classification determined solely by the projected fingerprint characteristic location relative to the plane decision boundaries. The boundaries are established during training [31]. Further information on MDA and MLE can be found in [2–4, 6, 31, 32, 36–38].

Figure 8 shows a three-dimensional projection of a device training subset onto two planes. Plane orientation is indicated by norm vectors  $W_1$  and  $W_2$ . The training subset projection onto the plane represented by norm vector  $W_1$  clearly shows preferable between-class scatter when compared with the plane represented by norm vector  $W_2$ . There is some within-class scatter variation for the training subset between the two planes, however,  $W_1$  provides the optimal outcome  $W_{best}$ . MLE then determines the class boundaries for the plane represented by norm vector  $W_{best}$ . A simulated



classification test set projection is shown in Figure 9.

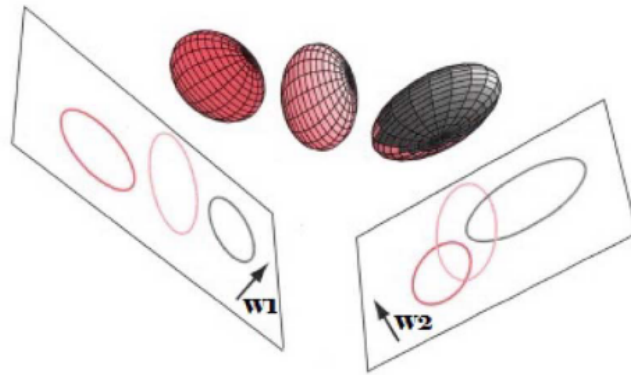


Figure 8. Multiple Discriminant Analysis three-dimensional sub-space projection onto two planes [39]. The two planes are identified by their norm vectors  $W_1$  and  $W_2$  which describe plane orientation. MDA aims to identify the plane orientation that maximizes between-class scatter (spreading) while minimizing within-class scatter (clustering) separation. The plane represented by norm vector  $W_1$  shows maximum between-class scatter and is selected in preference to the plane represented by norm vector  $W_2$ .

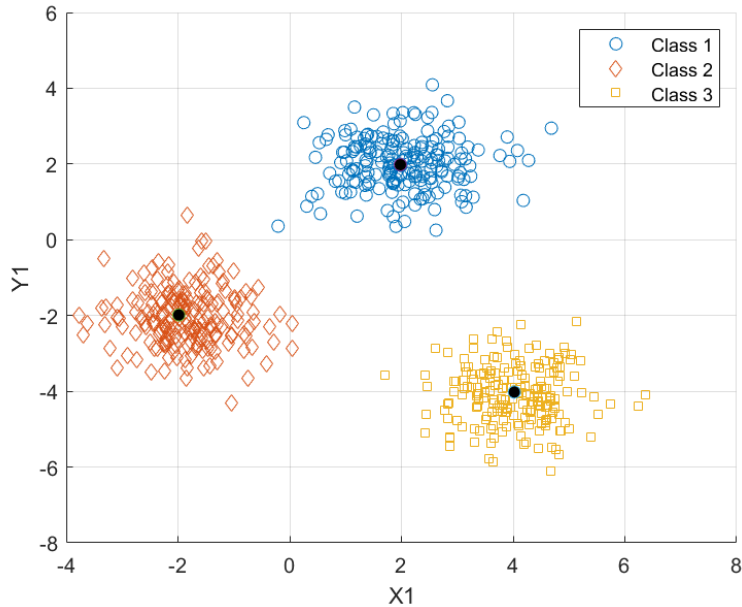


Figure 9. A Fisher plane subspace showing a three device classification [33]. The Fisher space is partitioned along class boundaries (not shown) with the test subset classification determined solely by sample location within respective class boundaries. The sample data shows good between-class scatter (mean separation) and good within-class scatter (clustering). The black dots indicate respective class mean centroids.

## 2.5 Summary

Chapter II provided theoretical background and a review of bandwidth expansion research. Section 2.1 defined NDE and presented further argument for the development of a NDE device; Section 2.2 described SDR technology and detailed Ettus USRP B205-mini SDR, the Ettus USRP X310 SDR features and architecture, as well as an overview of the GRC interface software; Section 2.3 described WSS and non-WSS bandwidth expansion techniques, including the technique advantages and disadvantages; finally Section 2.4 described signal collection and RF-DNA processes used for device classification. Chapter III investigates simulation and hardware tests adapting the techniques described here to solve the bandwidth expansion problem.

### III. Methodology

The overarching goal of the research effort is to perform a wide-band signal recovery. The recovery involves collecting a wide-band uniform white noise signal that exceeds the bandwidth of a single Software Defined Radio (SDR). This requires simultaneously collecting the signal using multiple SDRs. The reconstruction process must account for frequency offset and phase errors to ensure accurate symbol recovery.

A general equation is proposed to determine the minimum number of SDRs ( $N_{SDR}$ ) required to recover the full span of a transmitted signal bandwidth. The proposed equation is,

$$N_{SDR} = \left\lceil \frac{\beta_{tx}}{\beta_{rx} - \beta_{ol}} \right\rceil, \quad 0 < \beta_{ol} < \beta_{rx}, \quad (29)$$

where  $\beta$  is the instantaneous bandwidth, subscript  $tx$  denotes the transmit signal, subscript  $rx$  denotes each SDR receiver filtered signal and subscript  $ol$  denotes the desired sub-band overlap.

To investigate the adequacy of the equation we need to confirm that the  $N_{SDR}$  required to span a transmission signal bandwidth (e.g. the Noise Radar Network (NoNET) transmission bandwidth) is consistently determined using (29). Alternatively, we may find that additional factors affecting  $N_{SDR}$  are identified requiring reconsideration of (29).

The following sections describe the research methodology. Section 3.1 describes the bandwidth expansion models; Section 3.2 details the bandwidth expansion techniques used to effect transmit signal reconstruction; Section 3.3 discusses single, dual and multiple SDR simulation and hardware tests; Section 3.4 describes the scaling of the bandwidth expansion technique; Finally, Section 3.5 details a Radio Frequency-

Distinct Native Attribute (RF-DNA) test case. A summary of the bandwidth expansion simulations are provided in Appendix 5.1.4 Table 12 and the hardware tests are provided in Appendix 5.1.4 Table 13.

### **3.1 Bandwidth Expansion Modelling**

Simulation and hardware tests allow us to assess the effects of inputs on a process or system. Simulation also permits us to alter and assess the effect of controllable and uncontrollable factors on the process or system [39]. Multiple simulation or test runs can identify dominant factors influencing the desired output. These factors can then be accepted, controlled or mitigated [39]. Before this occurs system model development is required.

A communications system signal process is provided as a simulation model. The model steps are implemented in the Matrix Laboratory (Matlab<sup>®</sup>) 2018a software. The model is discussed in Section 3.1.1. Quadrature Phase Shift Keying (QPSK) signal and uniform white noise signal model generation are discussed in Section 3.1.2. This discussion includes the use of a Linear Feed-back Shift Register (LFSR) for drawing random samples. Section 3.1.3 describes the test used to validate the model for the research effort. Finally, symbol recovery measurement is discussed in Section 3.1.4.

#### **3.1.1 The Communications System Signal Process Model**

The communications system signal process model was developed using Matlab<sup>®</sup> R2018a. Initial development was coded using scripts until a fundamental process appreciation was gained. To improve computational efficiency and increase function flexibility, subsequent code was developed using the Matlab<sup>®</sup> R2018a communications system toolbox. This sub-section presents the process model overview. Bandwidth expansion techniques, simulation and hardware test set-up and signal parameters are addressed

in later sub-sections.

To simplify modelling, the signal process model was separated into transmit and receive components. The transmit and receive process models are shown in Figures 10 and 11 respectively. The minor variations to the models arising from QPSK modulation and demodulation are discussed in Section 3.1.2.1. The signal specific variations to the models are not indicated in Figure 10 and Figure 11.

### 3.1.1.1 The Transmit Process Model

The transmit process begins with modulating uniformly distributed randomly sampled bits to form a complex symbol. The random samples are generated using the Matlab<sup>®</sup> R2018a communications system toolbox ‘comm.PNSequence’ system object. This system object simulates a LFSR. The LFSR is described in Section 3.1.2.1. A user-defined number of symbols are combined to form a complex signal channel, or multiple complex signal channels.

The complex signal channels (e.g. ‘ $Tx_A$ ’ and ‘ $Tx_B$ ’) are up-sampled and filtered using the Matlab<sup>®</sup> communications system toolbox ‘comm.RaisedCosineTransmitFilter’ system object. Up-sampling interpolates ‘zeros’ between existing samples. This increases the effective sampling frequency. Interpolation filtering, referred to as pulse shaping, is provided by a Raised Root Cosine (RRC) filter. The RRC filter provides half of a transmit-receive filter combination forming a raised cosine filter. The RRC filter minimizes Inter-Symbol Interference (ISI) [11].

The up-sampled and filtered signal channels are then frequency shifted. Filtering and signal channel frequency shifting are critical to successful bandwidth expansion and are discussed further in Section 3.2. The frequency shifted channels, when summed, form a contiguous transmit signal bandwidth. Each transmit signal channel provides an auto-correlation template to recover part of the receive bandwidth

(sub-band). Transmit signal leading and trailing edge zero-padding is applied. This separates the signal pulses as the GNU Radio Companion (GRC) repeats, or continuously loops, the transmit signal when the process flow-graph is activated.

### 3.1.1.2 The Receive Process Model

Sub-band recovery is required when a single SDR receiver bandwidth does not span the complete transmit signal bandwidth. SDR receivers (e.g.  $Rx_A$  and  $Rx_B$ ) are selected or ‘tuned’ to different center frequencies so sub-bands, cumulatively spanning the transmit bandwidth, can be recovered. This ensures that transmit bandwidth coverage is contiguous, similar to the coverage depicted in Figure 4 for a bandwidth overlap case or Figure 5 for an adjacent alignment case.

Additive White Gaussian Noise (AWGN) is assumed to be imparted to the transmit signal during propagation. The B205 SDRs receive the AWGN-affected transmit signal after a propagation delay. The propagation delay is proportional to the propagation distance between the transmitter and a receiver. The propagation delay values therefore differ for each SDR receiver, but are assumed to be fixed for a SDR as time-varying propagation delay is not expected due to the static positions of the X310 and B205 SDRs [9].

A pre-determined sub-band time period, containing a single response pulse, is isolated for signal processing. The isolated pulse undergoes sample rate conversion using an anti-alias filter and down-sampling. Anti-alias filtering is provided by the Matlab<sup>®</sup> communications system toolbox ‘comm.RaisedCosineReceiveFilter’ system object receive RRC filter. This filter forms the second half of the transmit-receive raised cosine filter combination identified in Section 3.1.1.1. Down-sampling uses a decimation process whereby samples are removed at intervals determined by the samples-per-symbol value.

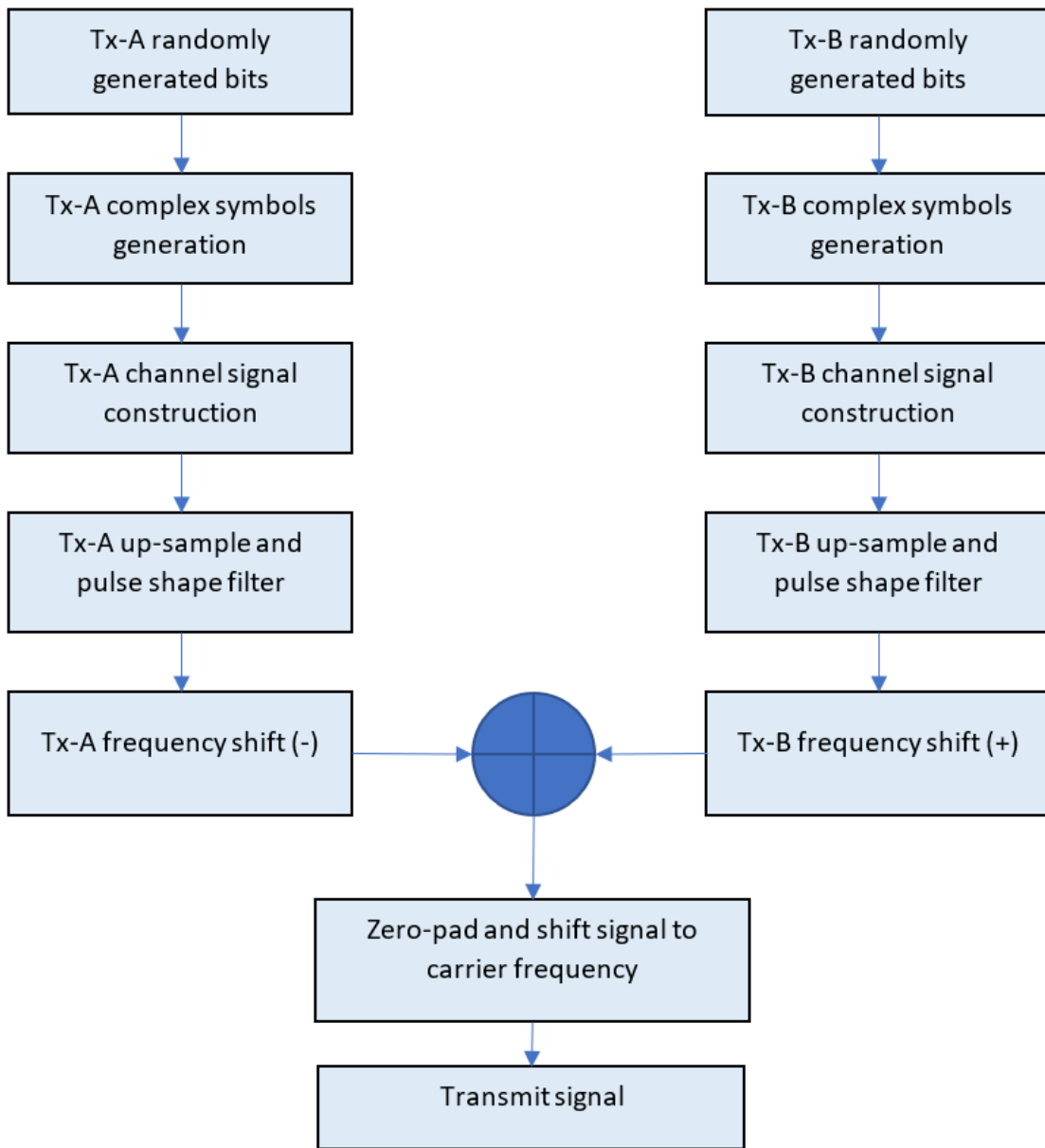


Figure 10. Communications system *transmit signal* process model [9].

Sample rate conversion is followed by receive sub-band frequency synchronization. The receive sub-band is auto-correlated with the equivalent portion of the transmitted signal (33) [30]. This is in contrast with Everett’s method [8] which achieved frequency synchronization between received sub-bands using spectral cross-correlation (16) [30]. Auto-correlation exploits a priori transmit signal knowledge. This is justified as the transmit signal channel parameters can be retained as a ‘template’ for auto-correlation. The technique is discussed in Section 3.2.

After frequency synchronization, phase synchronization is considered. To synchronize phase between a received sub-band and the transmitted signal, overlapping transmit and receive frequency bands are restored to the time domain. The lag between the restored sub-bands is applied as a delay to the transmit signal. The technique is discussed further in Section 3.2. Frequency and phase corrected signals are frequency shifted to base-band and summed to recombine the sub-bands. Finally, demodulation and symbol sequencing restore the initial transmitted symbols.

### **3.1.2 Signal Generation and Processing**

To validate the communications system process model, the QPSK and uniformly white noise signal models were generated as inputs.

#### **3.1.2.1 QPSK Signal**

The first validation simulation used an QPSK signal. QPSK is a digital communication technique that maps bits onto a quadrature constellation as complex symbols [19]. The QPSK signal is selected to validate simulation methodology because of the ease with which signal recovery can be quantified using Bit Error Rate (BER) [19].

For the transmit process, the QPSK signals are generated digitally in Matlab<sup>®</sup> R2018a.



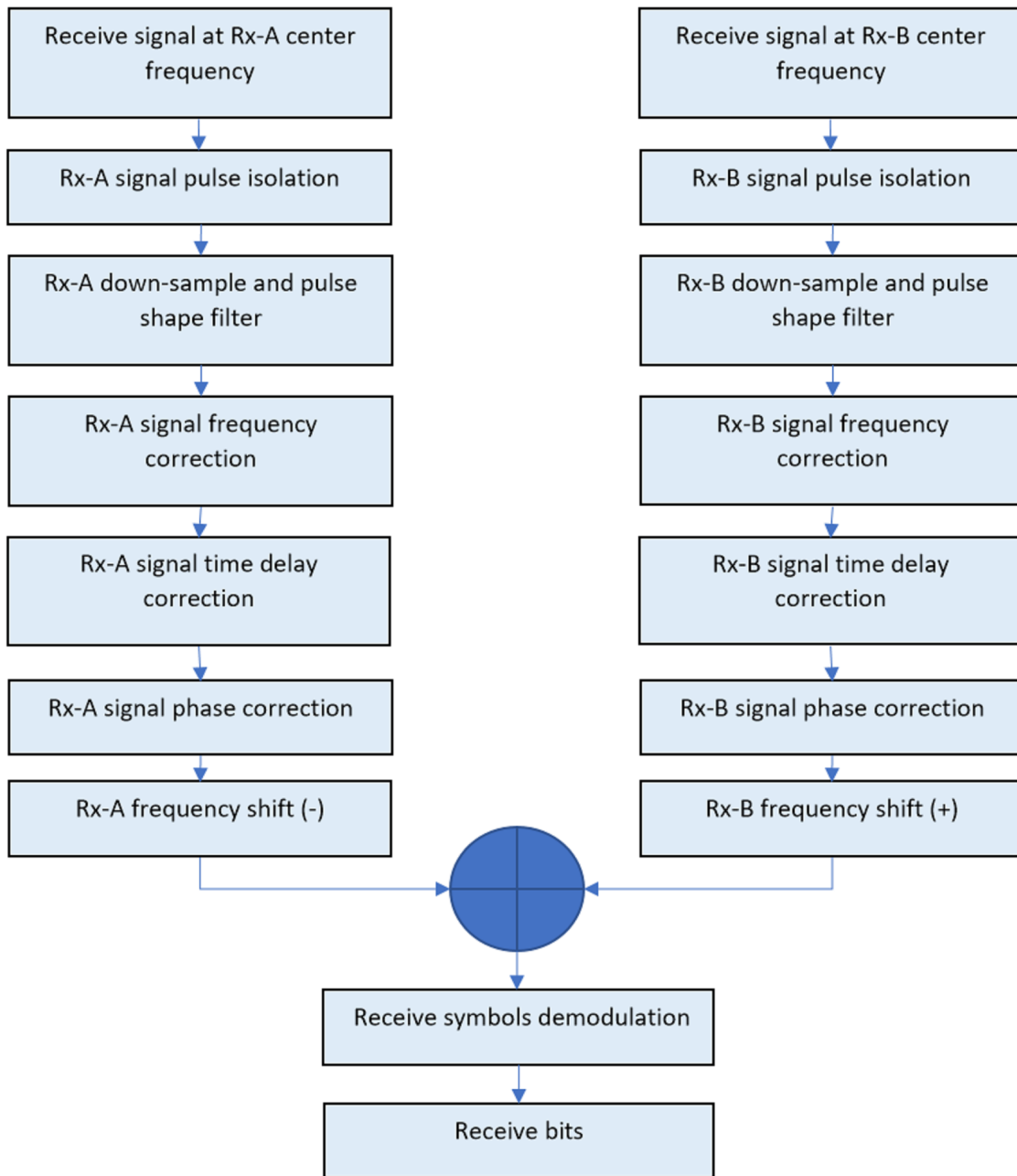


Figure 11. Communication system *receive signal* process model[9].

The QPSK parameters are detailed in Table 9. Figure 12 shows the base-band QPSK signal frequency spectrum. Samples are randomly generated from a uniform distribution using the Matlab<sup>®</sup> R2018a communications system toolbox ‘comm.PNSequence’ system object. The output bits are mapped at base-band to a complex symbol constellation using the Matlab<sup>®</sup> R2018a communications system toolbox ‘comm.PSKmodulator’ system object.

Table 9. Model validation QPSK signal parameters.

<b>Description</b>	<b>Value</b>
Sample rate	2 MS/s
Samples per symbol	4
Number of samples	20000
Number of symbols	5000
Transmit bandwidth	1 MHz
Sample duration	500 ns
Symbol duration	2 $\mu$ s
Signal duration	10 ms

The ‘comm.PNSequence’ system object outputs a LFSR generated pseudo-noise binary sequence. The LFSR bit sequence is determined by the shift-register length, tap positions and shift-register initial values known as ‘seed’ bits. The current state of the shift-register is based on exclusive-or (XOR) gate feed-back bits tapped at indicated polynomial sequence points. The XOR gate feed-back tapped bits are added ‘modulo-2’ and passed back to the input providing a new state at each clocked register shift [24].

Maximal LFSR polynomial sequences can be selected to minimize sequence repetition at user-defined shift-register lengths [24]. The LFSR taps are derived from a 36-bit feedback polynomial sequence ( $x^{36} + x^{25} + 1$ ). The pseudo-random samples generated are maximal. The selected repetition period of  $2^{36} - 1$  could be considered to provide a ‘true’ random noise output sequence for Non-Destructive Evaluation

(NDE) application purposes.

The ‘comm.PSK modulator’ system object applies a phase shift keying algorithm to map a bit, or group of bits, to a constellation symbol position. The number of constellation positions are determined by the modulation order. The modulation order is four in the case of QPSK [19].

Standard QPSK incurs an increased bit error rate due to rapid phase transition between constellation quadrants. An alternate Offset-Quadrature Phase Shift Keying (OQPSK) constellation can be used to reduce the maximum phase transition from  $\pi$  radians to  $\frac{\pi}{2}$  radians [19]. However, the standard QPSK model is used here. Figure 13 shows the transmit simulation QPSK symbol constellation for 5000 symbols. An QPSK symbol constellation, with infinite Signal-to-Noise Ratio (SNR) conditions would have infinite symbols ‘stacked’ on the unit circle at  $\frac{\pi}{4}$ ,  $\frac{3\pi}{4}$ ,  $\frac{5\pi}{4}$  and  $\frac{7\pi}{4}$  [19].

For receive signal processing, in addition to the steps seen in Section 3.1.1.2, the QPSK signal must undergo a phase ambiguity correction before demodulation occurs. The ambiguity, imparted during receiver carrier regeneration, occurs because the carrier can sometimes invert [24]. In the case of a QPSK signal, the carrier phase can align with an incorrect symbol quadrant phase. This can result in symbol error.

The transmit state aligns the carrier with a specific phase quadrant. This quadrant may be referred to as the first constellation quadrant. The phase ambiguity correction uses an indexed loop. Each loop iterates the following:

- Applies an indexed phase-shift to the received complex symbols.
- Isolates the real and imaginary symbol components.
- Restores the uncorrected isolated symbols to the first constellation quadrant.
- Determines the variance of the restored symbols.

The variance from each iteration is stored in a vector. The global minimum of the vector is applied as an index to phase-shift the received symbols. This provides the phase corrected symbols for the first constellation quadrant. Subsequent quadrant positions are found using indexed increments of  $\frac{\pi}{2}$ ,  $\pi$  and  $\frac{3\pi}{2}$  radians to rebuild the symbol constellation.

The Matlab<sup>®</sup> R2018a communications system toolbox ‘comm.PSKDemodulator’ system object is used for symbol demodulation, reversing the ‘comm.PSKmodulator’ system object process. Figure 14 shows a receive simulation QPSK symbol constellation for 5000 symbols. The receive symbol constellation shows evidence of spreading due to AWGN.

### 3.1.2.2 Uniform White Noise Signal

The second validation simulation substitutes the QPSK signal for a uniform white noise signal. Uniform white noise is a non-intrusive interrogation signal due to its low average power [34]. This is a key criteria for concurrent frequency spectrum use. This is the reason that a uniform white noise signal is selected for this research effort. The uniform white noise signal is generated digitally in Matlab<sup>®</sup> R2018a using the parameters detailed in Table 10. Figure 15 shows the base-band uniform white noise signal frequency spectrum.

Table 10. Model validation uniform white noise signal parameters.

<b>Description</b>	<b>Value</b>
Sample rate	2 MS/s
Samples per symbol	100
Number of symbols	256
Transmit bandwidth	2 MHz
Sample duration	500 <i>ns</i>
Symbol duration	50 $\mu$ s
Signal duration	12.8 ms

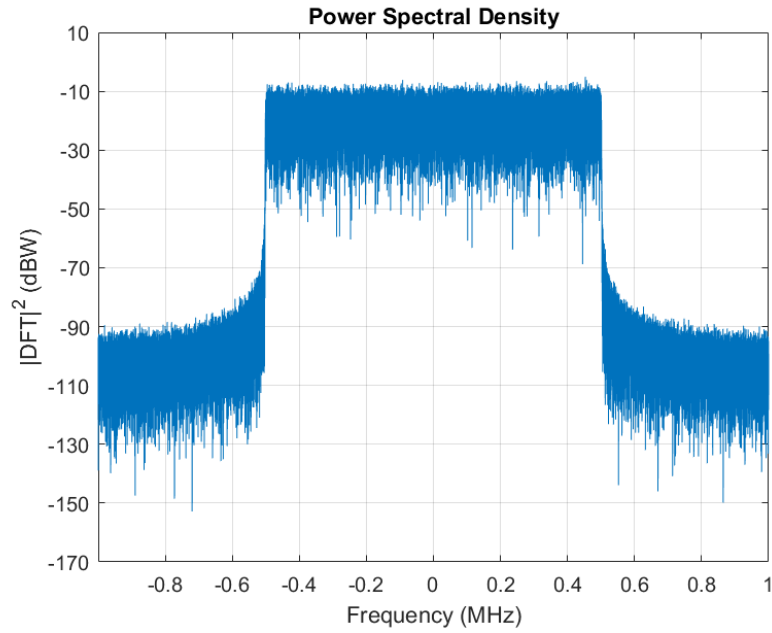


Figure 12. Power Spectral Density (PSD) showing the base-band bandwidth of a QPSK transmit signal.

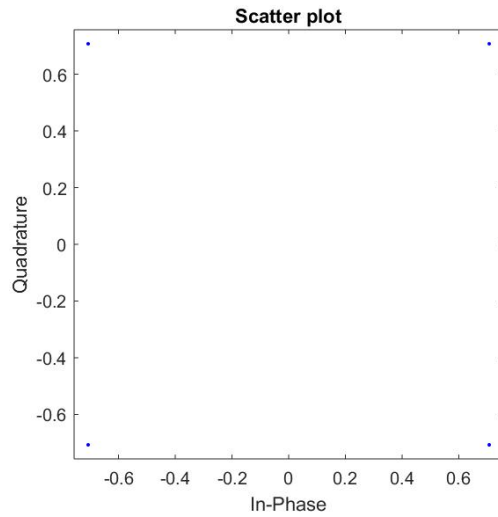


Figure 13. Simulated QPSK transmit signal constellation showing 5000 symbols, (1250 per phase) 'stacked' at  $\frac{\pi}{4}$ ,  $\frac{3\pi}{4}$ ,  $\frac{5\pi}{4}$  and  $\frac{7\pi}{4}$  under infinite SNR conditions.

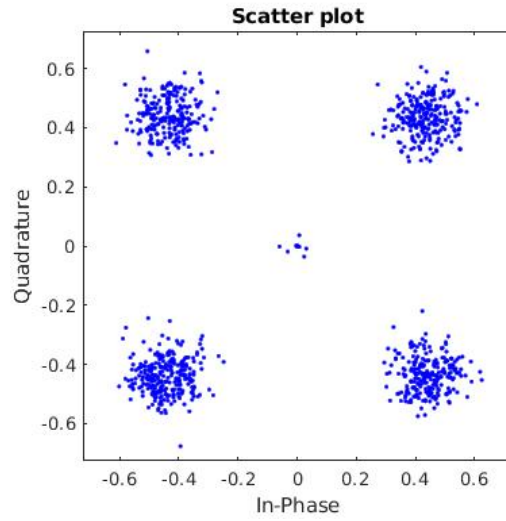


Figure 14. Simulated QPSK received signal constellation, for a single pulse containing 5000 symbols, after phase compensation. AWGN effects are evident but as the majority of symbols are restored to a quadrant, and assuming phase ambiguity is resolved, QPSK demodulation can commence.

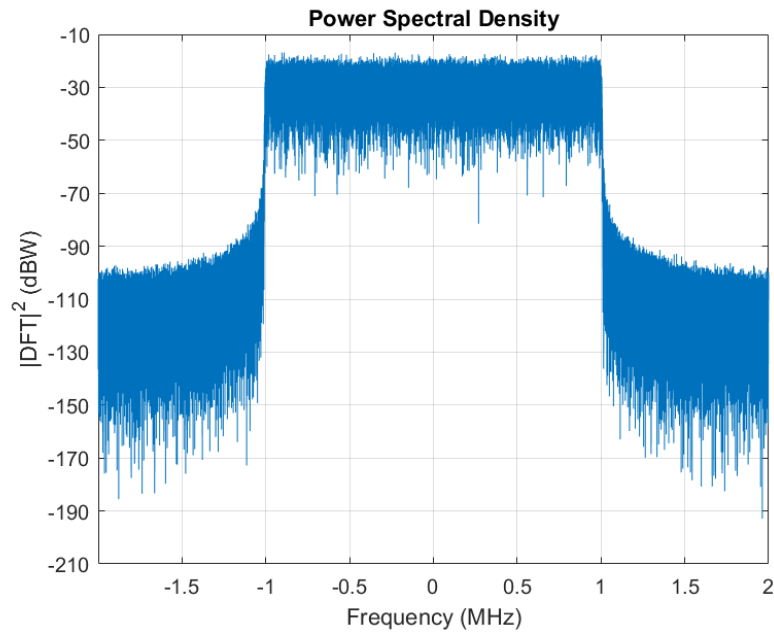


Figure 15. PSD showing the base-band bandwidth uniform white noise transmit signal.

The uniformly distributed white noise samples are generated using the Matlab<sup>®</sup> R2018a communications system toolbox ‘comm.PNSequence’ system object. The output is mapped to a  $P \times Q$  symbol table, where  $P$  is the user-defined number of complex symbols and  $Q$  is the user-defined symbol length. Complex symbols are randomly drawn from the symbol table, without repetition, to form the uniform white noise signal. Drawing a complex symbol, without repetition, from the symbol table ensures the random characteristic of the signal. The number of complex symbols  $R$  that define the signal is user-defined. Initial values of  $P$ ,  $Q$  and  $R$  were set at 256 complex symbol possibilities, a symbol length of 100, and 256 symbols per signal respectively.

### 3.1.2.3 Transmit Signal Spike Elimination

Everett identified a future work requirement to eliminate the transmit signal ‘spike’ attributed to clock bleed-through from the B205 SDR REF port to the TX/RX port [8]. The spike is evident in frequency response figures presented in [8]. The transmit spike is not evident in QPSK or uniform white noise hardware test cases for this research effort. A spike was readily produced by introducing a DC bias into signal generation code. The DC bias was introduced by the Matlab<sup>®</sup> ‘rand’ function during symbol table generation. The ‘rand’ function produces values between 0 and 1. Both real and imaginary values generated by the ‘rand’ function were offset by  $-0.5$  to remove DC bias. The resultant complex values have an expected mean of  $0 + 0i$ .

Everett’s coding specific to the signal generation cases could not be located so the clock bleed-through hypothesis was not eliminated as a causal factor. However, if PSD plots present with the transmit spike, the possibility that the ‘rand’ function use has introduced a DC bias should be considered before reverting to the clock bleed-through hypothesis. Alternatively, the Matlab<sup>®</sup> R2018a communications system toolbox ‘comm.PNSequence’ system object and the Matlab<sup>®</sup> R2018a communi-

cations system toolbox ‘comm.PSKModulator’ system object.comm remove DC bias automatically. Further, the SDR REF port should be terminated with an appropriate load. The load impedance is typically detailed in the online user manual [40].

### 3.1.3 Signal Process Model Validation

For signal process model validation, a QPSK simulation and a uniform white noise simulation were devised. The aim was to ensure communication system signal process model inputs provided expected outputs when subjected to increasing AWGN. The QPSK simulation and uniform white noise simulation both input a 500 kHz bandwidth signal to the communications system signal process model.

A frequency shift of 260 kHz was applied to the QPSK signals, one positive 260 kHz shift and one negative 260 kHz shift to the respective channels using the Matlab<sup>®</sup> R2018a communications system toolbox ‘comm.PhaseFrequencyOffset’ system object. The same frequency shifts were applied to the uniform white noise signal simulation. The frequency shifts intentionally separate the two channel signal frequency spectra to avoid symbol interference. This ensures unique bit sequence demodulation. Typically, the aim of frequency shifting for bandwidth expansion is to align adjacent sub-bands, or even provide an overlap.

The received symbols were sequenced by auto-correlating a stored replica of the transmit symbols with the complex conjugate of the received symbols. This is simply an adaption of the auto-correlation process to be discussed in Section 3.2. The sequenced symbols were then analyzed to provide Symbol Error Rate (SER). Section 4.2 provides the validation results.



### 3.1.4 Symbol Recovery Measurement

To provide process model output analysis, the probability of error for a given noise degradation needs to be measured. The probability of error is then compared with theoretical or simulated values. This identifies the penalty incurred by the bandwidth expansion process in terms of the increased signal power required, or as will be seen, the increased symbol power required.

For analog measurements, we are familiar with the probability of error versus SNR. However, SNR is applicable for power signals. Digital signals are energy signals, with probability of error typically presented as BER and SNR presented as Energy per Bit to Noise Power Spectral Density ( $E_b/N_0$ ) [24]. For a complex input signal the relationship between  $E_b/N_0$  and SNR is,

$$\frac{E_b}{N_0} = \frac{S}{N} \left( \frac{W}{R} \right), \quad (30)$$

where  $E_b$  is the bit energy,  $N_0$  is the noise power spectral density,  $\frac{S}{N}$  is the SNR,  $W$  is the bandwidth and  $R$  is the bit rate [24].

Information bits form the basis of digital messages.  $E_b/N_0$  allows the comparison of one communication system with another at the information bit level [24]. Hence, for a digital communication system  $E_b/N_0$  is a reasonable figure of merit.

This research effort is concerned with detection of the transmitted signal. As the signal is digital, bit error could be selected as an analysis metric. However, dependent on the number of information bits to each symbol, a bit error rate could be misleading. As a simplified example, if a number of bits are in error in one symbol, the symbol is in error. Alternately, if the same number of bits are in error, but those bits are spread across multiple symbols, then each of those symbols are in error. This leads to a difference in detection accuracy. Consequently, the probability of symbol error

is proposed as the preferred metric.

The probability of symbol error plots measure the SER versus Energy per Symbol to Noise Power Spectral Density ( $E_s/N_0$ ). The relationship between  $E_s$  and  $E_b$  is,

$$E_s = E_b(\log_2 M), \quad (31)$$

where  $E_s$  is the symbol energy and  $M$  is the symbol set size [24]. Presenting  $E_s/N_0$  in decibels, the relationship between  $E_s/N_0$  and  $E_b/N_0$  is as follows,

$$E_s/N_0(dB) = E_b/N_0(dB) + 10\log_{10}(k), \quad (32)$$

where  $k$  is the number of information bits per symbol. The symbol set size can be determined using  $k$ ; i.e.  $M = 2^k$  [24]. Therefore,  $E_s/N_0$  adapts the SNR figure of merit to provide a metric for our system analysis [24].

### 3.2 Bandwidth Expansion Techniques

The bandwidth expansion techniques used for this research effort rely on auto-correlation. Auto-correlation is the correlation of a signal with itself, or more precisely a delayed version of itself [30]. As we have a priori knowledge of the transmit signal, auto-correlation can be used to recover the delayed version of the transmitted signal. The auto-correlation function  $R_{xx}$  is,

$$R_{xx}[m] = \sum_{-\infty}^{\infty} \{x[n] x^*[n+m]\}, \quad -\infty < m < \infty, \quad (33)$$

where  $x[n]$  is a stored replica of the transmit signal,  $x^*[n+m]$  is the complex conjugate of the transmit signal at a delay, or lag index  $[m]$ , and  $*$  denotes the complex conjugate [30].

The auto-correlation lag index  $[m]$  can be exploited using the Fourier time-shift property (34). The Fourier time-shift property is,

$$x[n - m] \iff X[k]e^{-j\frac{2\pi k[n-m]}{N}}, \quad (34)$$

where the complex operator  $j = \sqrt{-1}$  and  $k$  is the frequency index having period  $N$  [30]. The lag index  $m$  is substituted in (34) to time-align the receive signal sub-band with the equivalent portion of the transmit signal.

This is a common use for the Fourier time-shift property, and is used in this research effort to time-align receive sub-bands with the equivalent portion of the transmitted signal. This essentially identifies the receive signal sub-band start times. The start time and a priori knowledge of the transmit signal length allows the receive signal stop time to be determined. A more novel use was the application of auto-correlation to a frequency ‘pull-in’ technique that aligns the transmit signal and the receive signal sub-band frequency.

### 3.2.1 Auto-correlation - Frequency ‘Pull-In’

In Section 2.3.3.2 it was identified that the uniform white noise signal could not exploit the non-data aided feed-forward carrier frequency offset estimation technique. Therefore an auto-correlation technique using the transmit channel templates was proposed. There is a duality to the time-shift property. This is the frequency-shift property, which can be applied in the time domain to effect a frequency shift [30]. The Fourier frequency-shift property is,

$$x[n]e^{j\frac{2\pi[k-l]n}{N}} \iff X[k - l], \quad (35)$$

where the complex operator  $j = \sqrt{-1}$  and  $l$  is the shifted frequency index having period  $N$  [30]. The auto-correlation principles can be transferred to the frequency-shift property. The lag index here references the shifted frequency index  $[l]$ . The lag index is substituted in (35) with opposite sign to frequency shift the receive signal sub-band to align with the transmit signal.

The frequency-shift property provides the basis for the frequency ‘pull-in’ technique which adapts a Frequency Locked Loop (FLL) process found in [23]. The ‘pull-in’ technique uses three auto-correlation iterations. It was assumed that the frequency offset would be a constant value between  $-20$  kHz and  $20$  kHz for the short duration (ms) signal. Section 4.3.1 show frequency change versus signal duration results.

For the first ‘pull-in’ iteration each receiver frequency sub-band was auto-correlated with the equivalent portion of the transmit signal. The transmit signal was swept through the assumed frequency-shift range, centered on the transmit frequency in  $100$  Hz steps. The auto-correlation lag index identified the new center frequency for the second iteration.

The second iteration used the same process as the first, except the auto-correlation was effected between  $-100$  Hz and  $100$  Hz of the new center frequency in  $20$  Hz steps. The lag index identified the new center frequency for the third iteration.

The third iteration used the same process as the first and second iterations except the auto-correlation was effected between  $-20$  Hz and  $20$  Hz of the new center frequency in  $1$  Hz steps. Due to the signal duration the FLL feed-back loop was not closed [23]. Instead the third iteration lag index was applied to (35) with opposite sign as a frequency shift and the FLL process ends.

### 3.2.2 Auto-correlation - Phase Correction

Phase correction also relies on auto-correlation. The phase correction technique finds the angular difference between the inner product of two complex vectors. The technique assumes that the angular difference is restricted to values between 0 and  $2\pi$  radians. An angular difference exceeding  $2\pi$  would require the signal to be repetitive. The uniform white noise signal is not repetitive. The technique also assumes that the vectors are of equivalent length ( $M$ ). The angle ( $\theta_m$ ) is,

$$\theta_m = \angle \sum_{i=1}^M \{x_i[n] x_i^*[n+m]\}, \quad (36)$$

where  $\angle$  denotes the angle operator,  $x[n]$  is a stored replica of the transmit signal, and  $x^*[n+m]$  is the complex conjugate of the transmit signal at a delay, or lag index  $[m]$ .  $*$  denotes the complex conjugate and subscript  $i$  indexes the  $i$ th vector value [30].

The transmit signal replica  $x[n]$  and its delayed version  $x^*[n+m]$  are represented by complex vectors. The angle ( $\theta_m$ ) returns a constant in radians. To phase-align the complex vectors,  $\theta_m$  is substituted into the following equation. The phase corrected vector is given by,

$$x[n] = x[n+m] e^{j\theta_m}, \quad (37)$$

where  $\theta_m$  is substituted with opposite sign [30]. The phase correction is effected in the phasor domain. The resultant shift also time-aligns the signal in the time domain.

### 3.2.3 Transmit Signal Preparation

The QPSK and uniform white noise transmit signal channels were designed in Matlab<sup>®</sup> R2018a using a RRC pulse shaping filter. Table 11 details the RRC filter

parameters. The RRC filter design features a steep roll-off and reduced pass-band ripple. This defines the characteristic square-like filter pass-band system response. The adjacent channels can be aligned to provide a contiguous pass-band with bandwidth overlap limited to that part of the response beyond the cutoff frequency. The received sub-bands retain this characteristic simplifying signal reconstruction. Figure 16 shows the Matlab<sup>®</sup> FVtool depiction of the RRC filter frequency response. The roll-off, using inputs from Table 9 is  $-3\text{dBW}/1000\text{Hz}$ . Figure 17 shows the resultant frequency response of a pulse shaped QPSK signal transmit channel.

Table 11. RRC filter parameters for transmit signal preparation.

<b>Description</b>	<b>Value</b>
Filter type	Finite Impulse Response (FIR)
Response type	Low-pass
Sample rate	2 MS/s
Filter span	400
Filter roll-off factor	0.01
Samples-per-symbol (QPSK)	4
Samples-per-symbol (noise)	2
Dynamic range	60 dBW

The channels are then frequency shifted to create the transmit signal. The frequency shifts must be precise to ensure adjacent pass-bands are contiguous but do not overlap. Section 3.3 identifies frequency shift values for single, dual and multiple SDR simulation and hardware tests.

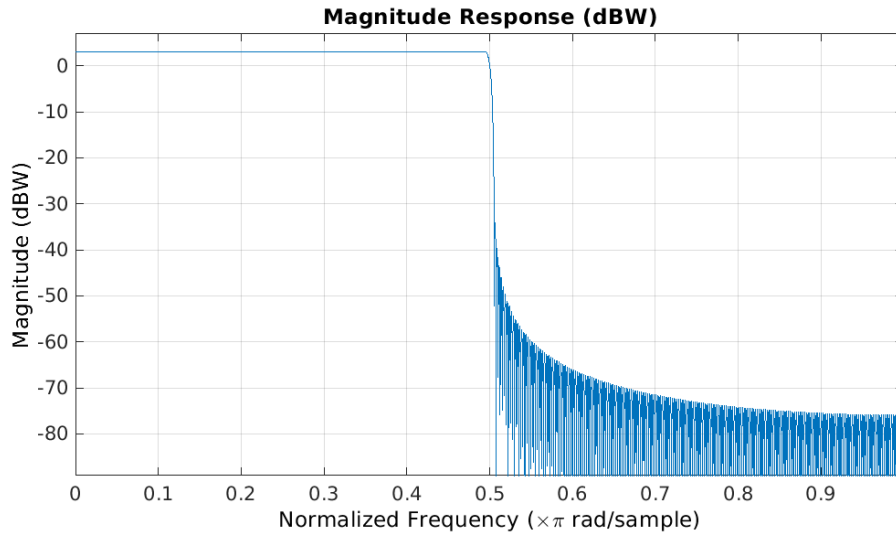


Figure 16. Matlab<sup>®</sup> FVtool filter depiction showing the steep filter roll-off used to minimize bandwidth overlap between adjacent receive signal sub-bands. Using the inputs from Table 11 the roll-off is  $-3$  dBW/1000 Hz.

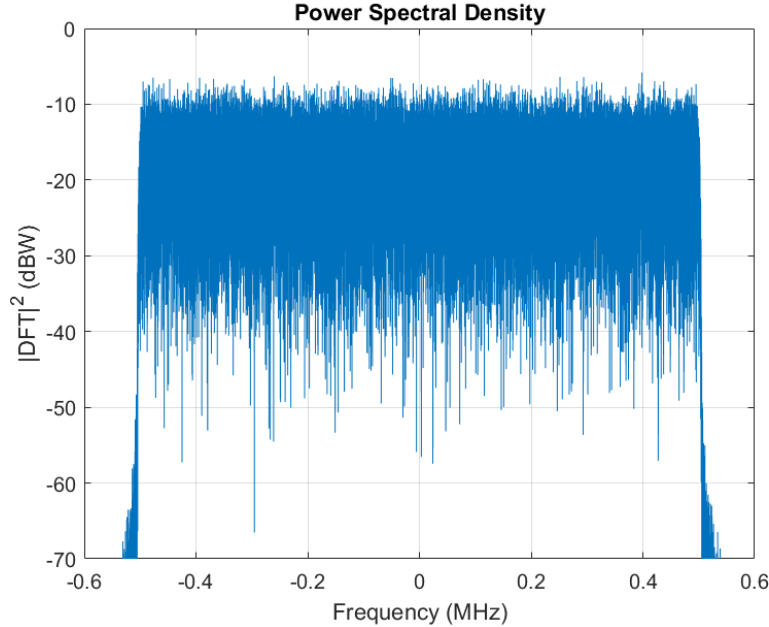


Figure 17. Filtered 1 MHz uniform white noise signal sub-band for transmit signal construction. The steep roll-off is a pre-requisite for successful bandwidth expansion using the auto-correlation technique.

### 3.3 Bandwidth Expansion Application

Attempts were made to replicate the QPSK phase cross-correlation bandwidth expansion technique in [8]. Phase cross-correlation [8], and the carrier frequency offset estimation technique [26, 27] described in Section 2.3.3 produced error values between 3% and 52%. Error values were obtained from trials, not controlled tests, but the error range suggested issues with the replication approach. Regardless, the earlier research efforts were abandoned due to the inconsistent error and the promising indications offered by an auto-correlation technique. The auto-correlation technique exploits a priori transmit signal knowledge and minimizes bandwidth overlap. The QPSK and uniform white noise signal simulations and hardware tests are devised to assess the auto-correlation bandwidth expansion techniques.

For the hardware tests, the transmit SDR is referenced to a 5 V<sub>pp</sub> 10 MHz square wave signal. This timing signal is sourced from an external Analog Waveform Generator (AWG) or the X310 on-board Global Positioning System Disciplined Oscillator (GPSDO). The GPSDO is synchronized to the GPS constellation. A 1 Pulse Per Second (PPS) clock signal is also sourced from the X310 on-board GPSDO. The on-board GPSDO is selected for both timing and clock signals as the AWG does not provide consistent results.

The GPSDO/AWG performance variation was not investigated. However, phase noise is suggested as a possible cause. This is based on the quoted Agilent 33250A AWG phase noise at 10 MHz of less than  $-65$  dBc (30 kHz band) [41] versus the board mounted OCXO GPSDO phase noise at 10 MHz of less than  $-145$  dBc (10 kHz band) adjusted to  $-105$  dBc (30 kHz band) [17].

The B205 SDR receiver clock timestamp synchronization is provided by a 1 PPS signal sourced from the X310 on-board GPSDO. The 1 PPS signal is passed via the X310 PPS/TRIG OUT output port to the B205 REF port. The B205 can also accept



the 5 Vpp 10 MHz square wave timing signal. However, the B205 REF port supports only one input, either the 10 MHz square wave or the 1 PPS signal. The 1 PPS signal is selected for sample time synchronization. Frequency synchronization is addressed using the auto-correlation technique.

Signal transfer is controlled by the GRC interface software. The txFile.bin file is passed via the host-PC 1 Gigabit Ethernet (1G ETH) port to the X310 SDR for digital-to-analog conversion before transmission at the RF front-end. The transmit X310 SDR Tx/Rx port is connected to a receive B205 SDR via the B205 Rx2 port. A 1 m Sub-Minature Version A (SMA) coaxial cable, SMA connectors and a Mini Circuits 15542 30 dB 50 ohm load attenuator for receiver protection also form part of the circuit. The input power into the B205 SDR was not quantified with the load attenuator in position.

Receiver data is returned to Matlab<sup>®</sup> as an rxFile.bin file, The rxFile.bin file is passed via a USB 3.0 cable, facilitated by the GRC interface software to the host-PC for signal processing.

Sections 3.3.1, 3.3.2 and 3.3.3 describe the respective single, dual and multiple SDR simulations. Sections 3.3.4, 3.3.5 and 3.3.6 describe the respective single, dual and multiple SDR hardware tests.

### **3.3.1 Single Receiver Dual Channel Simulations**

The single-receiver, dual-channel simulations aim to recover a 2 MHz transmit bandwidth. The use of two channels allows the summation process to be tested. All simulations and tests require summation to recombine received signal sub-bands. The exception is the single-receiver, single-channel hardware test. The partitioning of the transmit signal also provides the necessary templates to auto-correlate the equivalent portion of the received signal.

The simulation is initially conducted with zero frequency offset and phase error. As the frequency offset and phase error are not coded into the single receiver simulation, frequency and phase alignment between the recovered channels and the transmit signal is expected. Visually, auto-correlation plots are expected to identify zero lag, requiring no subsequent correction.

For the QPSK and uniform white noise signal dual channel simulations, the sample rate is set at 2 MS/s. Two simulated 1 MHz bandwidth transmit channels are generated using the transmit process model. The center frequency offsets of  $-0.5$  MHz and  $0.5$  MHz are applied. The transmit channels are summed to create a contiguous 2 MHz bandwidth signal.

The simulated 1 MHz bandwidth receive channels have center frequency offsets of  $-0.5$  MHz and  $0.5$  MHz applied respectively. The receive channels are generated to collect the adjacent 1 MHz transmit signal portions. The collected signals are passed through the receiver process model. The single-receiver, dual-channel simulation results are detailed in Section 4.2.1.

### **3.3.2 Dual Receiver Simulations**

The dual SDR receiver simulations use a similar set-up to the single SDR receiver simulations. Both the QPSK and uniform white noise signal simulations retain the 2 MS/s sample rate and the center frequencies at  $-0.5$  MHz and  $0.5$  MHz respectively. Random frequency offsets and phase error values are introduced to each signal to simulate SDR local oscillator variation. The frequency offset ( $-20$  to  $20$  kHz) and phase error ( $-\pi$  to  $\pi$  radians) values are typical of preliminary B205 SDR performance observations.

The auto-correlation ‘pull in’ technique described in Section 3.2.1 is applied to correct the simulated frequency offsets. The auto-correlation phase correction tech-

nique described in Section 3.2.2 is applied to correct the simulated phase errors. The dual receiver simulation results are detailed in Section 4.2.1.

### **3.3.3 Multiple Receiver Simulations**

To test scalability, the multiple (i.e. four) SDR receiver simulations repeat the process established for the dual SDR receiver simulations with minor changes. Again, both the QPSK and uniform white noise signals are simulated. The transmit and receive 1 MHz channel spacing is retained, with the sampling rate increased to 4 MS/s. New transmit and receive channel center frequencies are established at -1.5 MHz, -0.5 MHz, 0.5 MHz and 1.5 MHz. This provides a contiguous 4 MHz transmit bandwidth. The transmit bandwidth is collected by four simulated SDRs, each with a receive bandwidth of 1 MHz. The multiple receiver simulation results are detailed in Section 4.2.2.

### **3.3.4 Single Receiver Hardware Tests**

The single receiver hardware test methodology is discussed below. Section 3.3.4.1 considers a single channel methodology. This test is used to demonstrate the bandwidth expansion problem. Section 3.3.4.2 considers an emulated dual channel methodology. This tests the transmit and receiver signal auto-correlation techniques and bandwidth summation.

#### **3.3.4.1 Single Receiver Single Channel Tests**

A single-receiver, single-channel hardware test is devised. The aim of this test is to show that a wide-band signal can not be faithfully reconstructed from a single B205 SDR collection. The test assumes that the wide-band signal is time-variant and therefore requires simultaneous collection of the transmitted signal bandwidth.

The test also assumes that the wide-band signal bandwidth exceeds the instantaneous receiver bandwidth.

For the first part of the test a uniform white noise signal with a 50 MHz bandwidth is generated. 50 MHz is selected as the bandwidth spans the majority of the B205 SDR instantaneous bandwidth (50 MHz of 56 MHz). 50 MS/s also meets the X310 SDR sample rate master clock decimation requirements. The X310 master clock is set at 200 MS/s. 50 MS/s will provide an even integer decimation ratio of 4. The sample time is synchronized across the transmit and receive SDRs. The transmit and receive SDRs clock timestamp synchronization references the GPSDO 1 PPS timing signal. A single B205 SDR receiver, identified as ‘ $Rx_A$ ’, is prepared for the hardware test.  $Rx_A$  variables are set in the GRC for a 50 MHz bandwidth with a center frequency at 2.4 GHz. The Matlab<sup>®</sup> and GRC transmit and receive sampling rate is set at 50 MS/s. The GRC interface software frequency shifts the transmit signal from base-band to 2.4 GHz for transmission.

‘ $Rx_A$ ’ captured the 50 MHz transmit bandwidth. Full symbol recovery for the 50 MHz bandwidth signal is expected, as this falls within the instantaneous bandwidth of a B205 SDR. This will be confirmed by auto-correlating the transmitted symbols with the received symbols. The results are provided in Section 4.3.1.

For the second part of the test a second signal is transmitted. The transmit signal has a 100 MHz bandwidth. The 100 MHz bandwidth is selected because the signal spans approximately twice the instantaneous bandwidth of the B205 SDR (100 MHz versus 56 MHz). The X310 SDR sample rate master clock decimation requirements are also met. 200 MS/s will provide an even integer decimation ratio of 2. The signal is again transmitted at a 2.4 GHz center frequency and collected using ‘ $Rx_A$ ’. The Matlab<sup>®</sup> and GRC transmit sampling rates are set at 100-MS/s. Attempts to set the ‘ $Rx_A$ ’ sampling rate to 100 MS/s resulted in the GRC flow-graph process timing

out before a collection could be made. This is discussed further in the results. The receive sampling rate was therefore restored to 50 MS/s.

Full symbol recovery for the 100 MHz bandwidth signal is not expected, as this exceeds the B205 SDR instantaneous bandwidth. Symbol recovery will be confirmed by auto-correlating the transmitted symbols with the received symbols. The single SDR hardware test circuit is depicted in Figure 18. The GRC interface setup for the single SDR hardware test is shown in Figure 19. The sampling rates indicated are for the dual-channel tests. Single receiver hardware test results are detailed in Section 4.3.1.

#### **3.3.4.2 Single Receiver Dual Channel Tests**

Two single-receiver, dual-channel hardware tests were devised. The tests use a single receiver, with two emulated channels. The first test compared the bandwidth expansion QPSK signal PSD with the simulation data. The second test compared bandwidth expansion uniform white noise signal symbol recovery with a simulated single-receiver, single-channel transmit signal recovery and the preceding QPSK signal PSD.

The QPSK dual channel hardware test aims to recover a 2 MHz QPSK transmit signal using a single SDR receiver. While the B205 SDR receiver bandwidth can support a 2 MHz bandwidth on a single channel, two emulated channels, identified as ' $Rx_A$  low channel' and ' $Rx_A$  high channel', are generated to test the bandwidth expansion techniques.  $Rx_A$  low channel has a 1 MHz bandwidth with GRC center frequency at 2.3995 GHz, while  $Rx_A$  high channel has a 1 MHz bandwidth with GRC center frequency at 2.4005 GHz. The GRC transmitter sampling rate and receiver sampling rate is set at 2 MS/s. The GRC interface software frequency shifts the transmit signal from base-band to 2.4 GHz for transmission.

Receiver narrow-band sub-channel data is returned to Matlab<sup>®</sup> as rxFile(x).bin files, where ‘x’ represent the low channel or high channel. The rxFile(x).bin files are passed via a USB 3.0 cable facilitated by the GRC interface software to the host-PC for signal processing.

The dual channel hardware test subjects the transmit signal and the SDR receive signal to the transmit, environment, and receive variables that were previously controlled during simulation. Frequency offset and phase error between the two receive channel collections and the transmitted signal templates now need to be resolved using the auto-correlation techniques.

The single SDR hardware test circuit is depicted in Figure 18. The GRC interface setup for the single SDR hardware test is shown in Figure 19. Single receiver hardware test results are detailed in Section 4.3.1.

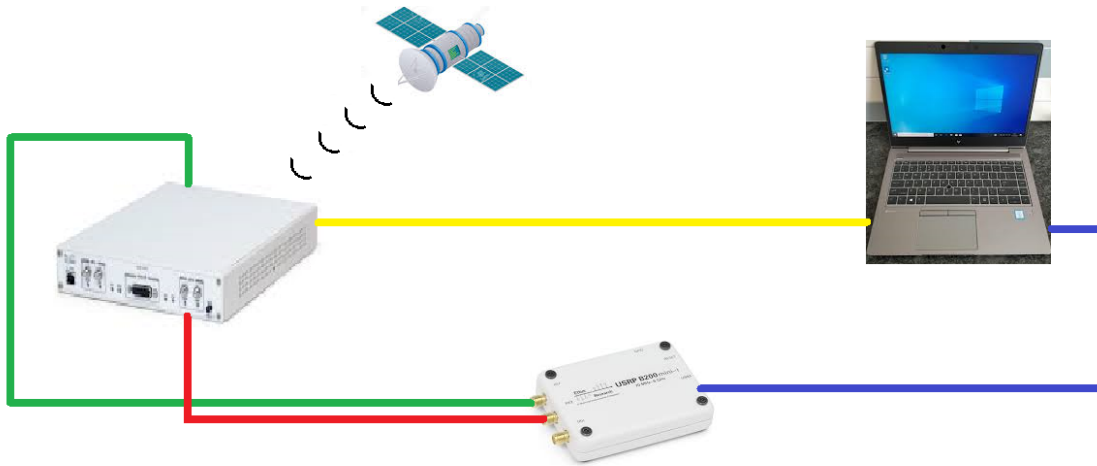


Figure 18. Hardware circuit setup for single SDR receiver tests. Connection legend: TX/RX signal (Red); 1 PPS (Green); 1G ETH (Yellow); USB 3.0 (Blue).

### 3.3.5 Dual Receiver Hardware Tests

Two dual receiver hardware tests were initially devised. The first test aimed to recover a 2 MHz QPSK transmit signal using two SDR receivers, each receiver

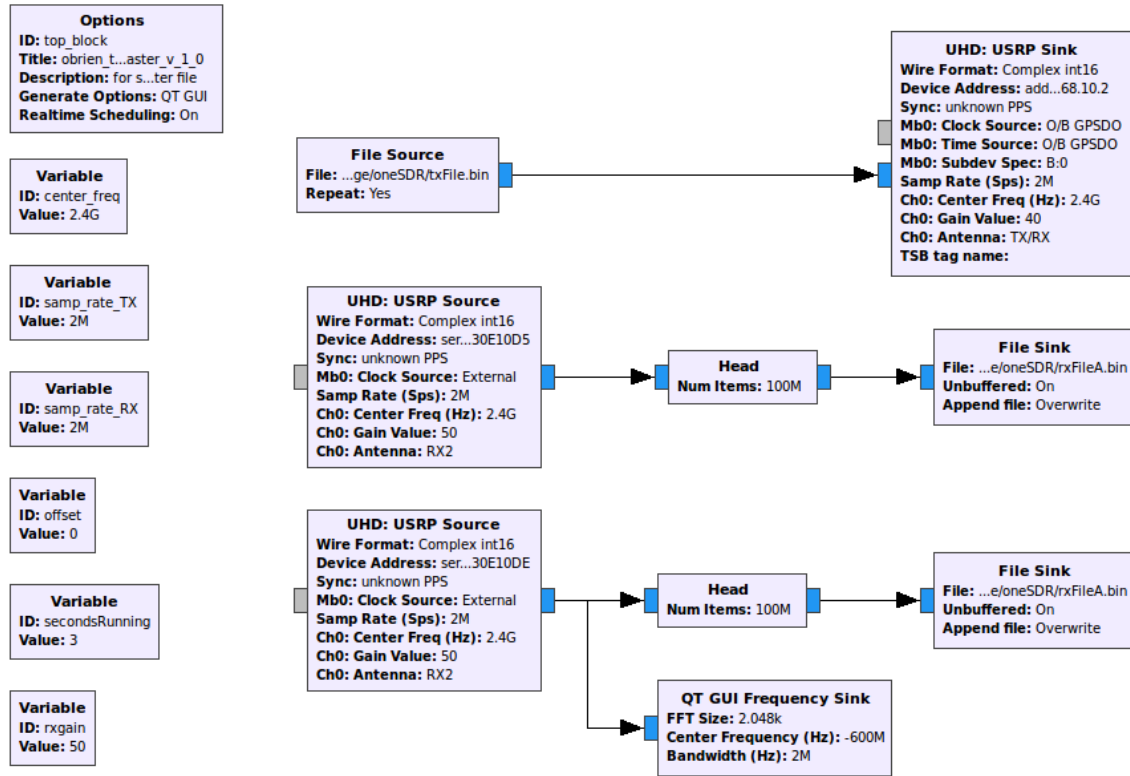


Figure 19. GNU radio companion interface setup for single SDR hardware tests.

recovering 1 MHz of the transmit signal. This test aimed to confirm the bandwidth expansion technique was viable using hardware, accounting for additional receiver frequency offset and phase errors arising from dual SDR receiver use.

The first dual receiver hardware test compared the bandwidth expansion QPSK signal PSD with simulation data. The second test substituted the uniform white noise signal for the QPSK signal. This test compared symbol recovery data with the simulated single-receiver, single-channel uniform white noise signal symbol recovery data and the QPSK signal PSD.

The sample time is synchronized across the transmit and receive SDRs. The transmit and receive SDR clock timestamp synchronization again references a 1 PPS timing signal. Two B205 SDR receivers, identified as ' $Rx_A$ ' and ' $Rx_B$ ', are prepared for hardware tests.  $Rx_A$  had a 1 MHz bandwidth with the GRC center frequency at

2.3995 GHz, while  $Rx_B$  had a 1 MHz bandwidth with the GRC center frequency at 2.4005 GHz. The Matlab<sup>®</sup> and the GRC transmitter sampling rate is set at 2 MS/s and the two receivers have sampling rates set at 1 MS/s. The GRC interface software frequency shifts the transmit signal from base-band to 2.4 GHz for transmission. The frequency shift ensures the signal is transmitted at frequencies supported by both the X310 and B205 SDRs. ‘ $Rx_A$ ’ captures the lower 1 MHz of the transmit bandwidth, while ‘ $Rx_B$ ’ captures the upper 1 MHz of the transmit bandwidth. Frequency offset settings provide a bandwidth overlap. However, the overlap only occurs where the transition region imposes on the adjacent sub-band. The frequency offset settings are assumed to provide a contiguous 2 MHz bandwidth recovery.

Transmit signal propagation was similar to the single SDR case, except for minor hardware changes. The hardware changes included a NARDA 4315 power splitter, a USB3.0 multi-port adapter and additional cabling inserted into the circuit to support the additional B205 SDR. The power splitter supported a bandwidth between 8 – 12 GHz. It is acknowledged that the transmit signal bandwidth was outside this range. The impact of the incorrect frequency use (2.4 GHz) on the power splitter signal output was not characterized. Additionally, the power loss attributable to the splitter was not accounted for in Matlab<sup>®</sup> code to remove bias from SER plots. The received signals were again passed via USB 3.0 to the host laptop Matlab<sup>®</sup> software for signal processing.

The hardware test circuit is depicted in Figure 20. The GRC interface setup for the dual SDR hardware test is shown in Figure 21. The 20 MHz and 100 MHz dual SDR receiver cases are discussed in Section 3.4. The dual receiver hardware test results are detailed in Section 4.3.2.



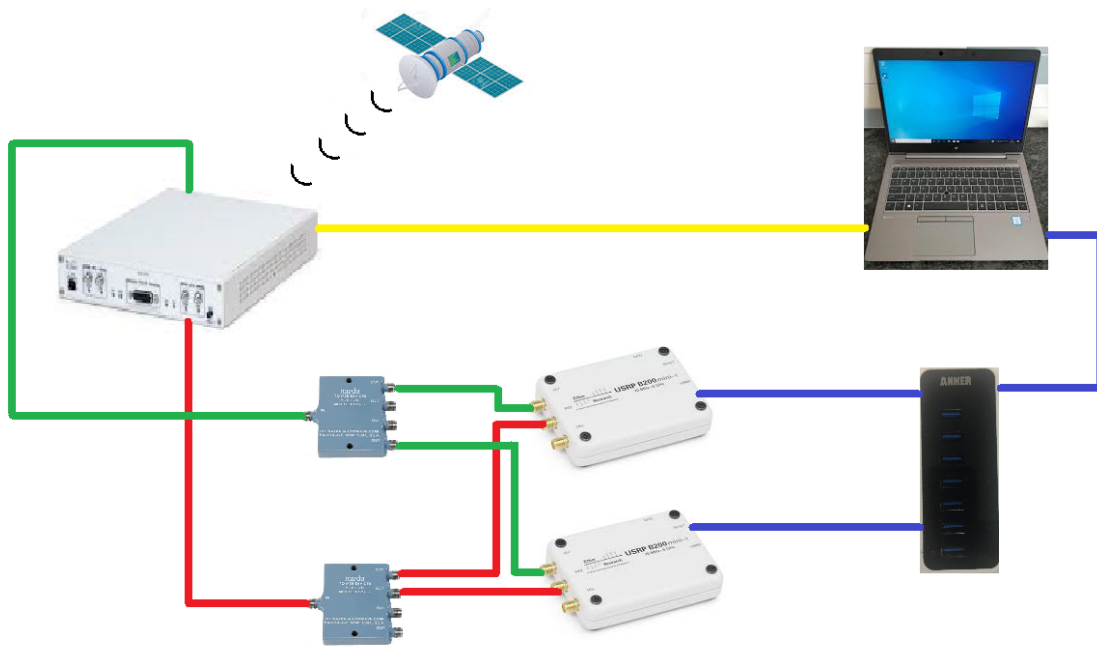


Figure 20. Hardware circuit setup for dual SDR receiver tests. Connection legend: TX/RX signal (Red); 1 PPS (Green); 1G ETH (Yellow); USB 3.0 (Blue).

### 3.3.6 Multiple Receiver Hardware Tests

Two multiple (four) receiver hardware tests were devised to confirm bandwidth expansion technique scalability. The first test aims to recover a 4 MHz QPSK transmit signal using four SDR receivers, each receiver recovering 1 MHz of the transmit signal. This test compares the bandwidth expansion QPSK signal PSD with simulation data. The second multiple receiver hardware test substitutes the uniform white noise signal for the QPSK signal. This test compares symbol recovery data with simulated single-receiver, single-channel data. The test also compares uniform white noise signal and QPSK PSDs.

The methodology is similar to the dual receiver hardware test cases, except there are now four B205 SDRs. 4 MHz QPSK and uniform white noise signals are generated for hardware tests. The respective transmit signal is again frequency shifted, using GRC functionality, to a center frequency of 2.4 GHz before being passed from the

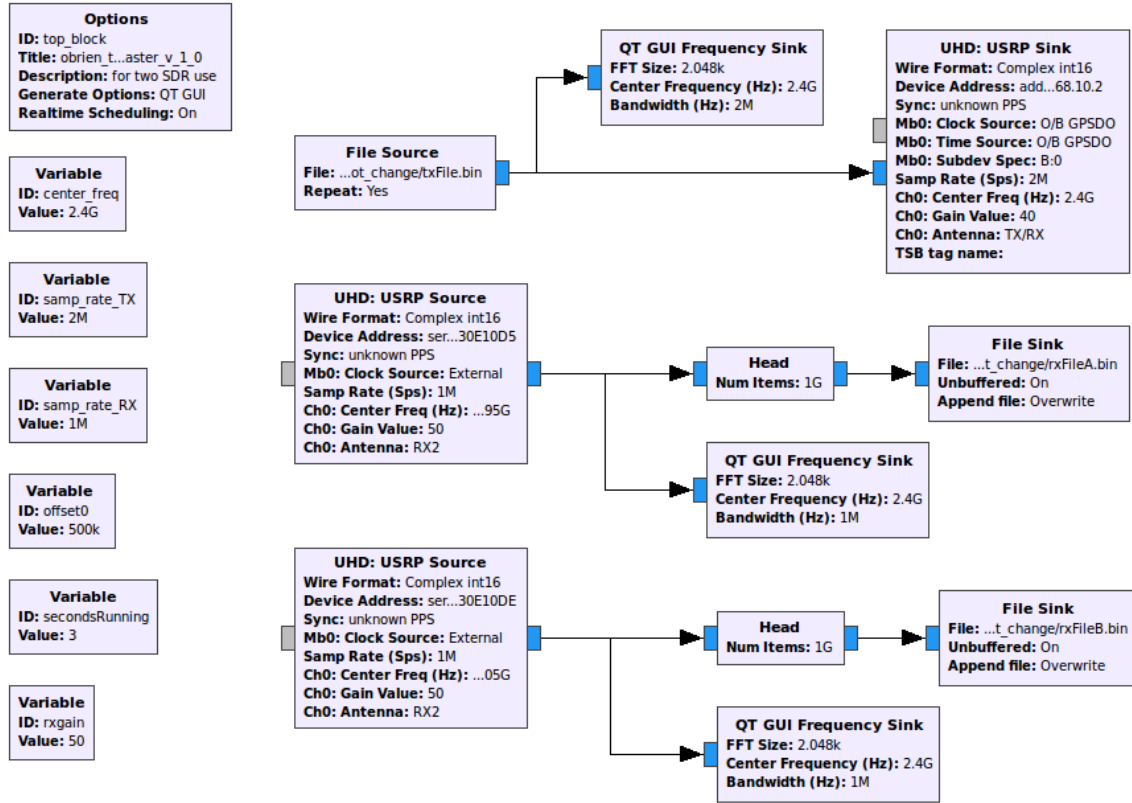


Figure 21. GNU radio companion interface setup for dual SDR receiver hardware tests.

host-PC to the X310 SDR for transmission. The B205 SDR receivers, ' $Rx_A$ ', ' $Rx_B$ ', ' $Rx_C$ ' and ' $Rx_D$ ' have center frequencies of 2.3985 GHz, 2.3995 GHz, 2.4005 GHz and 2.4015 GHz respectively. Matlab<sup>®</sup> and GRC transmitter sampling rates are set at 4 MS/s and GRC receiver sampling rates are set at 1 MS/s.

The hardware and Matlab<sup>®</sup> software changes simply scale existing B205 SDR support requirements. General connectivity, hardware application and synchronization requirements were similar to dual receiver hardware test cases. The hardware test circuit is depicted in Figure 22. The GRC interface setup for the four SDR hardware test is shown in Figure 23. The 20 MHz and 100 MHz multiple SDR receiver cases are discussed in Section 3.4. Test results are detailed in Section 4.3.3.

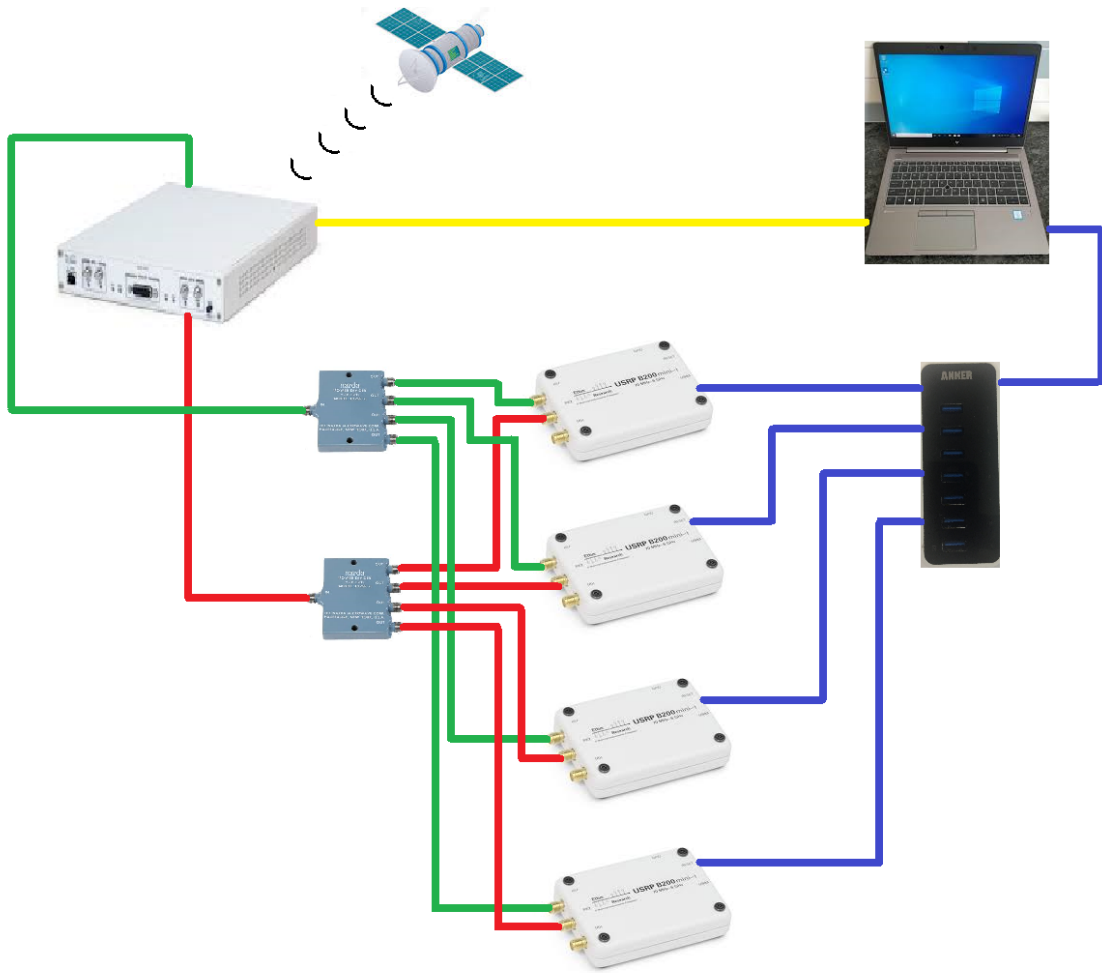


Figure 22. Hardware circuit setup for multiple SDR receiver test. Connection legend: TX/RX signal (Red); 1 PPS (Green); 1G ETH (Yellow); USB 3.0 (Blue).

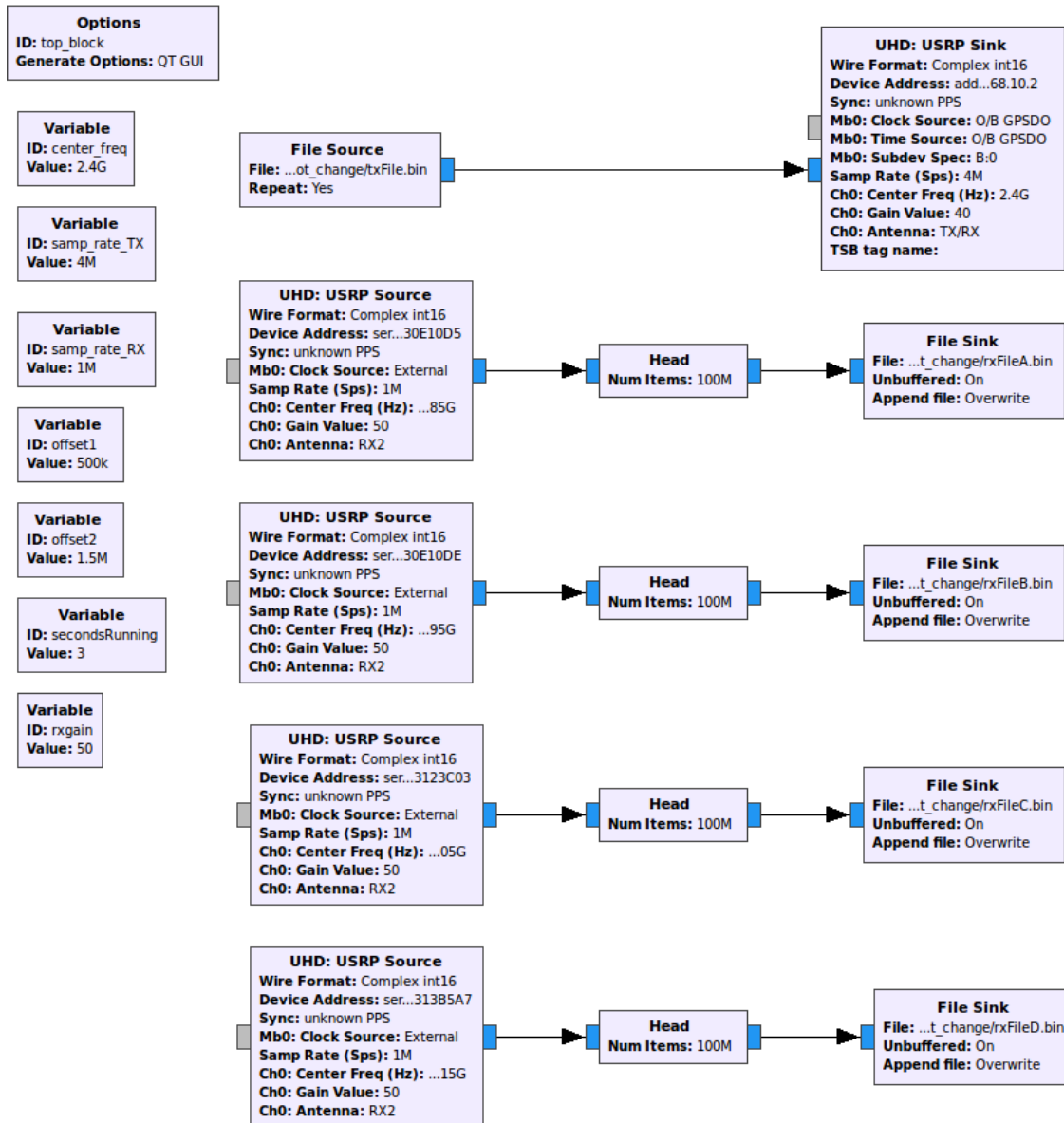


Figure 23. GNU radio companion interface setup for multiple SDR receiver hardware test.

### 3.4 Scaling the Bandwidth Expansion Technique

After the initial bandwidth expansion hardware tests the focus shifted to increasing single SDR bandwidth use. This was followed by bandwidth expansion exceeding a single SDR instantaneous bandwidth. A simple sampling rate adjustment and a center frequency recalculation are the only variable changes required to extend the recoverable bandwidth limits. The changes are applied to each sub-band.

Initially, a 50 MHz bandwidth hardware test was conducted using the dual SDR hardware test set-up in Figure 20. The test repeatedly failed to recover the correct symbol sequence. Each collection spanned a 25 MHz bandwidth. The GRC Graphic User Interface (GUI) displayed an overflow (*O*) condition which was interpreted as the host-PC losing data packets. Reducing the bandwidth to 20 MHz resolved the issue. For the 20 MHz test, each SDR collection spanned a 10 MHz bandwidth.

The reason for the unsuccessful 50 MHz test was investigated. Insufficient usable instantaneous bandwidth was identified as the cause. The usable instantaneous bandwidth is governed by:

- SDR analog bandwidth.
- Field Programmable Gate Array (FPGA) processing bandwidth.
- Host-PC hardware bandwidth limitations [42].

Therefore, with the existing configuration, a 20 MHz bandwidth is reasonably expected to be the upper-bound of bandwidth expansion. The existing configuration is comprised of an X310 SDR Universal Software Radio Peripheral (USRP) UBX-160 daughter-board, FPGA processing bandwidth (Analog to Digital Converter (ADC)/Digital to Analog Converter (DAC) (200/800 MS/s)) and a host-PC 1G ETH hardware connection. The host-PC 1G ETH stream at 25 MS/s is the limiting factor for this case [42].

The 20 MHz signal was the widest bandwidth successfully tested using the 1G ETH connection. This was due to the aforementioned 1G ETH configuration and the X310 SDR sampling rate decimation requirements. The X310 SDR sample rate decimation is required to be an even integer value of the SDR master clock (e.g. When the X310 SDR clock rate is set at 200 MS/s, a decimation rate of 10 will provide a 20 MHz bandwidth). The B205 SDR clock rate is set anywhere between 5 MS/s and 61.44 MS/s. The B205 SDR clock rate is determined automatically using a value that ensures anti-aliasing and correct sample rate decimation is effected in the B205 SDR digital signal processor [40]. A multiple SDR recovery was also conducted for the 20 MHz uniform white noise signal. Each collection spanned a 5 MHz bandwidth.

To expand the bandwidth beyond 20 MHz, a new host-PC with a 10 Gigabit Ethernet (10G ETH) connection was sourced. Recall, that the 1G ETH was the limiting factor with the preceding configuration. The substitution of the old host PC with the new host-PC, and the inclusion of 10G ETH cabling and connections, were the only changes to the hardware setup in Figures 20 and 22.

A 100 MHz bandwidth dual SDR recovery was tested. For the dual SDR recovery, the sub-band collections each spanned the majority of a B205 SDR instantaneous bandwidth (50 of 56 MHz). The X310 SDR USRP UBX-160 daughter-board is identified as the limiting factor for this hardware test. However, the daughter-board is capable of supporting a 100 MHz transmit signal. Section 4.3.2 shows the dual SDR results.

Following the dual SDR recovery, a multiple SDR recovery was conducted for the 100 MHz uniform white noise signal. Each collection spanned a 25 of 56 MHz of a B205 SDR instantaneous bandwidth . The 100 MHz transmit signal bandwidth was again selected due to X310 SDR USRP UBX-160 daughter-board filter roll-off attenuation and X310 sample rate decimation requirements (i.e. 200 MS/s decimation by

2 provides 100 MHz bandwidth). The 100 MHz bandwidth was the widest bandwidth tested. Section 4.3.3 shows the multiple SDR results.

### 3.5 RFDNA Test Case

A three-class discrimination problem is proposed. The aim is to discriminate three MiniCircuits 15542 30 dB 50  $\Omega$  load attenuators (S/Nos 31420 31647 31730) using the uniform white noise interrogation signal. Single, dual and multiple SDR collections are required. The set-up for a single SDR case is shown in Figure 18. The dual SDR case is shown in Figure 20 and the multiple SDR case is shown in Figure 22.

The RF-DNA test case was not actioned, but the details are retained to facilitate future work. The intended experiment for the single, dual and multiple SDR collection required for one of the test attenuators (Device Under Test (DUT)) to be inserted into the SDR transmit/receive loop. The attenuator is positioned after the X310 TX/RX port but before the power divider for each classification evolution. A 50 MHz bandwidth, 1000 burst uniform white noise interrogation signal stimulates the DUT, with collected data saved as a .mat Matlab<sup>®</sup> file.

The three .mat files are passed as input signal structures to Air Force Institute of Technology (AFIT) Matlab<sup>®</sup> Burst.m and InSigStruct Creator.m code for signal preparation, followed by fingerprint generation using AFIT Matlab<sup>®</sup> FingerPrint-GenV14 code to generate a Matlab<sup>®</sup> finger-print feature .mat file. Finally, device training and classification is provided by AFIT MDAML V14 code to provide 2-D training and test Fisher projection plots and confusion matrices. Classification results and analysis were to be provided in Section 4.4.

### 3.6 Summary

Chapter III described the research effort methodology. Bandwidth expansion models, including the communications system signal process model, QPSK and uniform white noise signal generation models and symbol recovery metrics were described. Bandwidth expansion auto-correlation techniques and transmit signal preparation details were provided and bandwidth expansion single, dual and multiple SDR simulations and hardware tests were outlined. Finally, an RF-DNA test case was suggested as a real-world application for the bandwidth expansion process. Chapter IV will provide results and analysis.



## IV. Results and Analysis

The following sections provide research effort results and analysis. Section 4.1 provides results and analysis for the signal process model validation. Section 4.2 provides simulation results and analysis for single, dual and multiple receiver cases. Section 4.3 provides hardware test results and analysis for single, dual and multiple Software Defined Radio (SDR) cases. Finally, Section 4.4 provides the Radio Frequency-Distinct Native Attribute (RF-DNA) test case results.

### 4.1 Validation Results

The Monte Carlo Quadrature Phase Shift Keying (QPSK) and uniform white noise signal simulations were conducted to validate the system process model. Symbol Error Rate (SER) versus  $E_s/N_0$  for 0 to 25 dB is averaged over 50 runs for each validation case. The simulations are conducted with no frequency offsets or phase errors. The simulated SER versus  $E_s/N_0$  is expected to be consistent with theoretical results.

Figures 24 and 25 show the SER versus  $E_s/N_0$  for the QPSK and the uniform white noise signal simulations respectively. An SER of  $10^{-3}$  at an  $E_s/N_0$  of 13 dB is indicated for the QPSK signal. The validation result shows a 3 dB loss for the simulated channels when measured against coherently detected QPSK theoretical values. An SER of  $10^{-3}$  at an  $E_s/N_0$  of 16 dB is indicated for the uniform white noise signal. The validation result shows a 3 dB loss for the simulated channels when measured against a theoretical coherently detected M-ary orthogonal signal.

The SER is higher than expected for the validation simulations. The characteristic SER concave plot, however, provides assurance that accurate symbol recovery is possible using the system process model, albeit with a higher  $E_s/N_0$  requirement.

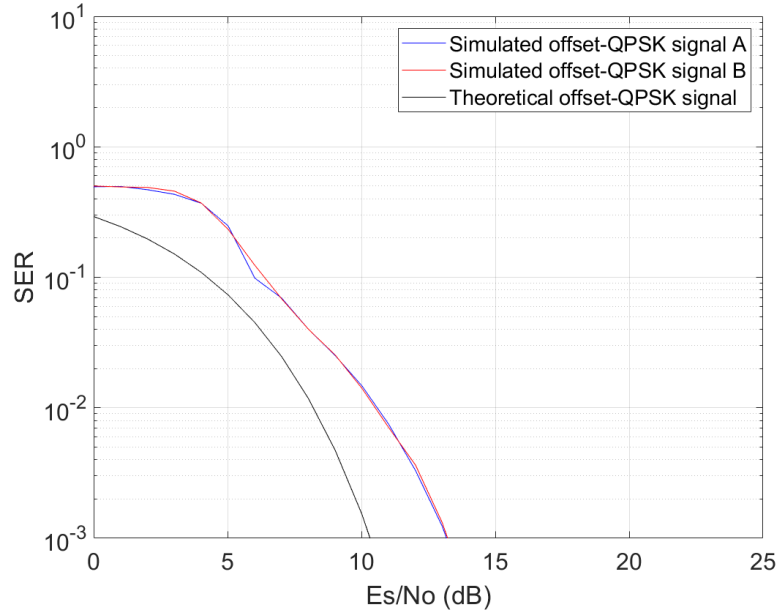


Figure 24. Monte Carlo simulation for the QPSK signal system process model validation showing SER versus  $E_s/N_0$  for the single receiver, dual channel case.

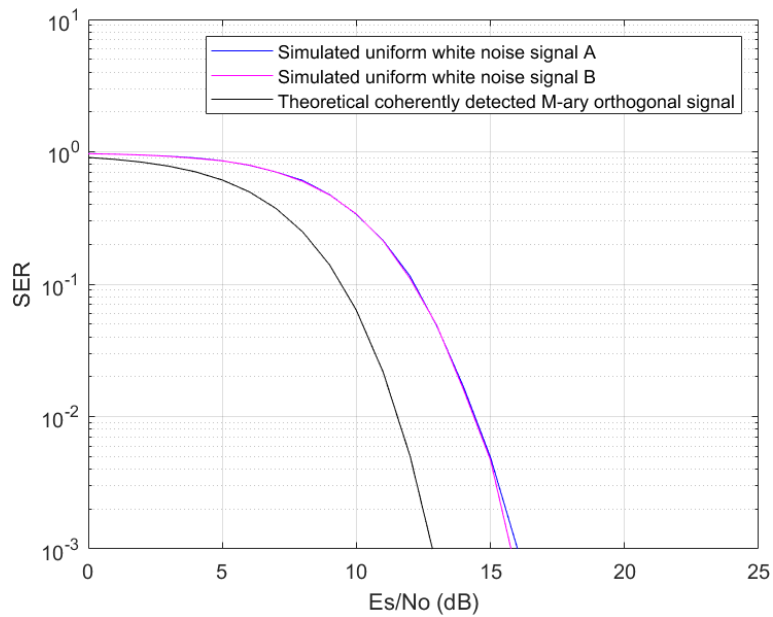


Figure 25. Monte Carlo simulation for the uniform white noise signal system process model validation showing SER versus  $E_s/N_0$  for the single receiver, dual channel case.

## 4.2 Simulation Results

This section shows results for single, dual and multiple receiver simulations. A single-receiver, single-channel simulation is mentioned in hardware testing. The simulated single-receiver, single-channel result is used as a comparative measure for symbol probability of error plots only. The single-receiver, dual-channel simulations and the dual receiver simulations show the same results. This is because the the dual receiver simulation, as described in Matrix Laboratory (Matlab<sup>®</sup>), replicates the dual channel code, simply changing ‘channel’ nomenclature for ‘receiver’ nomenclature. Therefore, the dual receiver simulation results can be considered to apply to the single-receiver, dual-channel case.

Therefore, the single receiver simulation results are not raised in this section. The dual receiver simulation results and analysis are discussed in Section 4.2.1. The multiple receiver simulation results and analysis are discussed in Section 4.2.2.

### 4.2.1 Dual Receiver Simulations

The dual SDR receiver simulations introduce frequency offset and phase error values to replicate expected local oscillator drift in the hardware tests. System resiliency to frequency and phase errors, within the prescribed bounds, meant the dual receiver simulation results showed no notable variation to the single-receiver, dual-channel results, which did not have a frequency offset or phase error applied.

Figure 26 shows the simulated 2 MHz uniform white noise transmit and receive signal auto-correlation plots, stepped through the frequency ‘pull-in’ sequence. Figure 26a shows the initial auto-correlation between the transmit and receive signal, Figure 26b shows the first iteration auto-correlation after frequency ‘pull-in’ searching for the maximum correlation index between  $-20$  kHz and  $20$  kHz, centered on the expected value in  $100$  Hz steps. Figure 26c shows the second iteration auto-correlation after

frequency ‘pull-in’ from  $-100$  Hz to  $100$  Hz centered on the first iteration maximum correlation index argument in  $20$  Hz steps. Figure 26d shows the final iteration auto-correlation after frequency ‘pull-in’ from  $-20$  Hz to  $20$  Hz centered on the second iteration maximum correlation index argument in  $1$  Hz steps. The maximum correlation index of the final iteration identifies optimal frequency synchronization between the transmit and receive signal sub-bands.

Phase correction also adopts an auto-correlation technique, using the phase angle and inner dot product for transmit and receive signal sub-band auto-correlation. The phase correction technique does not resort to the iterative approach used by the frequency pull-in technique. The phase auto-correlation plots show similar characteristics to the final frequency pull-in plots for both the uncorrelated and correlated cases. Therefore, the phase auto-correlation plots are not presented here. Further discussion regarding the frequency offset and phase error correction techniques is provided in Sections 3.2.1 and 3.2.2.

The QPSK and uniform white noise dual receiver simulation Power Spectral Density (PSD) plots show characteristic flat responses spanning the defined bandwidth. Transmit and receive PSD plots were produced for  $2$  MHz,  $20$  MHz and  $100$  MHz QPSK and uniform white noise signal bandwidths. The  $2$  MHz PSD plots for the uniform white noise signal are presented. The QPSK plots are not presented as they do not vary significantly from the uniform white noise signal plots.

Figure 27 shows the simulated  $2$  MHz uniform white noise transmit signal bandwidth for a dual SDR collection. As expected, the simulated QPSK and uniform white noise received signal PSD plots also show a characteristic flat response spanning the  $2$  MHz bandwidth. Figure 28 shows the simulated  $2$  MHz uniform white noise received signal bandwidth, with each SDR sub-band collection identified. Figure 29 shows the resultant simulated  $2$  MHz uniform white noise received signal bandwidth

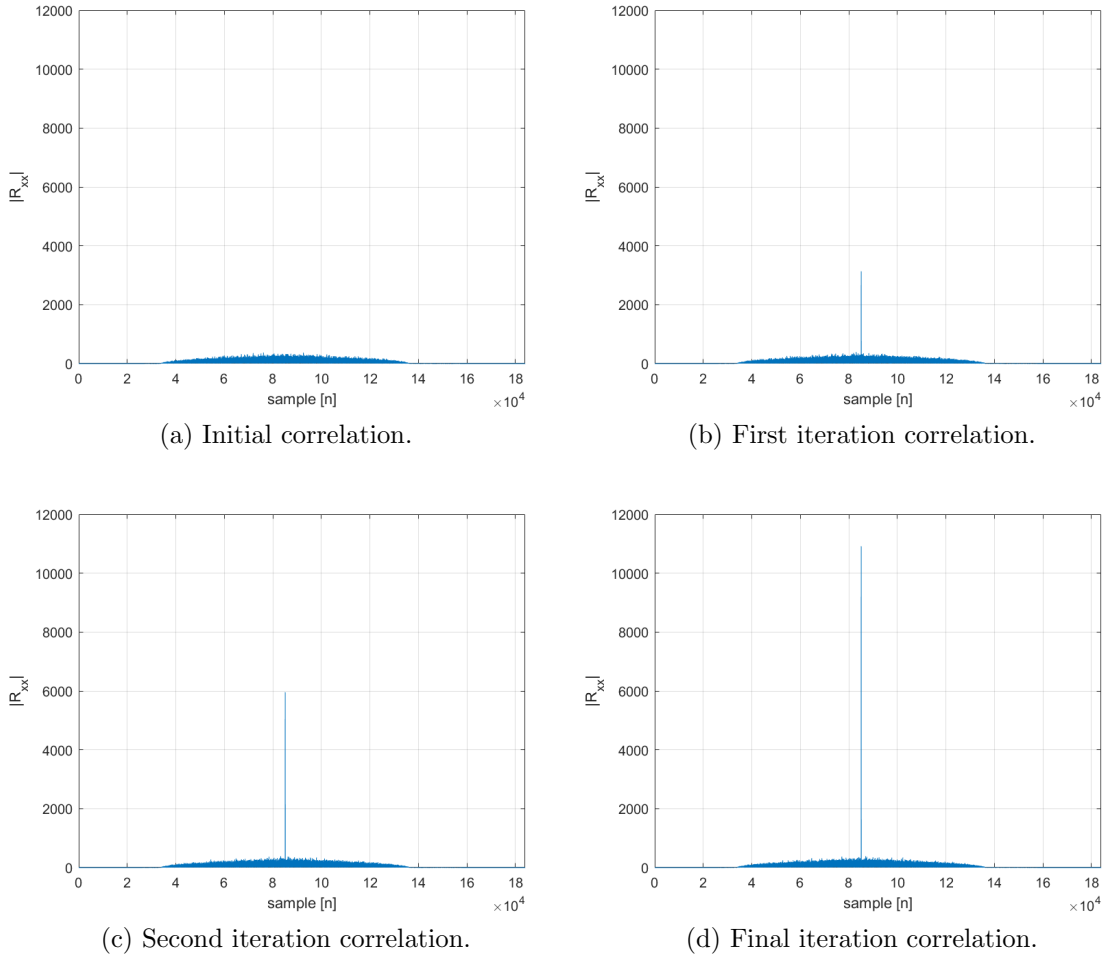


Figure 26. Simulated 2 MHz uniform white noise transmit and receive signal frequency pull in correlation sequence for a dual SDR collection.

summation.

Symbol synchronization was analyzed using two methods. The first method auto-correlated simulated transmit symbols and receive symbols to provide a coarse symbol recovery indication. The method was useful for confirming successful symbol recovery, correct sequencing and identifying synchronization lag. Symbol synchronization used Matlab<sup>®</sup> application of the Fourier time-shift property detailed in (34).

Figure 30 shows the 2 MHz uniform white noise transmit symbol and receive symbol auto-correlation for the dual SDR collection. Figure 30 shows a minor lag

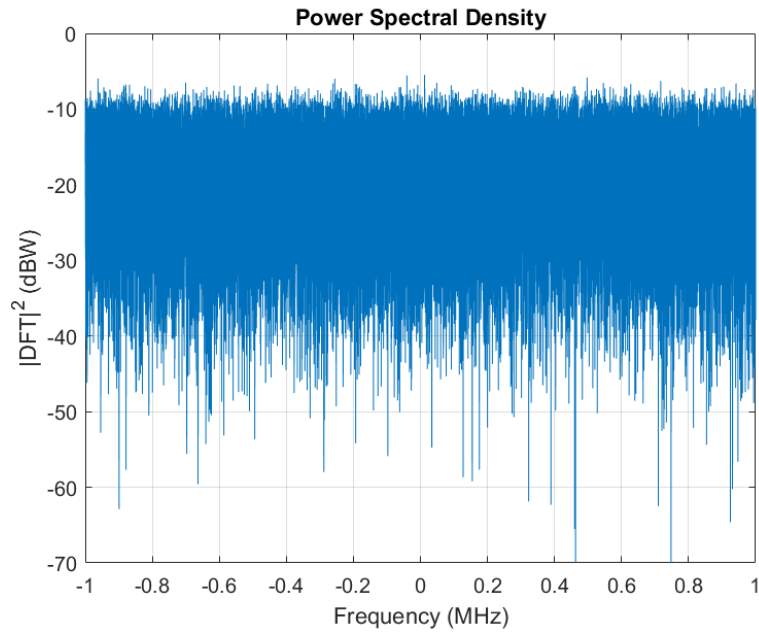


Figure 27. Simulated 2 MHz uniform white noise transmit signal PSD for dual SDR collection.

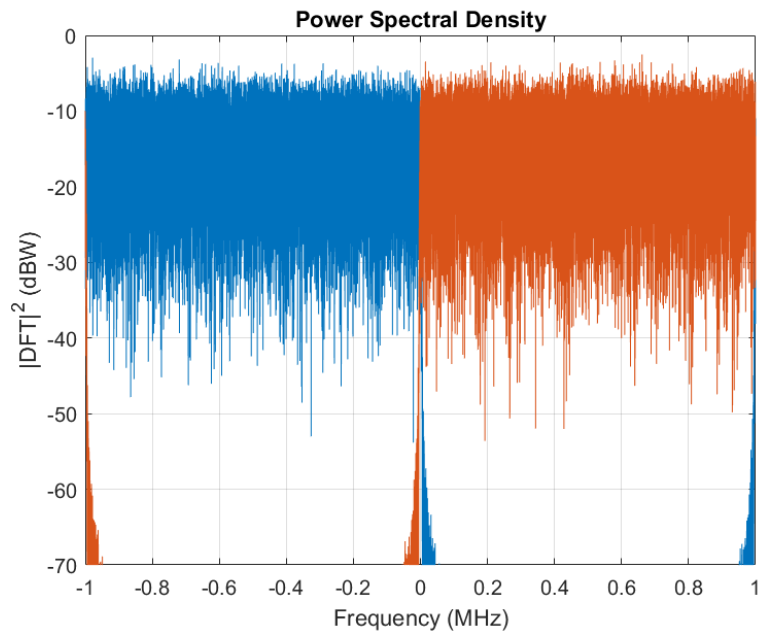


Figure 28. Simulated 2 MHz uniform white noise overlay signal PSD showing the two 1 MHz SDR collections. Each simulated SDR 1 MHz sub-band has undergone frequency and phase correction before being summed to recover the 2 MHz signal.

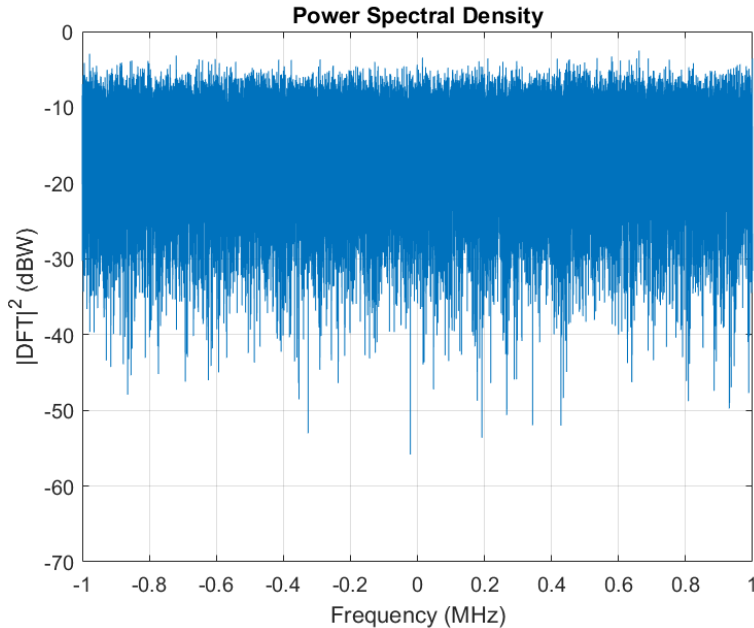


Figure 29. Simulated 2 MHz uniform white noise recombined signal PSD for a dual SDR collection. Each simulated SDR collected a 1 MHz sub-band which undergoes frequency and phase correction before the sub-bands are summed to recover the 2 MHz signal.

attributed to the system Raised Root Cosine (RRC) filter span and zero-buffer removal. Specifically, the up-sample and filter process introduced 399 complex samples to each transmit channel due to the RRC filter span (i.e. span= 400). The additional complex samples were not initially included in zero-buffer removal code calculation. The zero-buffer removal code simply removed a fraction of the received signal length. Matlab<sup>®</sup> code adjustment accounted for the lag with Figure 31 showing the corrected auto-correlation. Subsequent Matlab<sup>®</sup> code included the adjustment ensuring symbol synchronization auto-correlation did not present with this lag. The characteristic ‘spike’ is indicated in both plots indicating good symbol correlation.

The second method used symbol probability of error plots, analyzing the SER effect with increasing Additive White Gaussian Noise (AWGN). As discussed, the received symbol vector was resized to remove corrupted symbols attributable to RRC filtering. The transmit symbol vector was also resized to maintain equivalent transmit

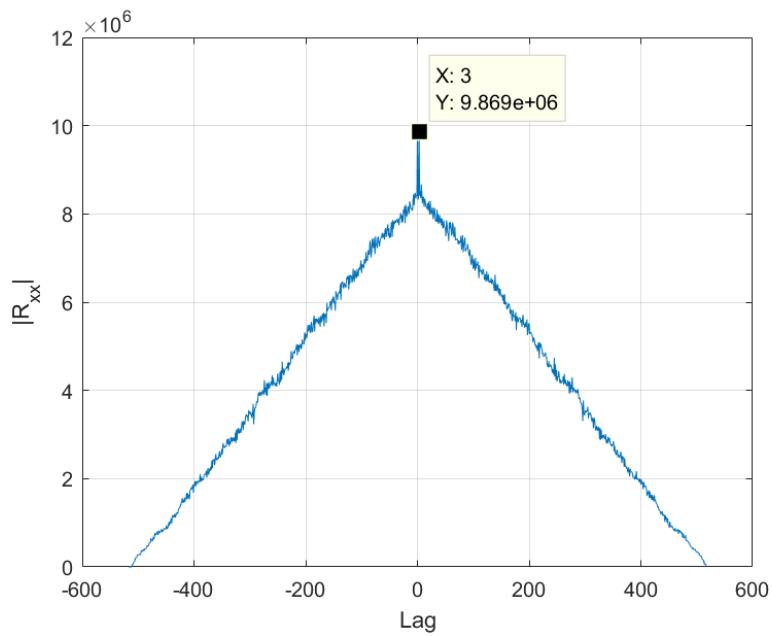


Figure 30. Simulated 2 MHz uniform white noise transmit and receive symbol correlation for a dual SDR collection. Symbol synchronization has not been effected as identified by the lag value.

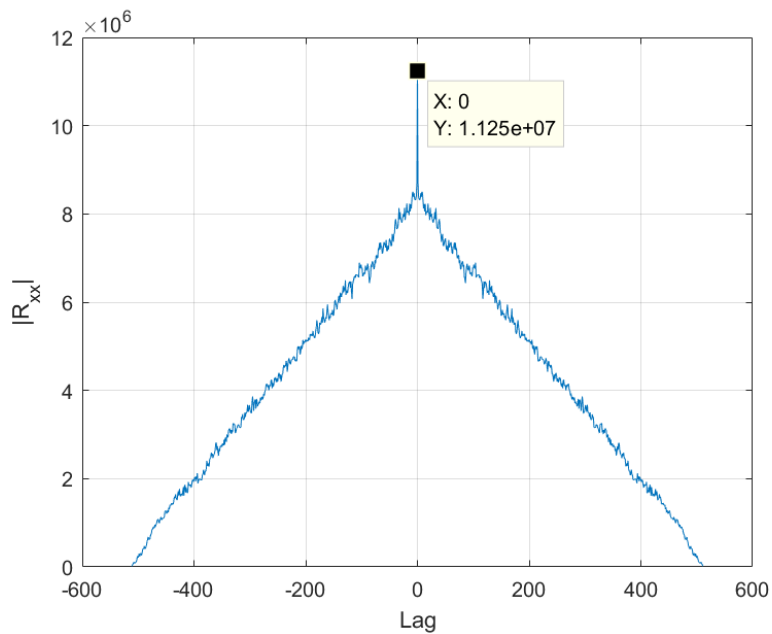


Figure 31. Simulated 2 MHz uniform white noise transmit and receive symbol correlation for a dual SDR collection. Symbol synchronization has been effected with the resultant symbol vectors now ready for probability of error evaluation.



and receive symbol vector lengths.

The Monte Carlo simulation SER versus  $E_s/N_0$  plots are provided for the 2 MHz uniform white noise signal. The Monte Carlo simulation was again conducted using 50 runs. The uniform white noise signal SER was compared with a theoretical coherently detected M-ary orthogonal signal SER. The M-ary signal is sourced for a bit value of  $k = 8$ , from [24]. The uniform white noise signal was also compared with a simulated single-SDR, single-channel 2 MHz uniform white noise signal SER. Figure 32 shows the simulated 2 MHz uniform white noise SER versus  $E_s/N_0$ , for a dual SDR collection. An SER of  $10^{-3}$  at an  $E_s/N_0$  of 16 dB is indicated. There is a 3 dB loss between the simulated dual SDR collection SER and the theoretical M-ary signal SER. A 0.5 dB loss is observed between the simulated dual SDR collection SER and the simulated single SDR collection SER.

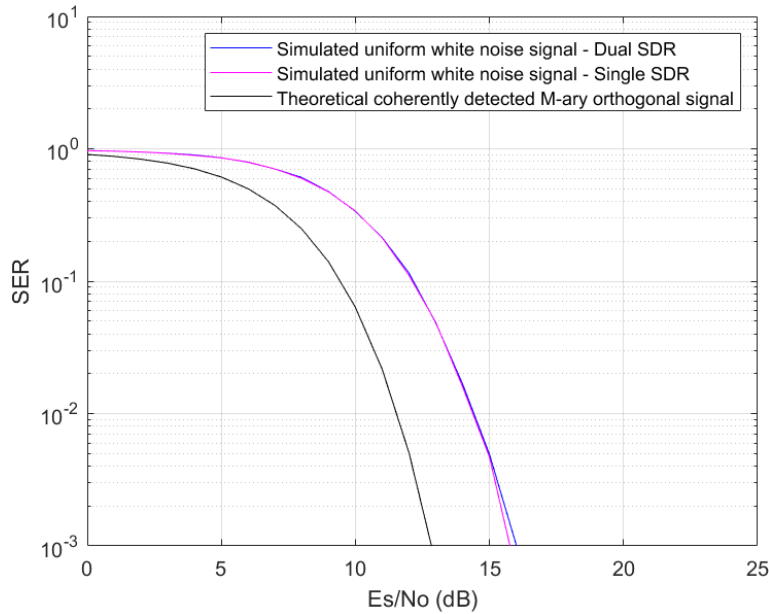


Figure 32. Monte Carlo simulation for the 2 MHz uniform white noise SER versus  $E_s/N_0$  for 0 to 25 dB, for single and dual SDR collections.

### 4.2.2 Multiple Receiver Simulations

The multiple receiver simulations use four receivers. The multiple receiver simulations simply require repetition of existing Matlab<sup>®</sup> code that was applied to the single and dual simulation cases. Three variables are changed to effect the multiple receiver simulation. The variables are sampling rate, receiver numbers and receiver center frequencies. The frequency offset and phase errors are again set within the prescribed bounds. Good auto-correlation results were again obtained once the respective correction techniques were applied. The auto-correlation plots are similar to those found in Section 4.2.1 and are not presented here.

The QPSK and uniform white noise multiple receiver simulation PSD plots show characteristic flat responses spanning the defined bandwidth. The transmit and receive PSD plots are produced for 4 MHz, 20 MHz and 100 MHz QPSK and uniform white noise signal bandwidths. The 4 MHz PSD plots for the uniform white noise signal are presented. The QPSK plots are not presented as they do not vary significantly from the uniform white noise signal plots.

Figure 33 shows the simulated 4 MHz uniform white noise transmit signal bandwidth for the multiple SDR collection. As expected, the simulated QPSK and uniform white noise received signal PSD plots also show a characteristic flat response spanning the 4 MHz bandwidth. Figure 34 shows the simulated 4 MHz uniform white noise received signal bandwidth, with each SDR sub-band collection identified. Figure 35 shows the resultant simulated 4 MHz uniform white noise received signal bandwidth summation.

Figure 36 shows good auto-correlation between the simulated 4 MHz uniform white noise transmit symbols and the received symbols. Figure 37 shows the Monte Carlo simulation 4 MHz uniform white noise SER versus  $E_s/N_0$ , for a multiple SDR collection. Again, 50 runs were conducted. An SER of  $10^{-3}$  at an  $E_s/N_0$  of 17 dB

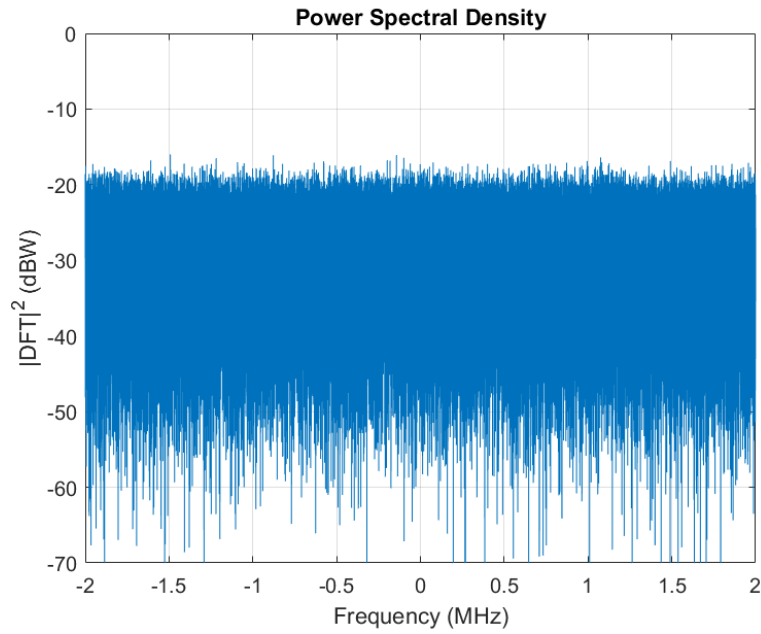


Figure 33. Simulated 4 MHz uniform white noise transmit signal PSD for multiple SDR collection.

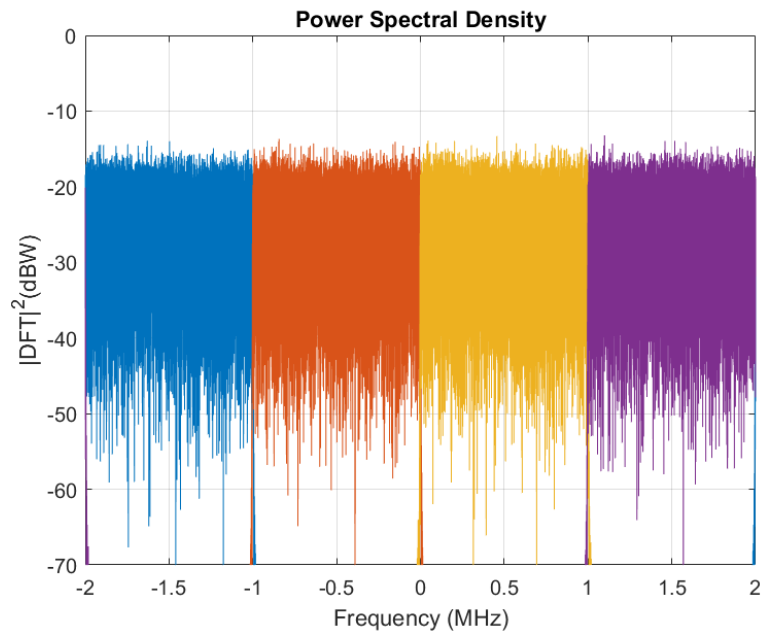


Figure 34. Simulated 4 MHz uniform white noise overlay signal PSD showing the four 1 MHz SDR collections. Each simulated SDR 1 MHz sub-band has undergone frequency and phase correction before being summed to recover the 4 MHz signal.

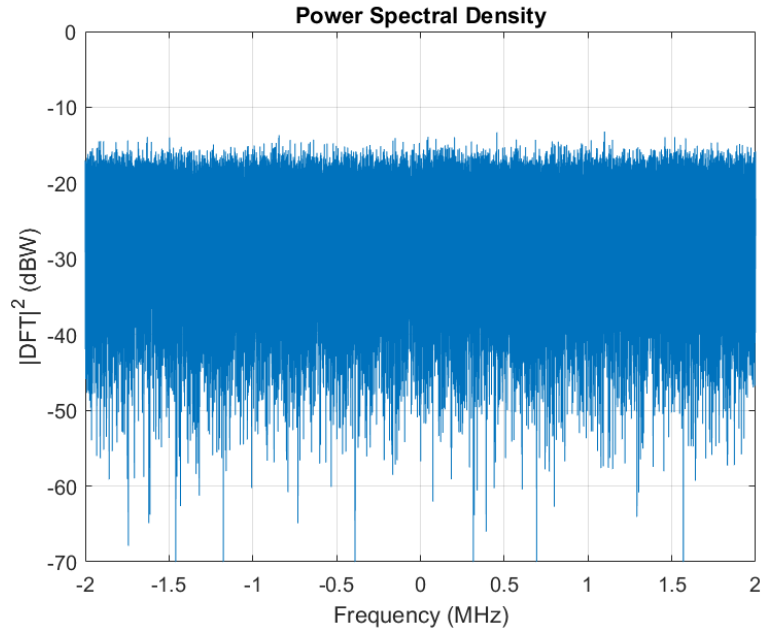


Figure 35. Simulated 4 MHz uniform white noise recombined signal PSD for a multiple (four) SDR collection. Each simulated SDR collected a 1 MHz sub-band which undergoes frequency and phase correction before the sub-bands are summed to recover the 4 MHz signal.

is indicated. There is a 4 dB loss between the multiple SDR collection SER and the theoretical M-ary signal SER, and a 1 dB loss between the simulated multiple SDR collection SER and the simulated single SDR collection SER.

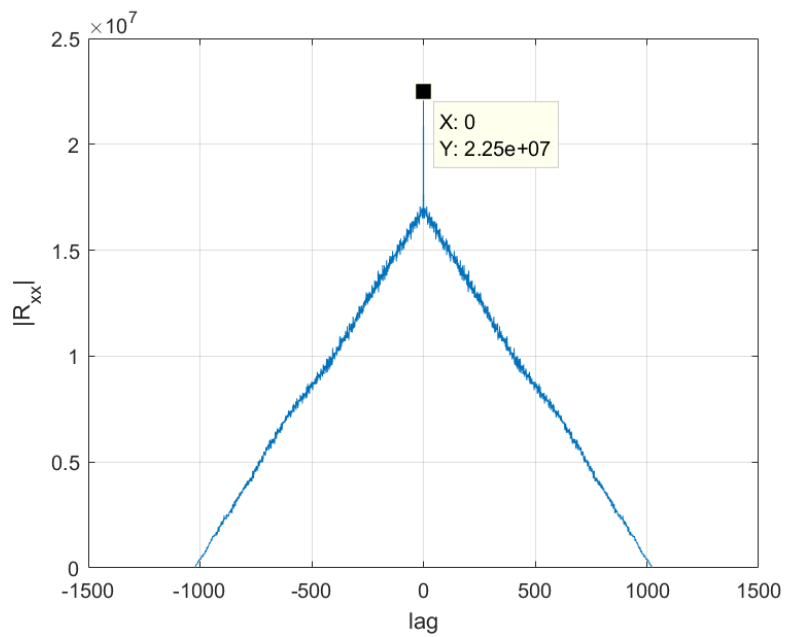


Figure 36. Simulated 4 MHz uniform white noise transmit and receive symbol correlation for a multiple (four) SDR collection. Symbol synchronization has been effected with the resultant symbol vectors now ready for probability of error evaluation.

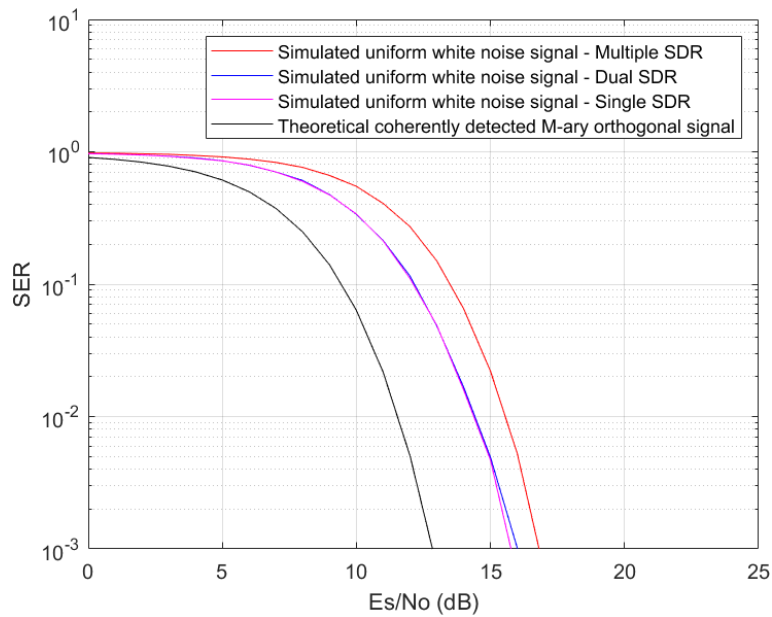


Figure 37. Monte Carlo simulation for the 4 MHz uniform white noise SER versus  $E_s/N_0$  for 0 to 25 dB, for single, dual and multiple SDR collections.

### 4.3 Hardware Test Results

This section shows results for the single, dual and multiple receiver hardware tests. Section 4.3.1 show the results for the single receiver hardware tests. Section 4.3.2 show the results for the dual receiver hardware tests and Section 4.3.3 provides the multiple receiver hardware test results.

#### 4.3.1 Single Receiver Hardware Test Results

Section 4.3.1.1 provides single-receiver, single-channel results. The results confirm the expectation that symbol loss will occur when the transmitted signal bandwidth exceeds the receiver instantaneous bandwidth. The single-receiver, signal-channel results also show that the frequency change assumption for shorter duration signals (ms) needs to be reconsidered. Section 4.3.1.2 identifies why the single-receiver, dual-channel results can be included with the dual receiver results in Section 4.3.2.

##### 4.3.1.1 Single Receiver Single Channel Hardware Test Results

The single-receiver, single-channel hardware test results demonstrate the bandwidth limitations of a single SDR when required to collect a time-variant wide-band signal. The wide-band signal having a bandwidth exceeding that of the SDR instantaneous bandwidth. Figures 38, 39 and 40 show a scenario where the receiver bandwidth spans the transmitted signal bandwidth. Figures 41, 42 and 43 show a scenario where the transmitted signal bandwidth exceeds the B205 SDR receiver bandwidth.

Figure 38 shows the X310 SDR 50 MHz transmit bandwidth. Figure 39 shows the B205 SDR 50 MHz collection. The full span of the transmit bandwidth (50 MHz) is collected (2.375 GHz to 2.425 GHz). Figure 40 shows the symbol recovery. The auto-correlation converges to a characteristic ‘spike’ with zero lag. This is indicative of a good transmit and receive symbol correlation.

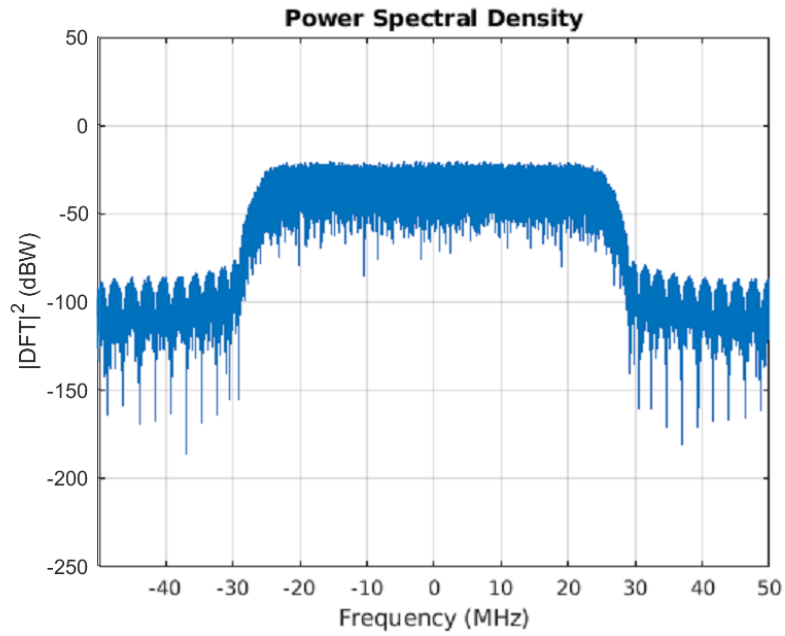


Figure 38. Single receiver hardware test PSD showing an approximate 50 MHz (at  $-3$  dB) transmit bandwidth.

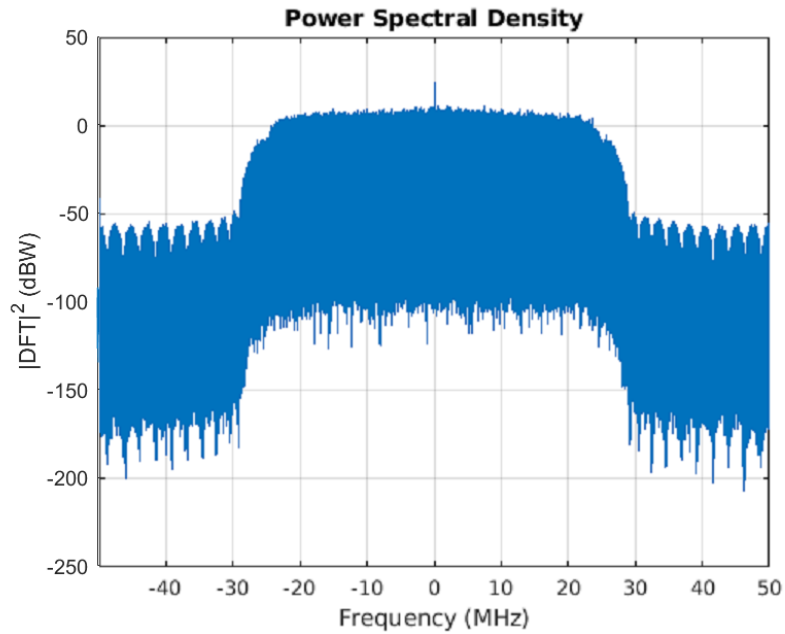


Figure 39. Single receiver hardware test PSD showing an approximate 50 MHz (at  $-3$  dB) collection bandwidth.

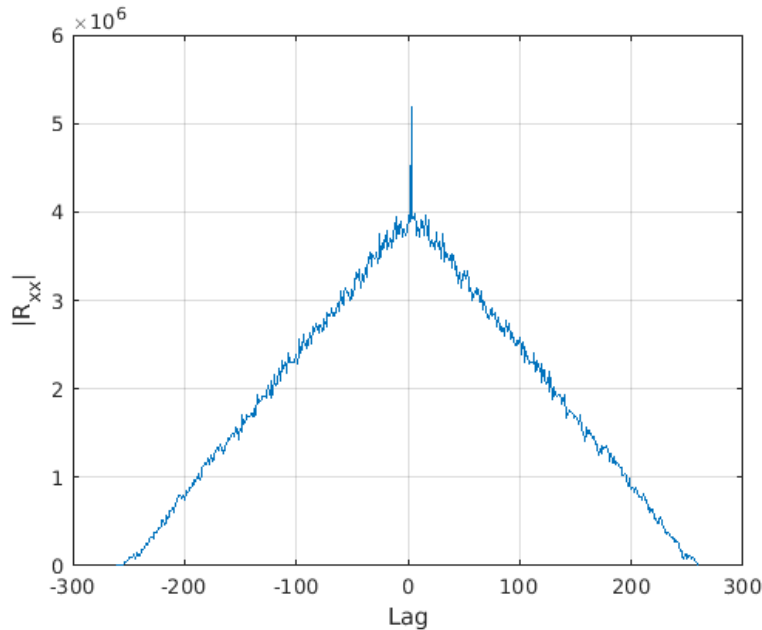


Figure 40. Single receiver hardware test plot showing a symbol recovery correlation for the approximate 50 MHz (at  $-3$  dB) collection bandwidth.

Figure 41 shows the X310 SDR 100 MHz transmit bandwidth. An attempt to collect the transmitted signal using the GNU Radio Companion (GRC) with a B205 SDR receiver sampling rate set at 100 MS/s resulted in the GRC timing out. This was expected. Reducing the receiver sampling rate to 50 MS/s resulted in the B205 SDR collecting a 50 MHz bandwidth.

Figure 42 shows the B205 SDR 50 MHz collection (2.375 GHz to 2.425 GHz). The full span of the transmit bandwidth cannot be collected (2.35 GHz to 2.45 GHz). Figure 43 shows the symbol recovery. The convergence lacks the characteristic ‘spike’. This is indicative of poor correlation. Accurate symbol recovery was not achieved. Therefore, a wide-band signal exceeding the receiver instantaneous bandwidth will not provide accurate symbol recovery using the above process. One solution is to expand the usable bandwidth by introducing additional B205 SDRs.

In Section 3.2.1 an assumption was made that the frequency offset would be constant for the short signal duration (ms) used in this research effort. Figure 44



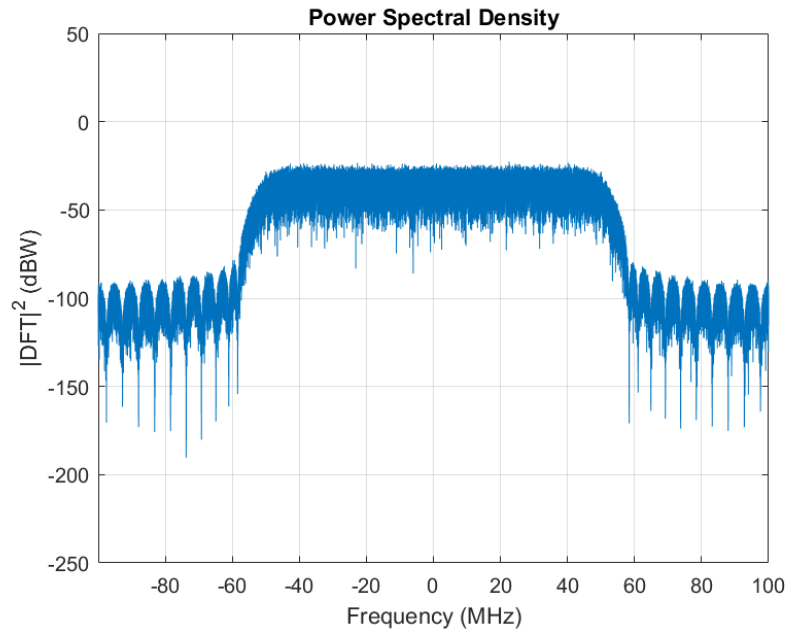


Figure 41. Single receiver hardware test PSD showing an approximate 100 MHz (at  $-3$  dB) transmit bandwidth.

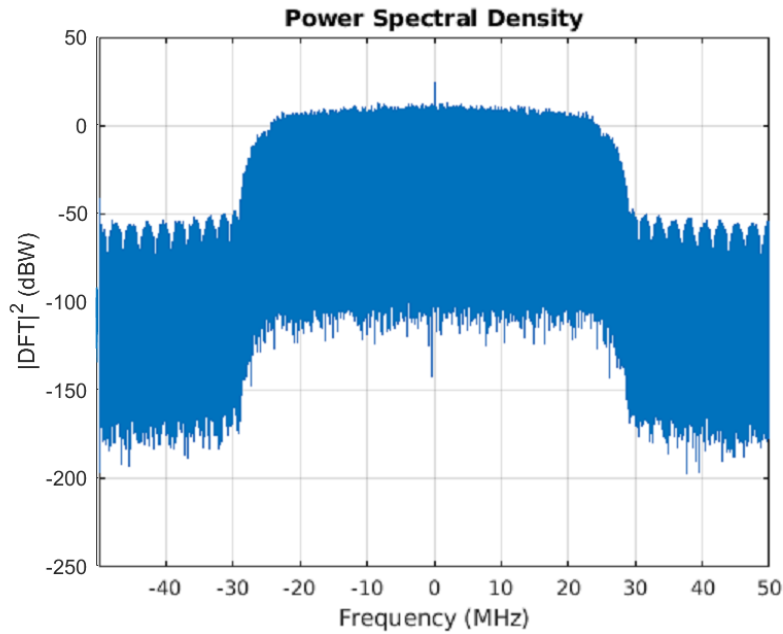


Figure 42. Single receiver hardware test PSD showing the failed 100 MHz bandwidth collection. Only an approximate 50 MHz (at  $-3$  dB) bandwidth is collected due to B205 SDR bandwidth limitations.

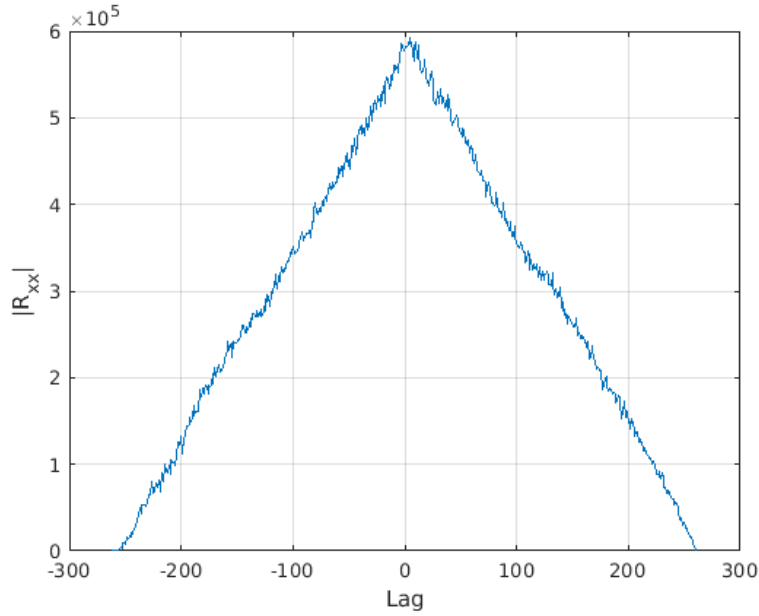


Figure 43. Single receiver hardware test plot showing a symbol recovery correlation for the failed 100 MHz collection bandwidth.

shows frequency change versus signal duration ( $\approx 400$  Hz per 50 ms). The variation was not expected and therefore our constant frequency assumption did not hold. The implications of this were not tested further. The reason for this was that the ‘open-loop’ frequency ‘pull-in’ technique repeatedly provided results similar to those seen in Figure 26.

#### 4.3.1.2 Single Receiver Dual Channel Hardware Test Results

Similar to the single-receiver, dual-channel simulation results, the single-receiver, dual-channel hardware tests and dual receiver hardware tests present the same results. Therefore, the single-receiver, dual-channel hardware test is discussed in Section 4.3.2.

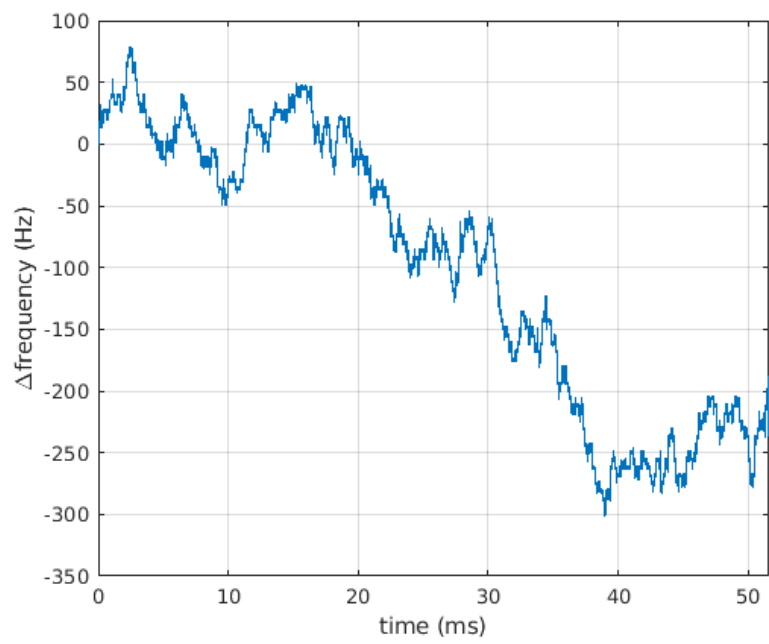


Figure 44. Hardware test frequency change versus signal duration for a uniform white noise single SDR collection.

### 4.3.2 Dual Receiver Hardware Test Results

The dual receiver hardware test SDR collections exhibit frequency and phase differences due to local oscillator drift. The frequency and phase auto-correlation plots show similar characteristics to the simulated frequency ‘pull-in’ and phase auto-correlation cases previously discussed, and therefore the frequency and phase auto-correlation plots are not presented here.

Transmit and receive PSD plots were produced for the 2 MHz QPSK and uniform white noise signal bandwidths. PSD plots for the 20 MHz and 100 MHz hardware tests were also produced for the uniform white noise signal. The 2 MHz, 20 MHz and 100 MHz PSD plots for the uniform white noise signal are presented. The QPSK plots are not presented as they do not vary significantly from the uniform white noise signal plots.

The QPSK and uniform white noise transmit signal PSD plots show the characteristic flat response spanning the defined bandwidth. Figure 45 shows the hardware test 2 MHz uniform white noise transmit signal bandwidth for a dual SDR collection. Figure 46 shows the hardware test 2 MHz uniform white noise received signal bandwidth, with each SDR sub-band collection identified. Figure 47 shows the resultant hardware test 2 MHz uniform white noise received signal bandwidth summation.

The QPSK and uniform white noise received signal PSD plots exhibit a relative attenuation of approximately  $-6$  dBW. “Relative attenuation [is] attenuation measured relative to the largest magnitude value” [11]. Attenuation is predominantly occurring at the sub-band extremities and is termed roll-off. Roll-off describes the steepness or slope in the filter response transition region [11]. The relative attenuation is attributed to X310 and B205 SDR digital up-conversion and digital down-conversion cascaded-integrator comb and half-band filters responsible for the anti-alias filtering associated with SDR sample rate conversion [42]. The up and down-conversion filters

understandably lack the roll-off characteristics achievable in Matlab<sup>®</sup> software that provided the PSD flat response seen in Figures 28 and 29. Roll-off of approximately  $-3$  dBW indicated at 0 MHz is attributed to B205 SDR cut-off filtering imposed by receive bandwidth (sample rate) selection. It is hypothesized that sub-band overlap could be used to reduce filter attenuation. This would require determining optimal sub-band overlap and resolving overlap summation errors. Overlap considerations are left as future work.

Figure 48 shows good auto-correlation between the hardware test 2 MHz uniform white noise transmit and receive symbols. Symbol recovery for the hardware test 2 MHz uniform white noise recombined signal was accurate at the  $E_s/N_0$  value inherent to each SDRs. Figure 49 shows the hardware test 2 MHz uniform white noise SER versus  $E_s/N_0$ , for a dual SDR collection. For the hardware tests the SER results are a ‘best plot’ from a limited number of runs. An SER of  $10^{-3}$  at an  $E_s/N_0$  of 18 dB is indicated. There is a 5 dB loss between the dual SDR collection SER and the theoretical M-ary signal SER, and 2 dB between the dual hardware test and simulated single SDR collection SER.

The hardware test 2 MHz QPSK and uniform white noise signal dual SDR collection were the first successful demonstrations of the auto-correlation bandwidth technique. As discussed, the focus then moved to scaling the bandwidth. Figure 50 shows a hardware test 20 MHz uniform white noise recombined signal PSD for a dual SDR collection. This was the widest bandwidth tested with the 1 Gigabit Ethernet (1G ETH) connection. This was due to the aforementioned usable bandwidth and X310 sampling rate decimation requirements.

Figure 51 shows the 100 MHz uniform white noise recombined signal PSD for a dual SDR collection. This recovery required 10 Gigabit Ethernet (10G ETH). A 100 MHz bandwidth was the widest bandwidth tested. Figure 52 shows symbol

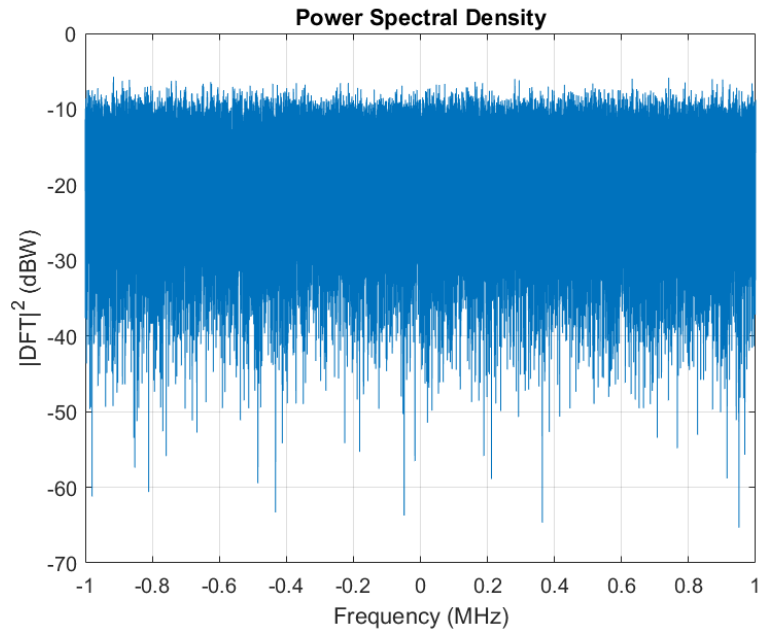


Figure 45. Hardware test 2 MHz uniform white noise transmit signal PSD for dual SDR collection.

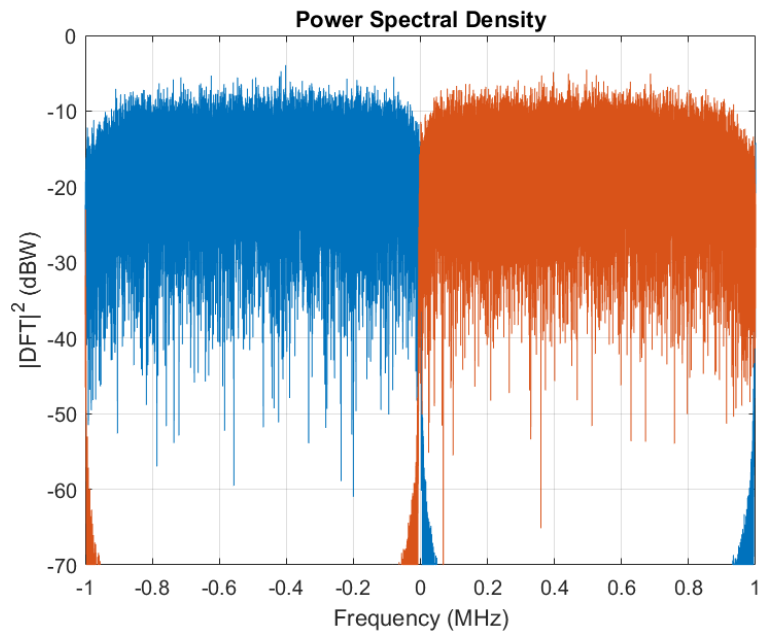


Figure 46. Hardware test 2 MHz uniform white noise overlay signal PSD showing the two 1 MHz SDR collections. Each SDR 1 MHz sub-band has undergone frequency and phase correction before being summed to recover the 2 MHz signal.

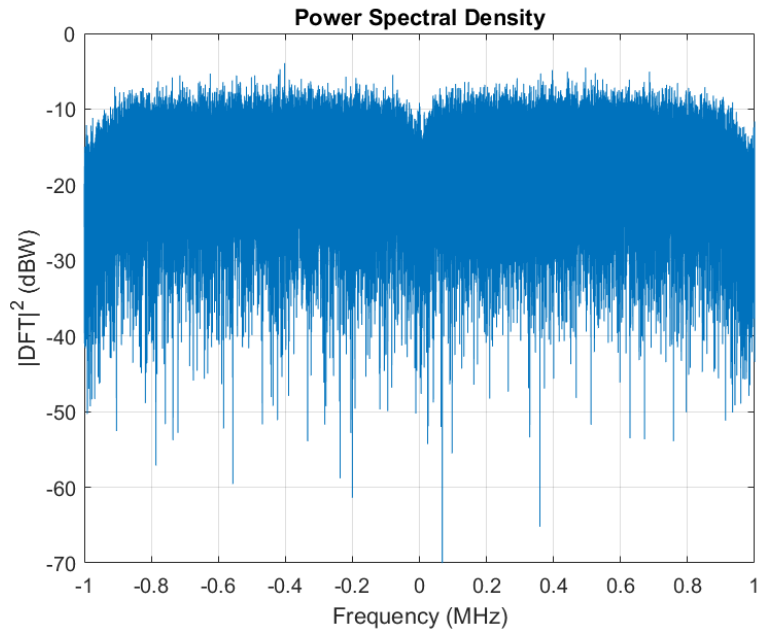


Figure 47. Hardware test 2 MHz uniform white noise recombined signal PSD for a dual SDR collection. Each SDR collected a 1 MHz sub-band which undergoes frequency and phase correction before the sub-bands are summed to recover the 2 MHz signal.

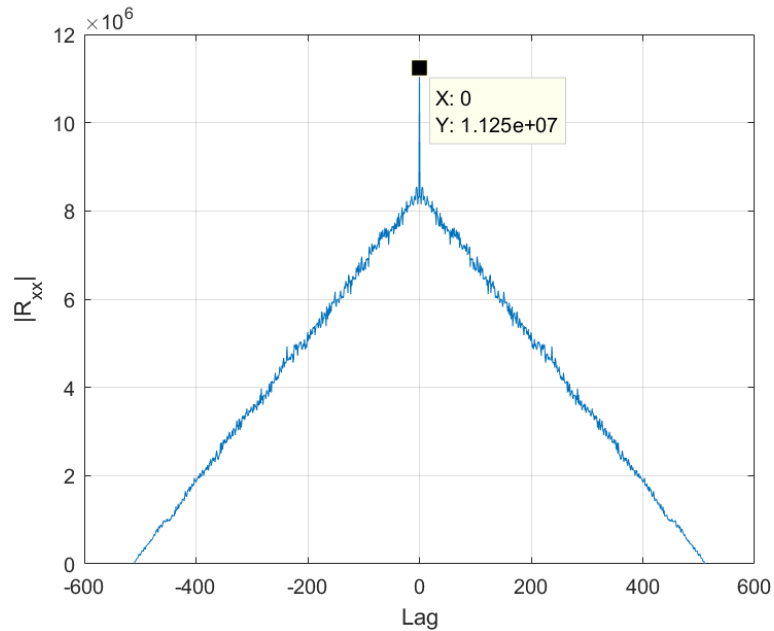


Figure 48. Hardware test 2 MHz uniform white noise transmit and receive symbol correlation for a dual SDR collection. Symbol synchronization has been effected with the resultant symbol vectors now ready for probability of error evaluation.

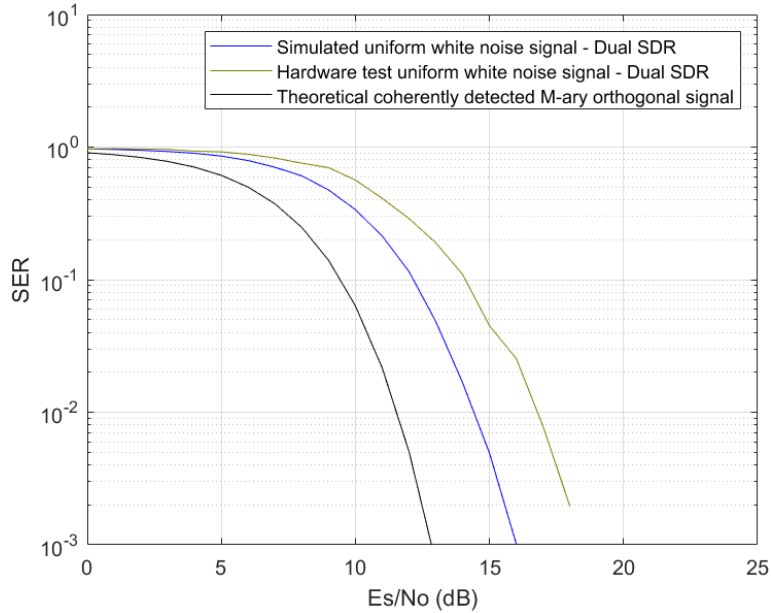


Figure 49. Hardware test 2 MHz uniform white noise SER versus  $E_s/N_0$  for 0 to 25 dB, for a dual SDR collection.

recovery for the hardware test 100 MHz uniform white noise recombined signal is accurate at the  $E_s/N_0$  value inherent to each SDRs.

Two interesting points arise from the 100 MHz hardware test. First, the PSD roll-off at 0 MHz is approximately  $-6$  dBW. This is attributed to X310 and B205 SDR digital up-conversion and digital down-conversion cascaded-integrator comb and half-band filters responsible for anti-alias filtering associated with SDR sample rate conversion. The roll-off of approximately  $-3$  dBW previously indicated at 0 MHz due to B205 SDR cut-off filtering is no longer dominant. Second, the use of 10G ETH caused GRC to display an underrun ( $'U'$ ) condition. This is interpreted as the host-PC not producing data packets fast enough for the SDR. This issue was resolved by looping the transmit signal in the GRC.



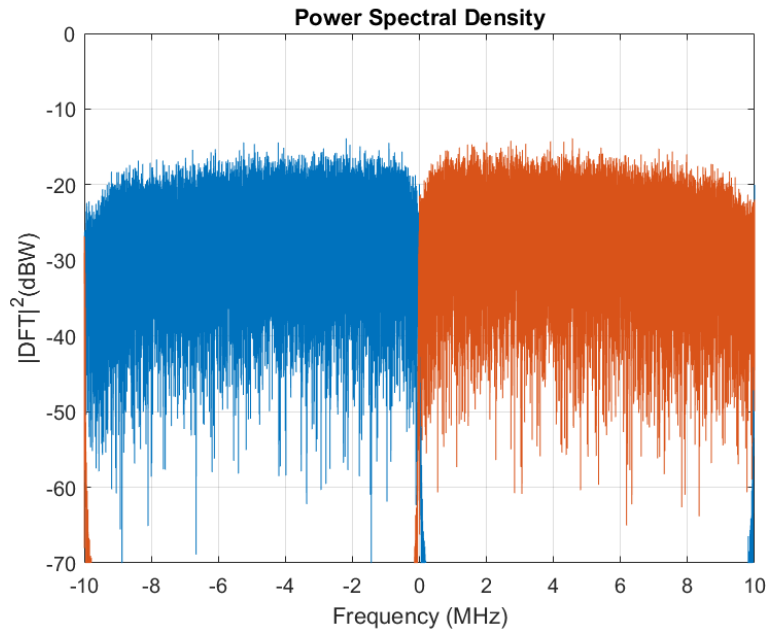


Figure 50. Hardware test 20 MHz uniform white noise overlay signal PSD showing the two 10 MHz SDR collections. The two collections are frequency and phase corrected before the sub-bands are summed to recover the 20 MHz signal.

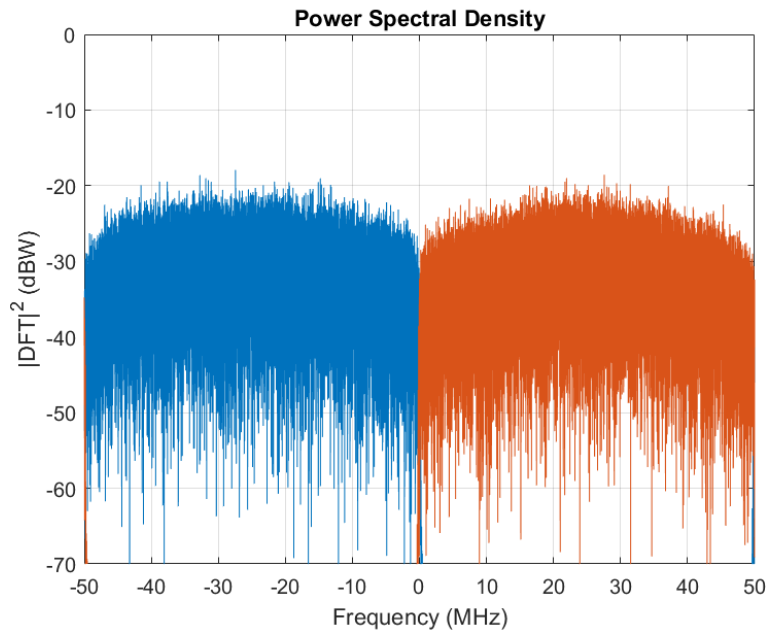


Figure 51. Hardware test 100 MHz uniform white noise overlay signal PSD for a dual SDR collection. Each SDR collected a 50 MHz sub-band which undergoes frequency and phase correction before the sub-bands are summed to recover the 100 MHz signal.

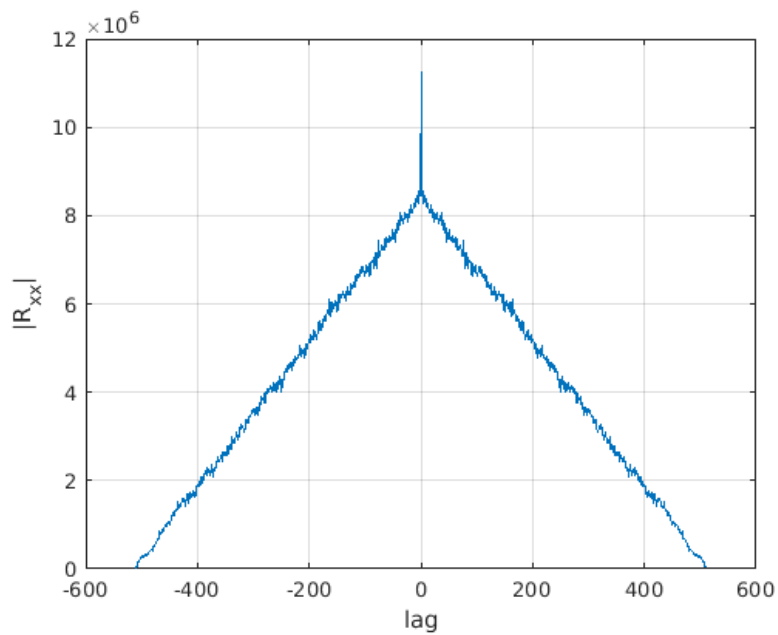


Figure 52. Hardware test 100 MHz uniform white noise transmit and receive symbol correlation for a dual SDR collection. The symbol synchronization shows that wide-band signal reconstruction exceeding a single B205 SDR instantaneous bandwidth is possible using the techniques described in this research effort.

### 4.3.3 Multiple Receiver Hardware Test Results

The multiple receiver hardware tests use four B205 SDR receivers. The SDR collections exhibit frequency and phase differences due to local oscillator drift. Frequency ‘pull-in’ auto-correlation plots are similar to those shown for the dual receiver hardware tests, and therefore frequency auto-correlation plots are not presented here. Again, phase auto-correlation plots show similar characteristics to the frequency pull-in plot for both the uncorrelated and correlated cases, and therefore phase auto-correlation plots are not presented here.

Transmit and receive PSD plots were produced for 4 MHz QPSK and uniform white noise signal bandwidths. 20 MHz and 100 MHz were also produced for the uniform white noise signal. The 4 MHz, 20 MHz and 100 MHz PSD plots for the uniform white noise signal are presented. 4 MHz QPSK plots are also presented.

The QPSK and uniform white noise transmit signal PSD plots show the characteristic flat response spanning the defined bandwidth. Figure 53 shows the 4 MHz uniform white noise transmit signal bandwidth for a multiple SDR collection. Figure 54 shows the 4 MHz uniform white noise receive signal bandwidth for the multiple SDR collection, with each SDR sub-band collection identified. Figure 55 shows the resultant 4 MHz uniform white noise receive signal bandwidth summation for the multiple SDR collection.

Similar to the dual SDR collections, PSD plots for QPSK and uniform white noise tests show a relative attenuation of  $-6$  dBW, predominantly at SDR sub-band extremities. This is attributed to X310 and B205 SDR in-built signal filtering, as described in Section 4.3.2.

Figure 56 shows the hardware test 4 MHz QPSK recombined signal PSD for the multiple SDR collection.  $R_{x_C}$  exhibits a 10 dBW loss. The issue was corrected by increasing SDR receiver gain. Figure 57 shows the hardware test 4 MHz QPSK recom-

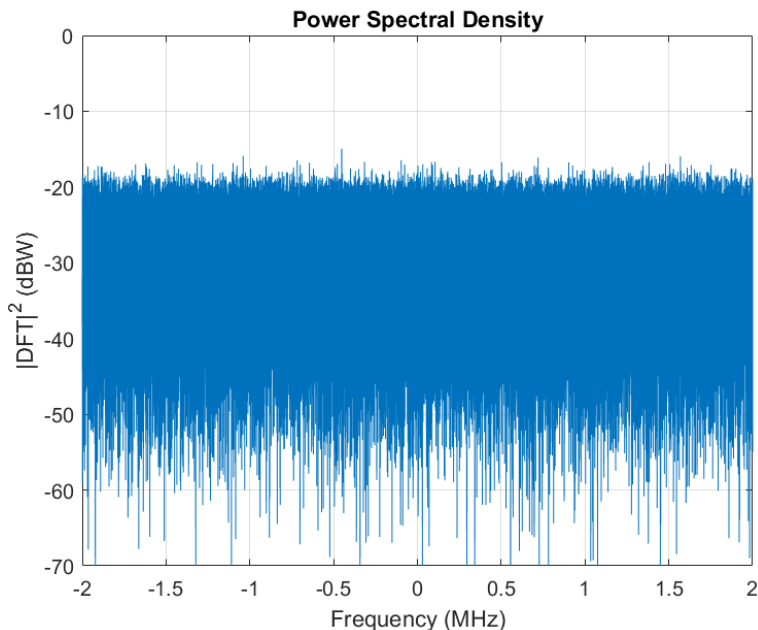


Figure 53. Hardware test 4 MHz uniform white noise transmit signal PSD for multiple SDR collection.

bined signal PSD for the multiple SDR collection, with the receiver gain corrected. GRC receiver gain settings contributed significantly to result variation in early QPSK single, dual and four receiver hardware tests. Gain settings were selected after much trial and error, and was dependent, not only on the hardware test, but time-varying factors such as receiver temperature or cable connection quality. The receiver gain issue was not apparent during uniform white noise receiver tests.

Figure 58 shows good auto-correlation between hardware test 4 MHz uniform white noise transmit and received symbols for the multiple SDR collection. Symbol recovery for the hardware test 4 MHz uniform white noise recombined signal was accurate at the  $E_s/N_0$  value inherent to each SDRs. Figure 59 shows the hardware test 4 MHz uniform white noise SER versus  $E_s/N_0$ , for a multiple SDR collection. For the hardware tests the SER results are a ‘best plot’ from a limited number of runs. An SER of  $10^{-3}$  at an  $E_s/N_0$  of 19 dB is indicated. There is a 6 dB loss between the multiple SDR collection SER and the theoretical M-ary signal SER, and a 3 dB loss

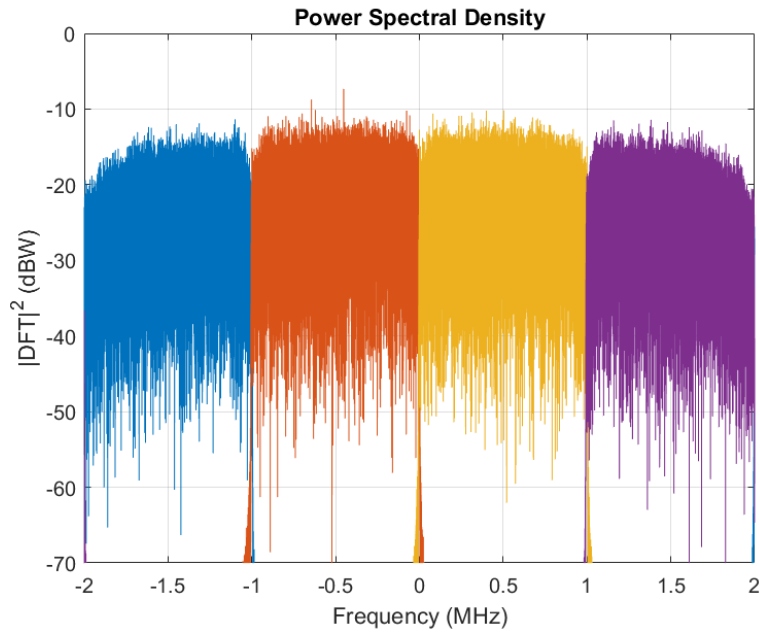


Figure 54. Hardware test 4 MHz uniform white noise overlay signal PSD showing the four 1 MHz SDR collections. Each SDR 1 MHz sub-band has undergone frequency and phase correction before being summed to recover the 4 MHz signal.

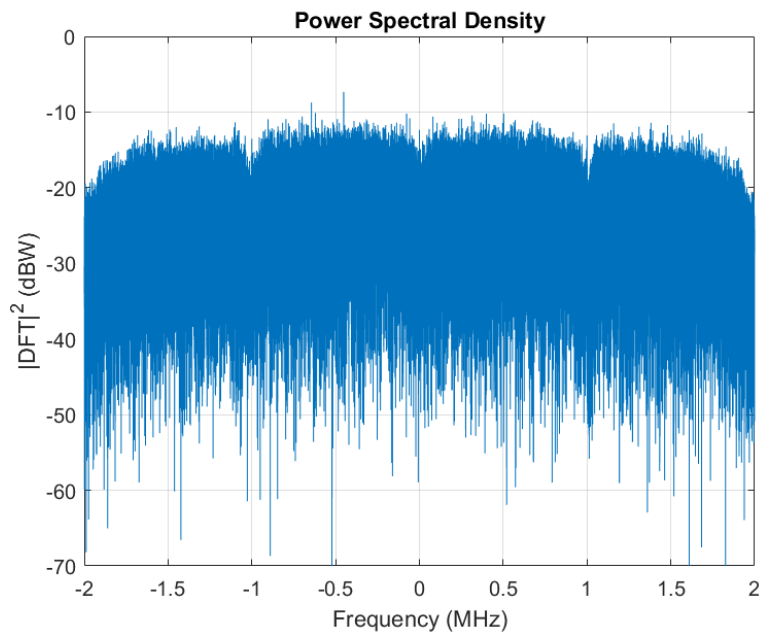


Figure 55. Hardware test 4 MHz uniform white noise recombined signal PSD for a multiple SDR collection. Each SDR collected a 1 MHz sub-band which undergoes frequency and phase correction before the sub-bands are summed to recover the 4 MHz signal.

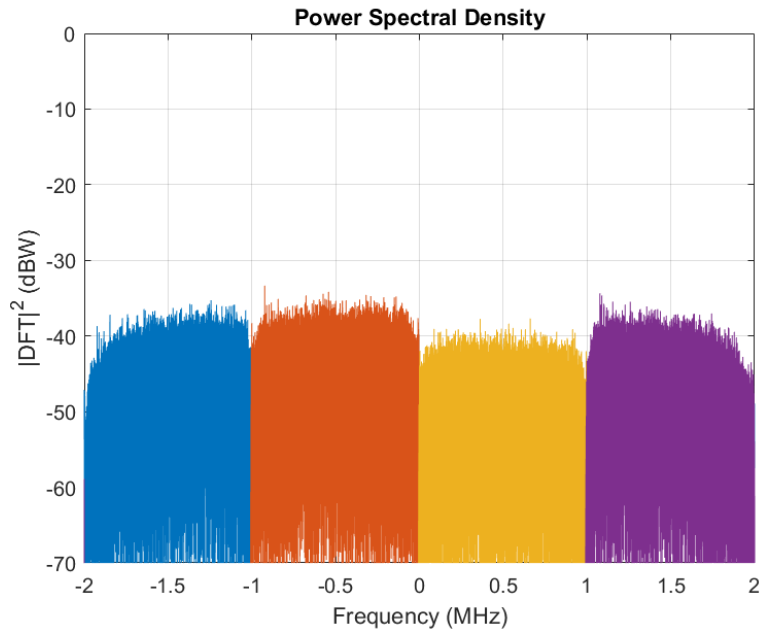


Figure 56. Hardware test 4 MHz QPSK overlay signal for a multiple SDR collection. Each SDR collected a 1 MHz sub-band which undergoes frequency and phase correction before the sub-bands are summed to recover the 4 MHz signal. Receiver gain settings require adjustment to correct the power loss in ' $Rx_C$ '.

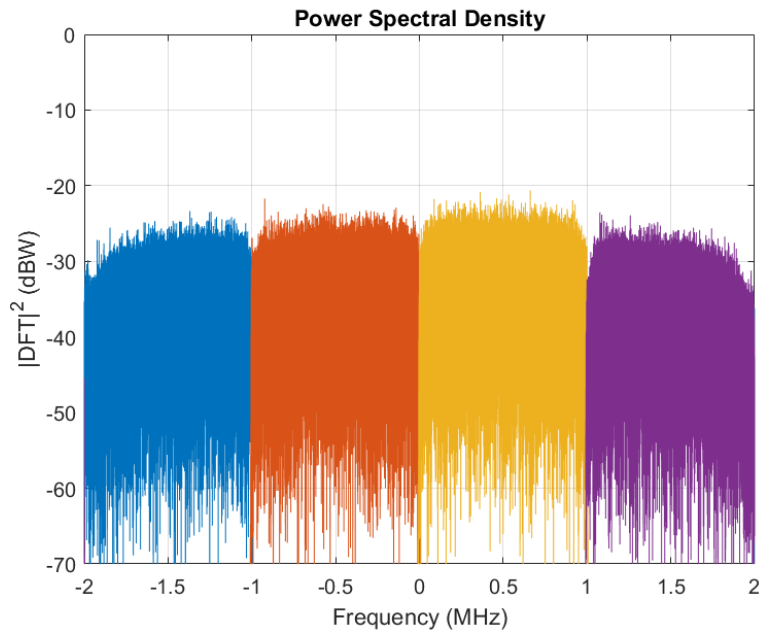


Figure 57. Hardware test 4 MHz QPSK overlay signal showing the four 1 MHz SDR collections. Receiver gain settings for all receivers have been increased. The power loss issue with ' $Rx_C$ ' is no longer apparent.

between the multiple SDR collection SER and the simulated single SDR collection SER.

The 4 MHz hardware test was the first successful demonstration of the auto-correlation bandwidth technique using multiple receivers. The focus shifted to increasing single SDR bandwidth use, followed by bandwidth recovery exceeding single SDR instantaneous bandwidth limits. Again, a simple sampling rate adjustment and center frequency recalculation for each sub-band were the only variable changes required to extend recoverable bandwidth limits.

As with the dual SDR recovery, as long as sampling rate settings were consistent with X310 SDR sample rate decimation requirements and the 1G ETH bit-rate was not exceeded, bandwidth recovery could be extended to 20 MHz. Figure 60 shows a hardware test 20 MHz uniform white noise recombined signal for a multiple SDR collection. This is the widest bandwidth tested with the 1G ETH connection. Symbol recovery for the hardware test 20 MHz uniform white noise recombined signal is accurate at the  $E_s/N_0$  value inherent to each SDRs.

Figure 61 shows the 100 MHz uniform white noise recombined signal PSD for a multiple SDR recovery. Figure 62 shows symbol recovery for the hardware test 100 MHz uniform white noise recombined signal is accurate at the  $E_s/N_0$  value inherent to each SDRs. A 100 MHz bandwidth was the widest bandwidth tested for the multiple SDR receiver case.

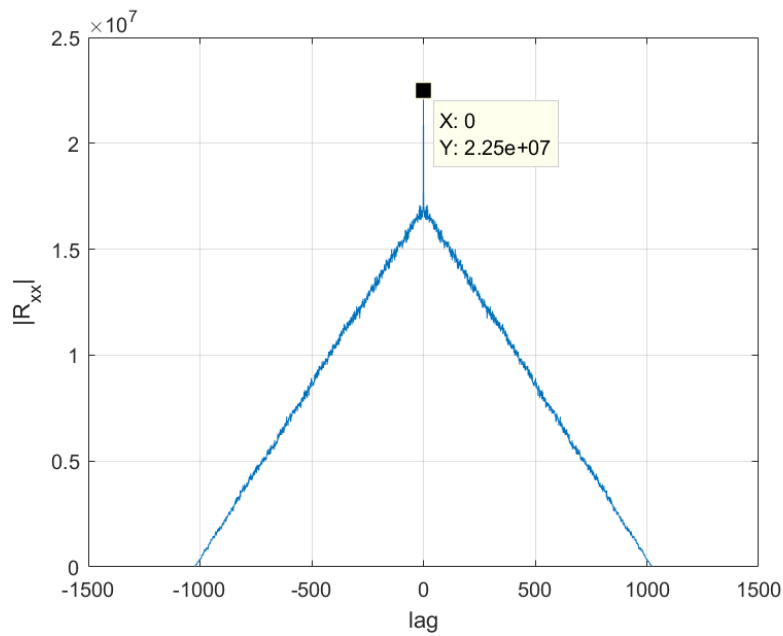


Figure 58. Hardware test 4 MHz uniform white noise transmit and receive symbol correlation for a multiple (four) SDR collection. Symbol synchronization has been effected with the resultant symbol vectors now ready for probability of error evaluation.

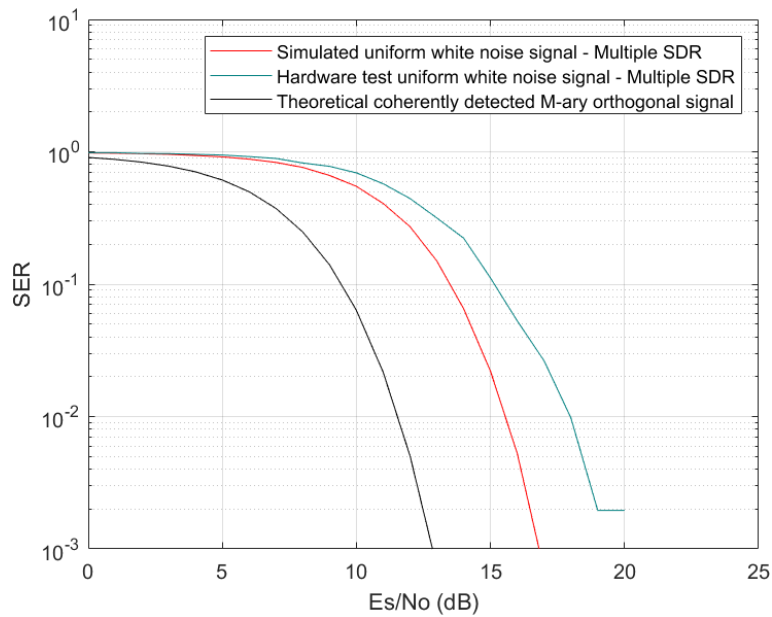


Figure 59. Hardware test 4 MHz uniform white noise SER versus  $E_s/N_0$  for 0 to 25 dB, for a multiple SDR collection.



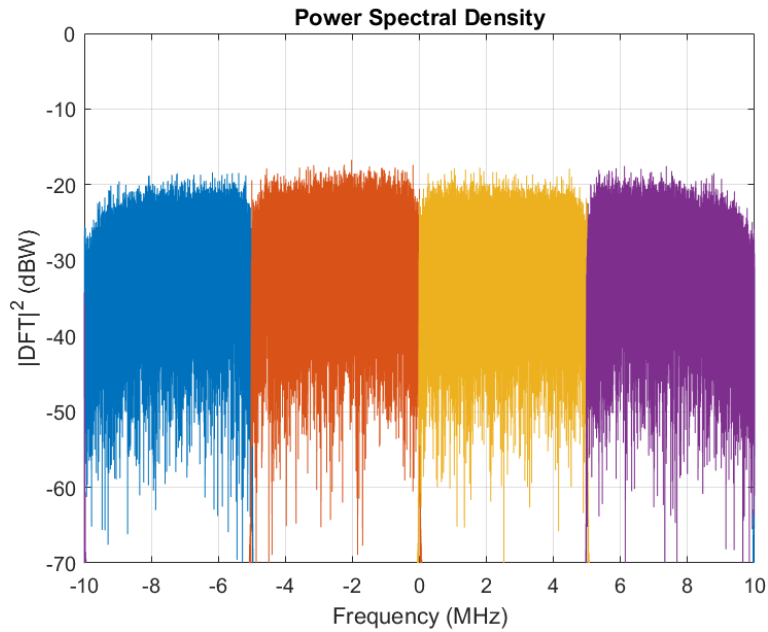


Figure 60. Hardware test 20 MHz uniform white noise overlay signal showing the four 5 MHz SDR collections. Each SDR 5 MHz sub-band has undergone frequency and phase correction before being summed to recover the 20 MHz signal.

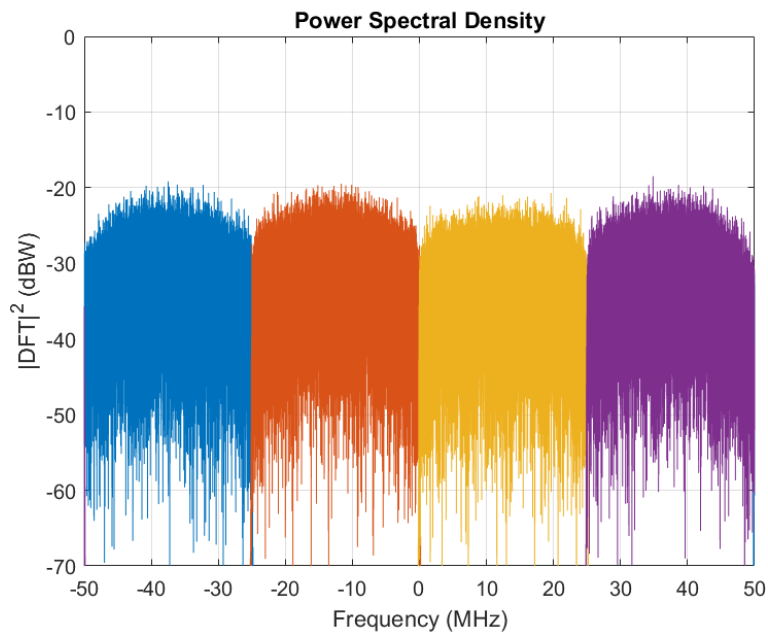


Figure 61. Hardware test 100 MHz uniform white noise overlay signal showing the four 25 MHz SDR collections. Each SDR collected a 25 MHz sub-band which undergoes frequency and phase correction before the sub-bands are summed to recover the 100 MHz signal.

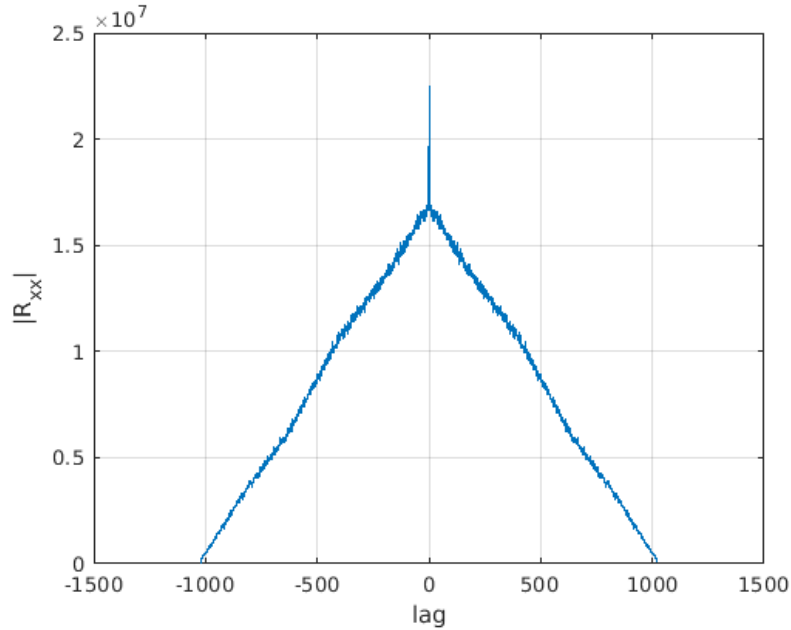


Figure 62. Hardware test 100 MHz uniform white noise transmit and receive symbol correlation for a multiple (four) SDR collection. The symbol synchronization shows that wide-band signal reconstruction exceeding a single B205 SDR instantaneous bandwidth is possible using the techniques described in this research effort.

#### 4.4 RFDNA Test Results

The intent of the RF-DNA test case was to demonstrate a real-world application for the auto-correlation bandwidth expansion technique. However, the proposed RF-DNA test was not conducted and is left as future work.

#### 4.5 Summary

Chapter IV detailed research effort results and analysis. The results show that a uniform white noise transmit signal, with a bandwidth exceeding a single B205 SDR instantaneous bandwidth, can be simultaneously collected and reconstructed using multiple SDRs and the described auto-correlation bandwidth expansion technique. The auto-correlation technique requires no overlap of the collected sub-bands. PSD plots for single, dual and multiple SDR receiver simulations and hardware tests for

transmit bandwidths of 2 MHz, 4 MHz, 20 MHz and 100 MHz demonstrate the technique is scalable.

The research culminates with two 100 MHz bandwidth hardware tests. The two uniform white noise hardware tests use a two B205 SDR and a four B205 SDR collection. Symbol recovery for the two hardware tests were accurate at the  $E_s/N_0$  value inherent to each SDRs. Chapter V will provide research effort conclusions and future work recommendations.

## V. Conclusion

The research objective was to demonstrate wide-band signal response collection simultaneously spanning multiple Software Defined Radio (SDR) narrow-band receiver bandwidths using a uniform white noise signal. The simultaneous collections were then recombined to provide a wide-band receive signal. The receive signal was then demodulated to provide accurate symbol recovery. This objective had two requirements:

- A hardware test should be developed to demonstrate collection and reconstruction of a signal bandwidth exceeding that of an individual SDR instantaneous bandwidth.
- A hardware test should be developed to demonstrate collection and reconstruction of a signal using multiple SDRs.

An additional objective was to determine the minimum number of SDRs required to collect the full span of a transmit signal bandwidth.

The initial attempts to develop hardware tests using Everett's cross-correlation techniques met with some difficulty [8]. While always intending to substitute a uniform white noise signal for the Quadrature Phase Shift Keying (QPSK) signal, a successful outcome would have provided a useful baseline for further bandwidth expansion development. The full replication of Everett's technique was ultimately abandoned in favor of an alternate approach. The alternate approach used auto-correlation to exploit a known a priori transmit signal.

As seen, in Chapter IV, the auto-correlation technique was able to recover the uniform white noise signal. Indeed, while this research effort did not achieve all the objectives, there were three significant outcomes that progress Non-Destructive Evaluation (NDE) system development. These outcomes were:

- The successful simulation and hardware testing of an auto-correlation bandwidth expansion technique using dual and multiple B205 SDRs to collect and restore a uniform white noise signal with a bandwidth of 100 MHz. This bandwidth is greater than the instantaneous bandwidth of the B205 SDR. Previous research efforts used two SDRs to recover a 1.98 MHz bandwidth from a 2 MHz QPSK signal.
- The successful simulation and hardware testing of an auto-correlation bandwidth expansion technique for simultaneous collection and reconstruction of QPSK or uniform white noise signals, using more than two SDRs.
- The successful development and application of a uniform white noise signal comprised of complex symbols, drawn randomly without replacement. Previous research efforts used communication-centric signals (e.g. QPSK). This outcome demonstrated noise signals similar to that generated by the Air Force Institute of Technology (AFIT) Noise Radar Network (NoNET) could be recovered by light-weight, low-cost and low-complexity SDRs.

One further issue raised as future work in [8] was resolved during this research effort. The issue required transmit spike elimination. As discussed, the transmit spike presented if a DC bias was coded into the transmit signal. Offsetting complex symbol inputs so both real and imaginary values were uniformly distributed with zero mean eliminated the observed transmit spike.

This research effort restricted overlap to that part of the bandwidth extending beyond the pass-band cut-off frequency. The bandwidth expansion auto-correlation technique is therefore optimized for equation (29). Further, the minimal code changes required to transition from a dual to multiple SDR collection suggests the technique is scalable.

## 5.1 Future Work

Due to difficulties with the modelling process, the XTRX SDR bandwidth expansion technique transfer was not investigated. The intended Radio Frequency-Distinct Native Attribute (RF-DNA) test was also not conducted. Additionally, the extent of intended bandwidth expansion was limited by hardware restrictions and sampling considerations, primarily due to host-PC and SDR analog bandwidth restrictions. A further hardware consideration is the effect of SDR filter attenuation. Consequently, there is still further work to do.

### 5.1.1 Bandwidth Expansion Technique Transfer

To confirm whether the auto-correlation bandwidth expansion technique developed in this research effort is transferable, it is recommended that the auto-correlation bandwidth expansion technique be tested using alternate SDR hardware. A transferable process would allow future NDE hardware to be tailored to user needs. The Fairwaves XTRX and Blade RF SDRs are suggested as suitable alternatives for this work.

### 5.1.2 Alternate Support Hardware Tests

The constraints imposed on sampling rates by the low-complexity Universal Software Radio Peripheral (USRP) devices and the bit-rates supported by 1 Gigabit Ethernet (1G ETH) restricted bandwidth expansion to approximately 20 MHz. Expansion beyond this limit, and dependent on sample rate interpolation and decimation settings sometimes within this limit, caused buffer overflow ‘O’ conditions. While B205 SDR documentation noted that buffer overflow is “generally harmless” this was not the case for hardware tests [40].

Alternative host-PC hardware and 10 Gigabit Ethernet (10G ETH) with pro-

cessing capability sufficient to support wider instantaneous bandwidth data transfer still restricted tests to a 100 MHz transmit signal bandwidth. Sourcing a host-PC, and commercial-off-the-shelf portable transmit hardware able to support the NoNET bandwidth (395 – 720 MHz) is necessary to further auto-correlation bandwidth technique investigation.

### 5.1.3 SDR Filter Attenuation

Figures 46, 47, 54 and 55 show the attenuation attributed to SDR transmitter and receiver in-built filters. Losses due to filtering need to be quantified. A proposed hypothesis is that the  $EsNo$  degradation experienced during this research effort is in part attributable to the filters. If the losses are significant, a bandwidth overlap process could be developed to reduce filter attenuation effects and create a contiguous flat bandwidth response. This would have implications for equation (29). Increasing overlap would require an increasing number of receivers to span the same wide-band transmit signal bandwidth. Comparative tests to optimize the number of receivers versus the required bandwidth overlap could then be conducted.

### 5.1.4 RF-DNA Tests

The intended RF-DNA hardware test did not occur. This was unfortunate as a RF-DNA test provides an NDE of a Device Under Test (DUT). A successful NDE test would show the real-world application of the auto-correlation bandwidth expansion technique. A successful test would also provide further cases of uniform white noise signal use in the RF-DNA field.

## Appendix A: Non-Linear Least Squares Estimation

The estimate aims to provide the best possible solution for a non-linear system. The proof, found in [26], is repeated here with additional equations and explanation for completeness. Despite the insertion of additional equations and explanation, this appendix is not claimed as independent work. The equations and a large portion of the text are copied from [26]. The proof begins with a statement of the Non-Linear Least Squares (NLS) criteria for (38),

$$\min_{\alpha, \omega, x} \|y - \alpha Dx\|^2, \quad (38)$$

where  $y = [y(0), y(1), \dots, y(N-1)]^T$ ,  $x = [x(0), x(1), \dots, x(N-1)]^T$ ,  $D = \text{diag}(1, e^{j\omega}, \dots, e^{j(N-1)\omega})$ ,  $N$  is the number of samples and  $T$  is the transpose operator, with  $\alpha$  being the least squares solution [26]. Minimizing the sum of squares (38) is the same as minimizing (39),

$$\min_{\alpha, \omega, x} (y - \alpha Dx), \quad (39)$$

To minimize (39) identification of the normal equation is required. The normal equation is (40),

$$x^T((y - \alpha Dx) = 0, \quad (40)$$

where  $x^T$  indicates the transpose of  $x$  [26]. Expanding (40) rearranging and isolating for  $\alpha$  provides (41), (42) and (43),

$$x^T y - x^T \alpha Dx = 0, \quad (41)$$

$$x^T y = x^T \alpha Dx, \quad (42)$$



$$\alpha = x^T D^* y / x^T x, \quad (43)$$

where  $*$  indicates the complex conjugate [26]. Substituting (43) in (42) provides a solution for minimizing  $\alpha$  (44),

$$\min_{\omega, x} \|(I - Dxx^T D^* / x^T x)y\|^2, \quad (44)$$

which equates to maximizing (45),

$$y^* Dxx^T D^* y / x^T x = |x^T z|^2 / x^T x, \quad (45)$$

where  $z = D^* y$  is a function of  $\omega$  [26]. To maximize (45) with respect to  $x \in \mathfrak{R}^{N \times 1}$ , let,

$$z = z_r + iz_i, \quad (46)$$

and observe that,

$$|x^T z|^2 = (x^T z_r)^2 + (x^T z_i)^2 = x^T [z_r \ z_i] \begin{bmatrix} z_r^T \\ z_i^T \end{bmatrix} x = x^T Z Z^T x, \quad (47)$$

Next let,

$$Z^T Z = U \begin{bmatrix} \lambda_1 & 0 \\ 0 & \lambda_2 \end{bmatrix} U^T = U \Lambda U^T, \quad (48)$$

denote the eigenvalue decomposition of the  $2 \times 2$  matrix  $Z^T Z$  where  $\lambda_1 \geq \lambda_2$  and  $U = [u_1 \ u_2]$  is an orthogonal matrix [26]. Note that generically we have  $\lambda_1 > \lambda_2$ , which we assume in the following. A simple calculation shows that,

$$\begin{aligned}
(ZZ^T) \times \underbrace{Z(Z^T Z)^{-1/2}U}_V &= Z(Z^T Z)^{1/2}U \\
&= Z(Z^T Z)^{-1/2}U \times \underbrace{U^T(Z^T Z)U}_\Lambda \\
&= V\Lambda,
\end{aligned} \tag{49}$$

where  $(\cdot)^{1/2}$  denotes the square root of the matrix between parentheses [26]. The  $N \times N$  matrix  $ZZ^T$  has  $N - 2$  eigenvalues equal to zero. It follows from (49) that the other two eigenvalues of  $ZZ^T$  are equal to  $\lambda_1, \lambda_2$  and, also, that the eigenvector associated with  $\lambda_1$  is given by,

$$v_1 = Z(Z^T Z)^{-1/2}u_1, \tag{50}$$

Since we have assumed that  $\|x\| = 1$ , it follows that the maximum of the function in (45),(47) with respect to  $x$  is obtained for

$$\hat{x} = v_1, \tag{51}$$

and that,

$$\hat{\omega} = \arg \max_{\omega} \lambda_1(\omega), \tag{52}$$

A closed-form expression for  $\lambda_1(\omega)$  can be readily obtained as,

$$\begin{bmatrix} z_r^T z_r - \lambda & z_r^T z_i \\ z_r^T z_i & z_i^T z_i - \lambda \end{bmatrix} = \lambda^2 - \lambda(z_r^T z_r + z_i^T z_i) + (z_r^T z_r)(z_i^T z_i) - (z_r^T z_i)^2, \tag{53}$$

we obtain,

$$2\lambda_1 = (z_r^T z_r + z_i^T z_i) + [(z_r^T z_r - z_i^T z_i)^2 + 4(z_r^T z_i)^2]^{1/2}, \tag{54}$$

Now,

$$z_r^T z_r + z_i^T z_i = z^* z, \quad (55)$$

$$(z_r^T z_r - Z_i^T z_i)^2 + 4(z_r^T z_i)^2 = |z^T z|^2, \quad (56)$$

Hence,  $\hat{\omega}_0$  is obtained by maximizing,

$$z^* z + |z^T z|, \quad (57)$$

Since  $z^* z$  does not depend on  $\omega$ , it follows that the NLS frequency estimate is given by,

$$\hat{\omega}_0 = \arg \max_{\omega} \frac{1}{N} \left| \sum_{n=0}^{N-1} y^2(n) e^{-j2\omega n} \right|^2, \quad (58)$$

This completes the proof.

## Appendix B: Simulation Summary

Table 12. Bandwidth expansion simulations.

Simulation	Simulation description
1	QPSK signal communications system validation simulation
2	Uniform white noise signal communications system validation simulation
3	QPSK signal single receiver dual-channel simulation
4	Uniform white noise signal single receiver dual-channel simulation
5	QPSK signal dual receiver 2 MHz simulation
6	Uniform white noise signal dual receiver 2 MHz simulation
7	QPSK signal dual receiver 20 MHz simulation
8	Uniform white noise signal dual receiver 20 MHz simulation
9	QPSK signal dual receiver 100 MHz simulation
10	Uniform white noise signal dual receiver 100 MHz simulation
11	QPSK signal multiple (four) receiver 4 MHz simulation
12	Uniform white noise signal multiple (four) receiver 4 MHz simulation
13	QPSK signal multiple (four) receiver 20 MHz simulation
14	Uniform white noise signal multiple (four) receiver 20 MHz simulation
15	QPSK signal multiple (four) receiver 100 MHz simulation
16	Uniform white noise signal multiple (four) receiver 100 MHz simulation

## Appendix C: Hardware Test Summary

Table 13. Bandwidth expansion hardware tests.

Hardware test	Hardware test description
1	Single SDR receiver hardware test using a 2 MHz QPSK transmission signal
2	Single SDR receiver hardware test using a 2 MHz uniform white noise transmission signal
3	Dual SDR receiver hardware test using a 2 MHz QPSK transmission signal
4	Dual SDR receiver hardware test using a 2 MHz uniform white noise transmission signal
5	Dual SDR receiver hardware test using a 20 MHz uniform white noise transmission signal
6	Dual SDR receiver hardware test using a 100 MHz uniform white noise transmission signal
7	Multiple (four) SDR receiver hardware test using a 4 MHz QPSK transmission signal
8	Multiple (four) SDR receiver hardware test using a 4 MHz uniform white noise transmission signal
9	Multiple (four) SDR receiver hardware test using a 20 MHz uniform white noise transmission signal
10	Multiple (four) SDR receiver hardware test using a 100 MHz uniform white noise transmission signal

## Bibliography

1. R. C. McMaster, *Nondestructive Testing Handbook, Vol 1*. The Ronald Press Company, New York, NY, 1959.
2. M. W. Lukacs, P. J. Collins, and M. A. Temple, “Interrogation Signal Optimization for Improved Classifier Performance when using for Non-Destructive Antenna Acceptance Testing,” *Proceedings of the Antenna Measurement Techniques Association 37th Annual Symposium*, pp. 1–6, 2015.
3. M. W. Lukacs, P. J. Collins, and M. A. Temple, ““RF-DNA” Fingerprinting for Non-Destructive Antenna Acceptance Testing,” *Proceedings of the Antenna Measurement Techniques Association 36th Annual Symposium*, pp. 314–319, 2014.
4. M. W. Lukacs, A. J. Zeqolari, P. J. Collins, and M. A. Temple, “RF-DNA Fingerprinting for Antenna Classification,” *IEEE Antennas and Wireless Propagation Letters*, 2015.
5. M. A. Temple, P. J. Collins, and M. W. Lukacs, “Classification performance using ‘RF-DNA’ fingerprinting of ultra-wideband noise waveforms,” *Electronics Letters*, vol. 51, no. 10, pp. 787–789, 2015.
6. M. W. Lukacs, P. J. Collins, and M. A. Temple, “Device Identification Using Active Noise Interrogation and RF-DNA Fingerprinting for Non-Destructive Amplifier Acceptance Testing,” *2016 IEEE 17th Annual Wireless and Microwave Technology Conference (WAMICON)*, pp. 1–6, 2016.
7. A. J. Paul, P. J. Collins, and M. A. Temple, “Nondestructive Evaluation of Radio Frequency Connector Continuity Using Stimulated Emissions,” *Journal of Nondestructive Evaluation, Diagnostics and Prognostics of Engineering Systems*, vol. 2, no. 1, p. 011010, 2018.

8. N. Everett, “Instantaneous bandwidth expansion using software defined radios,” Master’s thesis, Air Force Institute of Technology, 2019.
9. B. Stewart, K. Barlee, D. Atkinson, and L. Crockett, *Software Defined Radio using MATLAB and Simulink and the RTL-SDR*. Strathclyde Academic Media, Ltd., G43 2DX Glasgow, UK, 2015.
10. “Ettus Research USRP B205 mini Software Defined Radio [Product Datasheet],” Ettus Research, National Instruments, Santa Clara, CA, 2010.
11. R. G. Lyons, *Understanding Digital Signal Processing, Second Edition*. Pearson Education Inc., Upper Saddle River, NJ, 2004.
12. S. L. Miller and D. Childers, *Probability and Random Processes, Second Edition*. Academic Press, Waltham, MA, 2012.
13. J. Hardin, “Information encoding on a pseudo random noise radar waveform,” Master’s thesis, Air Force Institute of Technology, 2013.
14. P. J. Collins and J. A. Priestly, “Trading spectral efficiency for system latency in true-random noise radar network through template-replay diversity,” *2012 International Waveform Diversity & Design Conference (WDD)*, pp. 238–242, 2012.
15. A. Hauser, B. Fenski, and L. Cavalli, “Maximize Asset Availability and Reduce Maintenance Costs - an Integrated Approach Combining Condition Assessment with Data Analytics,” *24th International Conference & Exhibition on Electricity Distribution (CIRED)*, pp. 316–319, 2017.
16. “RF Agile Transceiver AD9364 [Product Datasheet],” Analog Devices, Norwood, MA, 2014.

17. “Ettus Research USRP X310 Software Defined Radio [Product Datasheet],” Ettus Research, National Instruments, Santa Clara, CA, 2010.
18. “GNU Radio,” The GNU Radio Foundation, Inc., The Free Software Foundation, Boston, MA, 2020.
19. J. S. Beasley and G. M. Miller, *Modern Electronic Communication, Ninth Edition*. Pearson Education Inc., Upper Saddle River, NJ, 2008.
20. E. Zenteno, M. Isaksson, and P. Händel, “Pilot tone aided measurements to extend the bandwidth of radio frequency applications,” *Measurement: Journal of the International Measurement Confederation*, vol. 90, pp. 534–541, 2016.
21. D. Wisell, D. Rönnow, and P. Händel, “A Technique to Extend the Bandwidth of an RF Power Amplifier Test Bed,” *IEEE Transactions on Instrumentation and Measurement*, vol. 56, no. 4, pp. 1488–1494, 2007.
22. K. A. Remley, D. F. Williams, D. M. Schreurs, L. Giovanni, and A. Cidronal, “Phase Detrending for Measured Multisine Signals \*,” *In: 61st ARFTG Conference Digest Spring 2003*, pp. 73–83, 2003.
23. E. D. Kaplan and C. J. Hegarty, *Understanding GPS Principles and Applications, Second Edition*. Artech House, Inc., Norwood, MA, 2006.
24. B. Sklar, *Digital Communications Fundamentals and Applications, Second Edition*. Prentice Hall Inc., Upper Saddle River, NJ, 2001.
25. D. Sorensen, C. Lindstrom, and J. Gunther, “Exponent: Arbitrary Bandwidth Receiver Architecture,” *Proceedings of the GNU Radio Conference*, vol. 4, no. 1, 2019.



26. O. Besson and P. Stoica, "Frequency estimation and detection for sinusoidal signals with arbitrary envelope: a nonlinear least-squares approach," *Digital Signal Processing*, vol. 56, no. 1999, pp. 2209–2212, 2002.
27. Y. Wang, K. Shi, and E. Serpedin, "Non-Data-Aided Feed-Forward Carrier Frequency Offset Estimators for QAM Constellations: A Non-Linear Least-Squares Approach," *Eurasip Journal on Applied Signal Processing*, vol. 2004, no. 13, pp. 1993–2001, 2004.
28. U. Mengali and M. Morelli, "Data-Aided Frequency Estimation for Burst Digital Transmission," *IEEE Transactions on Communication*, vol. 45, no. 1, pp. 23–25, 1997.
29. J. G. Proakis, *Digital Communications, Third Edition*. McGraw Hill., New York, NY, 1995.
30. B. P. Lathi and Z. Ding, *Modern Digital and Analog Communication Systems, Fourth Edition*. Oxford University Press., New York, NY, 2009.
31. R. W. Klein, M. A. Temple, and M. J. Mendenhall, "Application of Wavelet-Based RF Fingerprinting to Enhance Wireless Network Security," *Journal of Communications and Networks*, vol. 11, no. 6, pp. 544–555, 2009.
32. C. K. Dubendorfer, B. W. Ramsey, and M. A. Temple, "An RF-DNA Verification Process for ZigBee Networks," *Proceedings - IEEE Military Communications Conference MILCOM*, pp. 1–6, 2012.
33. D. R. Reising, M. A. Temple, and J. A. Jackson, "Authorized and Rogue Device Discrimination Using Dimensionally Reduced RF-DNA Fingerprints," *IEEE Transactions on Information Forensics and Security*, vol. 10, no. 6, pp. 1180–1192, 2015.

34. P. E. Pace, *Detecting and Classifying Low Probability of Intercept Radar*. Artech House Inc., Norwood, MA, 2004.
35. M. A. Richards, J. A. Scheer, and W. A. Holm, *Principles of Modern Radar, Basic Principles*. SciTech Publishing, Raileigh, NC, 2010.
36. C. M. Talbot, M. A. Temple, T. J. Carbino, and J. A. Betances, “Detecting Rogue Attacks on Commercial Wireless Insteon Home Automation Systems,” *Computers and Security*, vol. 74, pp. 296–307, 2018.
37. D. R. Reising, M. A. Temple, and M. J. Mendenhall, “Improving Intra-cellular Security using Air Monitoring with Radio Frequency (RF) Fingerprints,” *IEEE Wireless Communications and Networking Conference*, pp. 1–6, 2015.
38. R. O. Duda, P. E. Hart, and D. G. Stork, *Pattern Classification, Second Edition*. John Wiley & Sons, Inc., New York, NY, 2001.
39. D. C. Montgomery, *Design and Analysis of Experiments, Ninth Edition*. John Wiley & Sons, Inc., Hoboken, NJ, 2017.
40. “Ettus Research USRP B205 mini Software Defined Radio [User Manual],” Ettus Research, National Instruments, Santa Clara, CA, 2010.
41. “Agilent 33250A 80 MHz Function/Arbitrary Waveform Generator [User Guide] Ed. 2.,” Agilent Technologies, Santa Clara, CA, 2003.
42. “About USRP Bandwidths and Sampling Rates [Application Note 177],” Ettus Research, National Instruments, Santa Clara, CA, 2016.

# REPORT DOCUMENTATION PAGE

*Form Approved*  
OMB No. 0704-0188

The public reporting burden for this collection of information is estimated to average 1 hour per response, including the time for reviewing instructions, searching existing data sources, gathering and maintaining the data needed, and completing and reviewing the collection of information. Send comments regarding this burden estimate or any other aspect of this collection of information, including suggestions for reducing this burden to Department of Defense, Washington Headquarters Services, Directorate for Information Operations and Reports (0704-0188), 1215 Jefferson Davis Highway, Suite 1204, Arlington, VA 22202-4302. Respondents should be aware that notwithstanding any other provision of law, no person shall be subject to any penalty for failing to comply with a collection of information if it does not display a currently valid OMB control number. **PLEASE DO NOT RETURN YOUR FORM TO THE ABOVE ADDRESS.**

<b>1. REPORT DATE</b> (DD-MM-YYYY) 19-03-2020		<b>2. REPORT TYPE</b> Master's Thesis		<b>3. DATES COVERED</b> (From — To) Sept 2018 — Mar 2020			
<b>4. TITLE AND SUBTITLE</b>  A Non-Destructive Evaluation application using Software Defined Radios and Bandwidth Expansion				<b>5a. CONTRACT NUMBER</b>			
				<b>5b. GRANT NUMBER</b>			
				<b>5c. PROGRAM ELEMENT NUMBER</b>			
				<b>5d. PROJECT NUMBER</b>			
				<b>5e. TASK NUMBER</b>			
<b>6. AUTHOR(S)</b>  O'Brien, Nicholas J, Flight Lieutenant, RAAF				<b>5f. WORK UNIT NUMBER</b>			
				<b>7. PERFORMING ORGANIZATION NAME(S) AND ADDRESS(ES)</b> Air Force Institute of Technology Graduate School of Engineering and Management (AFIT/EN) 2950 Hobson Way WPAFB OH 45433-7765			
				<b>8. PERFORMING ORGANIZATION REPORT NUMBER</b>  AFIT-ENG-MS-20-M-049			
<b>9. SPONSORING / MONITORING AGENCY NAME(S) AND ADDRESS(ES)</b>  Intentionally Left Blank				<b>10. SPONSOR/MONITOR'S ACRONYM(S)</b>			
				<b>11. SPONSOR/MONITOR'S REPORT NUMBER(S)</b>			
<b>12. DISTRIBUTION / AVAILABILITY STATEMENT</b> DISTRIBUTION STATEMENT A: APPROVED FOR PUBLIC RELEASE; DISTRIBUTION UNLIMITED.							
<b>13. SUPPLEMENTARY NOTES</b>							
<b>14. ABSTRACT</b> The development of low-complexity, lightweight and low-cost Non-Destructive Evaluation (NDE) equipment for microwave device testing is desirable from a maintenance efficiency and operational availability perspective. Current NDE equipment tends to be custom-designed, cumbersome and expensive. Software Defined Radio (SDR) technology, and a bandwidth expansion technique that exploits a priori transmit signal knowledge and auto-correlation to effect received signal reconstruction provides a potential solution. This research investigated the reconstruction of simultaneous SDR receiver instantaneous bandwidth (sub-band) collections. The adjacent sub-bands collectively spanned a transmit signal bandwidth. Research culminated in a 100 MHz bandwidth uniform white noise transmit signal reconstruction. The transmit signal provided near true-noise characteristics ( $2^{36} - 1$ non-repeatable sequences). The reconstructed bandwidth exceeded a single B205 SDR receiver instantaneous bandwidth and provided accurate symbol recovery for the inherent SDR Energy per Symbol to Noise Power Spectral Density.							
<b>15. SUBJECT TERMS</b>  Instantaneous Bandwidth Expansion, Software Dened Radio, Non-Destructive Evaluation							
<b>16. SECURITY CLASSIFICATION OF:</b>			<b>17. LIMITATION OF ABSTRACT</b>	<b>18. NUMBER OF PAGES</b>	<b>19a. NAME OF RESPONSIBLE PERSON</b>		
<b>a. REPORT</b>	<b>b. ABSTRACT</b>	<b>c. THIS PAGE</b>			Dr. Peter J Collins, AFIT/ENG		
U	U	U	UU	147	<b>19b. TELEPHONE NUMBER</b> (include area code) (937) 255-3636, ext 7256; peter.collins@afit.edu		